| | |
|---|---|
| **Submitted to:** | Dr. Seth Lawson<br>National Energy Technology Laboratory<br>U.S. Department of Energy |
| **Project Title:** | "Effects of Hot Streak and Phantom Cooling on Heat Transfer in a Cooled Turbine Stage Including Particulate Deposition" |
| **Type of Report:** | Final |
| **Reporting Period Start Date**: | 1 October 2011 |
| **Reporting Period End Date**: | 30 September 2015 |
| **Principal Authors:** | Dr. Jeffrey Bons, Ohio State University<br>Dr. Ali Ameri, Ohio State University |
| **Date of Report**: | 8 January 2016 |
| **DOE Award Number:** | DE-FE0007156 |
| **Submitting Organization:** | JEFFREY P. BONS, PhD, Professor<br>Department of Aerospace Engineering<br>The Ohio State University<br>DUNS: 83212723<br>2300 West Case Rd.<br>Columbus, OH<br>(614) 247-8414, bons.2@osu.edu |

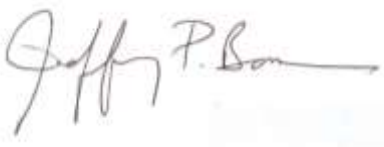

## DISCLAIMER

## ABSTRACT

The objective of this research effort was to develop a validated computational modeling capability for the characterization of the effects of hot streaks and particulate deposition on the heat load of modern gas turbines. This was accomplished with a multi-faceted approach including analytical, experimental, and computational components. A 1-year no cost extension request was approved for this effort, so the total duration was 4 years. The research effort succeeded in its ultimate objective by leveraging extensive experimental deposition studies complemented by computational modeling. Experiments were conducted with hot streaks, vane cooling, and combinations of hot streaks with vane cooling. These studies contributed to a significant body of corporate knowledge of deposition, in combination with particle rebound and deposition studies funded by other agencies, to provide suitable conditions for the development of a new model. The model includes the following physical phenomena: elastic deformation, plastic deformation, adhesion, and shear removal. It also incorporates material property sensitivity to temperature and tangential-normal velocity rebound cross-dependencies observed in experiments. The model is well-suited for incorporation in CFD simulations of complex gas turbine flows due to its algebraic (explicit) formulation. This report contains model predictions compared to coefficient of restitution data available in the open literature as well as deposition results from two different high temperature turbine deposition facilities. While the model comparisons with experiments are in many cases promising, several key aspects of particle deposition remain elusive. The simple phenomenological nature of the model allows for parametric dependencies to be evaluated in a straightforward manner.

This effort also included the first-ever full turbine stage deposition model published in the open literature. The simulations included hot streaks and simulated vane cooling. The new deposition model was implemented into the CFD model as a wall boundary condition, with various particle sizes investigated in the simulation. Simulations utilizing a steady mixing plane formulation and an unsteady sliding mesh were conducted and the flow solution of each was validated against experimental data. Results from each of these simulations, including impact and capture distributions and efficiencies, were compared and potential reasons for differences discussed in detail. The inclusion of a large range of particle sizes allowed investigation of trends with particle size, such as increased radial migration and reduced sticking efficiency at the larger particle sizes. The unsteady simulation predicted lower sticking efficiencies on the rotor blades than the mixing plane simulation for the majority of particle sizes. This is postulated to be due to the preservation of the hot streak and cool vane wake through the vane-rotor interface (which are smeared out circumferentially in the mixing-plane simulation). The results reported here represent the successful implementation of a novel deposition model into validated vane-rotor flow solutions that include a non-uniform inlet temperature profile and simulated vane cooling.

**TABLE OF CONTENTS**


| Page | Section |
|---|---|
| 1 | Executive Summary |
| 3 | Main Report |
| 3 | Background |
| 4 | Objectives |
| 5 | Approach |
| 7 | Results and Discussion |
| 7 | Fundamental Deposition Modeling |
| 24 | Experimental and Computational Vane Deposition |
| 59 | Vane-Rotor Simulations |
| 77 | References |

# EXECUTIVE SUMMARY

Project Title: Effects of Hot Streak and Phantom Cooling on Heat Transfer in a Cooled Turbine Stage Including Particulate Deposition

Research Team: Dr. Jeffrey Bons and Dr Ali Ameri, Ohio State University

Program Duration: 1 October 2011 – 30 September 2015

Total Cost: $497k with $125k OSU Cost Share

The primary objective of this multi-year research effort was to develop a validated computational modeling capability for the characterization of the effects of hot streaks and particulate deposition on the heat load of modern gas turbines. This was accomplished with a multi-faceted approach including analytical, experimental, and computational components. Experimental data from OSU's Turbine Reacting Flow Facility (TuRFR) deposition cascade facility was used to validate a new deposition model. The TuRFR facility was modified to provide for the generation of inlet temperature profile non-uniformities (hot streaks) which were tracked through the turbine nozzle passage using surface temperature infrared imagery and exit plane temperature measurements. Hot streak evolution and the effect of the hot streaks on deposition were evaluated. Film cooling was then added to both the experiments and the computation to evaluate how the hot streak migration and deposition are affected. Finally, the model's ability to track hot streak migration was exercised on a full turbine stage (vane and rotor) using data previously acquired in the OSU Gas Turbine Laboratory transient turbine test rig. The model was also used to predict deposition in the rotating configuration.

The new deposition model includes the following physical phenomena: elastic deformation, plastic deformation, adhesion, and shear removal. It also incorporates material property sensitivity to temperature and tangential-normal velocity rebound cross-dependencies observed in experiments. The model is well-suited for incorporation in CFD simulations of complex gas turbine flows due to its algebraic (explicit) formulation. This report contains model predictions compared to coefficient of restitution data available in the open literature as well as deposition results from two different high temperature turbine deposition facilities.

This effort also included the first-ever full turbine stage deposition model published in the open literature. The simulations included hot streaks and simulated vane cooling. The new deposition model was implemented into the CFD model as a wall boundary condition, with various particle sizes investigated in the simulation. Simulations utilizing a steady mixing plane formulation and an unsteady sliding mesh were conducted and the flow solution of each was validated against experimental data. Results from each of these simulations, including impact and capture distributions and efficiencies, were compared and potential reasons for differences discussed in detail. The inclusion of a large range of particle sizes allowed investigation of trends with particle size, such as increased radial migration and reduced sticking efficiency at the larger particle sizes. The unsteady simulation predicted lower sticking efficiencies on the rotor blades than the mixing plane simulation for the majority of particle sizes. This is postulated to be due to the preservation of the hot streak and cool vane wake through the vane-rotor interface (which are smeared out circumferentially in the mixing-plane simulation). The results reported here represent the successful implementation of a novel deposition model into validated vane-rotor flow solutions that include a non-uniform inlet temperature profile and simulated vane cooling.

## MAIN REPORT

Project Title: Effects of Hot Streak and Phantom Cooling on Heat Transfer in a Cooled Turbine Stage Including Particulate Deposition

Research Team: Dr. Jeffrey Bons and Dr Ali Ameri, Ohio State University

Program Duration: 1 October 2011 – 30 September 2015

## BACKGROUND

As energy demands increase, the U.S. must consider clean high efficiency alternatives to present fuels. The U.S. has an abundance of coal, the proper use of which could reduce our dependency on foreign gas and oil imports. Coal can be utilized in an environmentally responsible manner if it is decarbonized (assuming carbon sequestration) to produce a high hydrogen content fuel through a water-gas shift process. This HHC synthesis (syngas) gas can then be burned in a gas turbine as part of a highly efficient IGCC plant. To harness the full potential of HHC fuels, the gas turbine will be operated at higher firing temperatures than at present with natural gas. However, localized "hot" spots, as well as large temperature gradients adversely affect the longevity of turbines. The rise in the turbine inlet temperature must be accommodated by the development of better-suited materials and the design of more efficient and effective cooling schemes. Designing efficient cooling schemes requires a detailed knowledge of the gas temperature field through the nozzle and blade of the first turbine stage so that coolant can be effectively used where it is most needed. To make matters more challenging, introduction of non-uniformities in the turbine inlet temperature give rise to hot streaks which lead to thermally driven interactions downstream of the vane. Such "pattern factors" create higher heat loads on the vane and may require additional stagnation cooling depending on the "clocking" of the fuel nozzles with the vane passages. Hot streak migration in the turbine blade passage creates hot gas accumulation on the pressure side and accumulation of cooling air (or "phantom cooling") on the suction side.

Another important characteristic of the HHC fuels is the particulate content of the fuel. Although much of the ash content of the fuel is extracted in the process of gasification and clean-up, a trace amount of particulates remain. Over time, such particulates can deposit and accumulate on hot surfaces and contribute to the deterioration in aero and heat transfer performance of the affected gas turbine. The particulates can also clog film cooling holes and lead to reduced longevity of the blades. Since the deposition process is most dependent on gas and surface temperatures, particulate is most likely to deposit in the path of the hot streaks emanating from the combustor. Figure 1, taken from the RB211 that ingested volcanic ash from Mt Gallungung on 24 June 1982, shows large-scale deposits near midspan on the pressure surface of turbine NGV's with the thickest deposits near the leading edge [Dunn et al., 1996]. This pattern mirrors the expected radial temperature gradient from the RB211 combustor. The rotor showed similar preferential deposition. Clearly, the ability to accurately predict the path of the combustor exit temperature non-uniformities is critical to determining the areas of highest concern for deposition with HHC fuels.

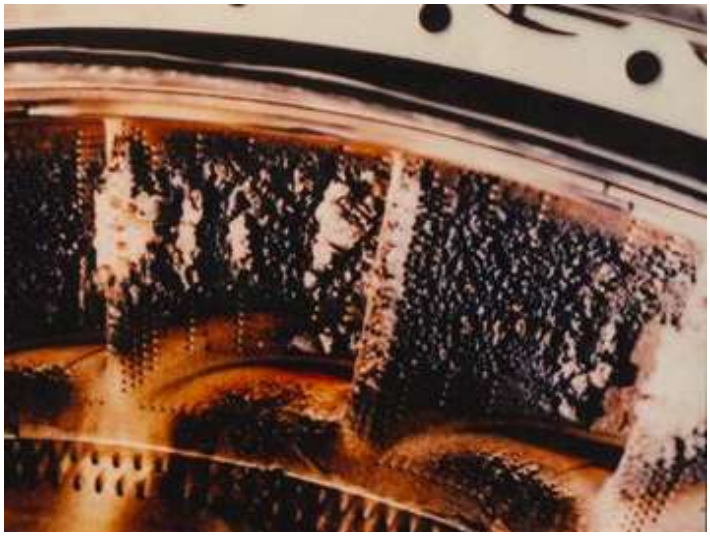

**Figure 1 Volcanic Ash Deposits on pressure surface of NGV's (from Dunn et al., 1996)**

## PROJECT OBJECTIVES

The objective of this project is to develop a validated modeling capability to characterize the effect of hot streaks on the heat load of a modern gas turbine. In its final form, the model will be able to accurately predict the heat load and deposition rates in a cooled turbine stage (vane and rotor), though this ultimate goal will be approached incrementally over the three year research program. Particularly noteworthy is the fact that the research effort will include model validation with data from unique deposition and rotating turbine test facilities at OSU. The work is divided into three specific phases. The specific objectives for each phase are listed below:

**Phase 1. Model validation with experiments for hot streaks in uncooled vane with deposition**

a. Pursue improvements to OSU's existing deposition models, with the goal of more faithfully capturing the fundamental physics of the particle sticking process.
b. Use the TuRFR to measure hot streak migration and surface temperature in NGV without film cooling.
c. Use the TuRFR to measure deposition patterns and rates in uncooled NGV with hot streaks
d. Compare model predictions to TuRFR hot streak and deposition measurements. Adjust model as needed.

**Phase 2. Model validation with experiments for hot streaks in cooled vane with deposition**

a. Use the TuRFR to measure hot streak migration and surface temperature in NGV with film cooling.
b. Use the TuRFR to measure deposition patterns and rates in cooled NGV with hot streaks
c. Compare model predictions to TuRFR hot streak and deposition measurements in cooled NGV. Adjust model as needed.
d. Propose and explore design modifications/guidance that will mitigate HHC particulate deposition on turbine vanes

**Phase 3. Model validation for hot streak migration in rotating turbine stage**

a. Incorporate deposition model into unsteady CFD code capable of making stationary-to-rotating frame flow transition.
b. Extract hot streak migration data from Gas Turbine Laboratory rotating turbine test data from uncooled NASA/DOD URETI turbine.
c. Extract hot streak migration data from Gas Turbine Laboratory rotating turbine test data from cooled NASA/DOD URETI turbine.
d. Geometry Modeling and Gridding.
e. Compare model predictions to URETI hot streak data. Adjust model as needed.
f. Model deposition on the unsteady flow with and without hot streak.
g. Propose and explore design modifications/guidance that will mitigate HHC particulate deposition on turbine rotors.

## APPROACH

**Experimental:** The OSU deposition cascade facility (Turbine Reacting Flow Facility or TuRFR) is designed to replicate the flow through a modern first stage turbine nozzle. The TuRFR consists of a partially premixed natural gas fired combustor capable of operating at an exit Mach number of 0.1 and an exit temperature near 1200°C. This reactor simulates the temperature and velocity conditions at the entrance of a typical first stage nozzle guide vane for an F-class power generation turbine. The system consists of a burner section followed by a cone to accelerate the flow, and an equilibration tube to permit the particles to accelerate to the gas temperature and velocity (Fig. 2). Metered particulate flow is added in the combustor to simulate the desired level of impurities in the gas path. Experiments have been accomplished with several grades of coal fly ash obtained from power plants including bituminous, lignite, and sub-bituminous [Webb et al., (2011)]. The mean particulate size can also be varied from 5-20 microns. The TuRFR's combustor exit flow area accommodates the positioning of multiple passages of actual engine hardware at the combustor exit. The current design accommodates four 6cm span CFM56 nozzle passages, configured as shown in Fig. 3. The facility design is modular so that the vane housing (rectangular to annular transition piece in Fig. 3) can be redesigned to accommodate different sized vanes of an equivalent cross-sectional area. A Rolls-Royce research vane configuration is also available and is being employed for this effort. The Rolls-Royce vane set has a simpler design and lacks film cooling holes that otherwise complicate the CFD modeling. Film holes can be added later in the project at specific locations of interest.

The rectangular transition duct just upstream of the annular cascade is fitted with coolant passages for dilution jets to allow the simulation of combustor exit pattern factors and turbulence levels. Also, coolant can be ducted to the cascade vanes themselves to replicate the internal and film cooling of an actual engine. Coolant temperatures can be adjusted to produce the same absolute gas to coolant temperature difference that would occur in an engine. Optical windows in the sides of the transition duct (Fig. 3) allow for optical access to the vane leading edge and pressure surface. Other laser diagnostics (e.g. PIV for velocity measurement) are also possible.

During Phase 1 of the program, the OSU hot cascade will be used to validate the CFD hot streak migration and deposition models. The hot streaks implemented in the TuRFR will provide the inlet conditions for the computational domain. The TuRFR will also be employed to acquire flat-plate particle deposition data to support fundamental deposition model development and validation. This will be accomplished with an inclined plate test article. Phase 2 will perform the same study with the addition of film cooling through the vane sector.

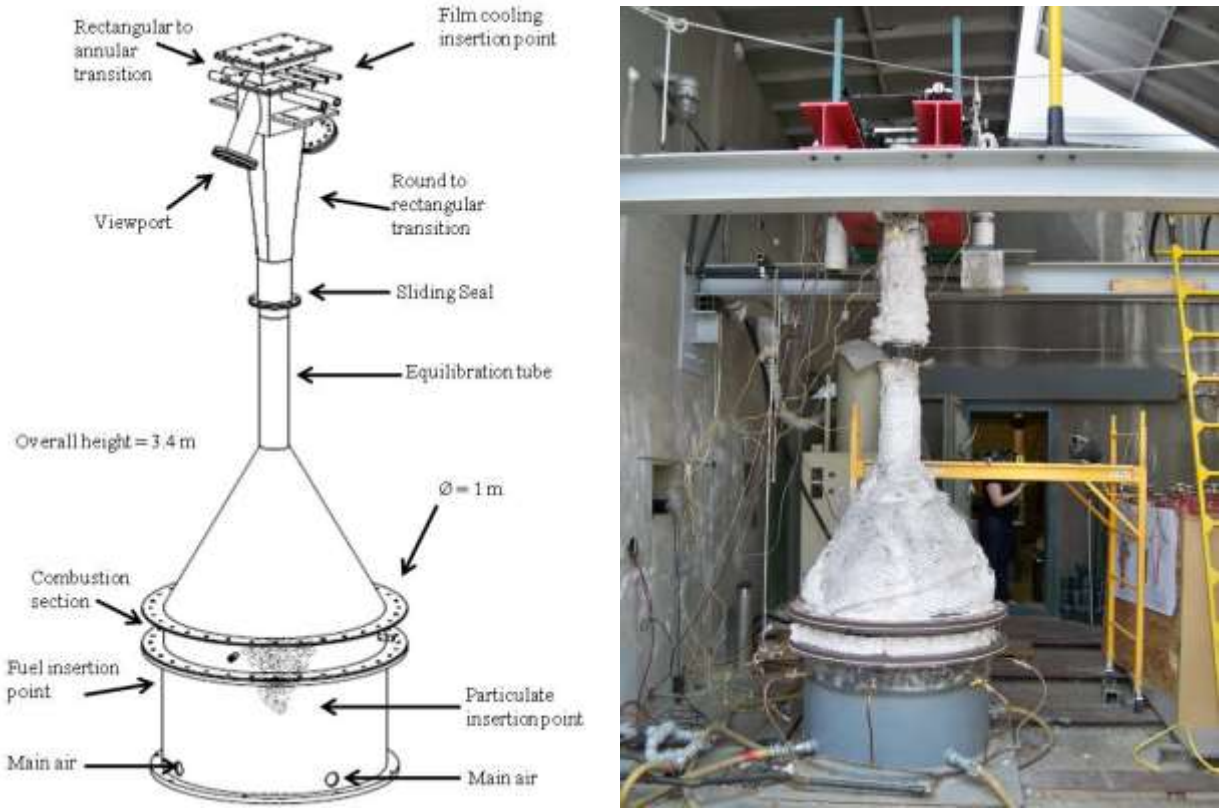


**Figure 2: Turbine Reacting Flow Research facility (TuRFR)**

**Modeling:** In numerical studies, the two steps required for deposition, namely particle tracking and sticking, are performed as a post-processing step once the steady flow analysis is completed. Tracking of particles has been achieved with good success. Particle sticking models, however, lack physical validity in several respects. El-Batsh and Haselbacher (2002) developed a sticking model to quantify the criteria for particle sticking and detachment. Ai (2009) modified the sticking model developed by El-Batsh and Haselbacher and calibrated it to match experimental results. The model from El-Batsh and Haselbacher modified by Ai (the *critical velocity model*) is limited in that does not account for plastic deformation of the particle on impact. Thus, calibration is required for the model to match experimental results. Tafti et. al. (2010) developed a sticking model using the coal ash composition to determine a sticking probability based on the viscosity-temperature relationship. This *critical viscosity* model is limited in that it does not account for elastic deformation and particulate removal or detachment. Perhaps more importantly, neither model accounts for the deposit buildup that occurs on existing deposits. This results in substantial differences between model predictions and experiments [Barker et al., 2011].

This research effort will model these physically relevant phenomena to allow for better simulation of deposition. This will allow more confident predictions and thus better designs through analysis. To improve upon the physical modeling embodied in the deposition models a new sticking model will be developed based on fundamental particle kinematics. From the DPM (Discrete Particle Modeling), the particles have a known kinetic and thermal energy upon impact. Sticking can be determined by a comparison of surface adhesion forces to the rebound

force from impact. The adhesion force is directly related to the surface area of impact. If both the particle and the surface have no deformation upon impact, deposition is unlikely. Whereas, if the kinetic energy is high enough to cause deformation (of the particle or the surface, or both) upon impact, this will increase the surface area and result in a larger force of adhesion. Deformation upon impact is accelerated at high temperatures since the shear modulus and Young's modulus are both inversely related to temperature. At high temperatures, the intermolecular forces maintaining the chemical structure are weakened and the force of impact (which is proportional to the impact velocity, or square root of kinetic energy) may be large enough to cause plastic deformation. Also, if the surface deforms during impact (as it would if the surface is softened ash deposit vs. metal), this will increase the contact area and thus the adhesion force. This is the fundamental approach that will be employed to develop a more accurate sticking model. Specific ash properties will be incorporated into the model through multiple inputs including: the kinetic energy (particle density), thermal energy (specific heat), mechanical properties (shear modulus and/or viscosity), and phase transitions (melting temperature). Two relevant models in the literature that will be used as a springboard include the Integral Elastoviscoplasticity (IEVP) and the Energy Elastoviscoplasticity (EEVP) models.

The Phase 1 modeling effort will culminate with a comparison of deposition predictions with hot streaks on the uncooled vane. Adjustments to the model will be pursued as required. The Phase 2 modeling effort will incorporate vane cooling, and thus include conjugate heat transfer within the blade and cooling passages as well. The final phase will move from the vane into the rotor through a full-stage unsteady calculation of hot streak migration and deposition. The plan is to validate the simulations with hot streak data acquired with a rotating turbine stage in OSU's Gas Turbine Laboratory.

## RESULTS AND DISCUSSION

# Fundamental Deposition Modeling

Soon after the research effort began in 2011 there was a concurrent research effort at Oak Ridge National Lab to acquire mechanical properties of small (10s of micron-sized) ash particles at elevated temperatures to support the current modeling effort. Progress was slow given the complications of pulling on such small specimens, and doing so in an oven was even more challenging. In the final quarters of this effort, since it was not clear when we would receive the Oak Ridge National Lab data for mechanical properties of various ash particle types, we set about developing a new particle impact/deposition model that incorporates as much of the relevant physics as possible. The framework of this physics-based model is such that it can be implemented with "guessed" particle properties as shown below. Should the ORNL data be available at some later date, this will provide validation of the model. The model is outlined below, followed by several validation cases with data from experiments at OSU and elsewhere.

### MODEL BACKGROUND

The present model was born out of the observation that despite the exact constitutive relations employed to derive rebound relations and deposition criteria, most models still rely heavily on empirical correlations to obtain what often amounts to mediocre accuracy when employed for turbine applications. This may in part be due to the fact that particles ingested in gas turbines are not homogenous or spherical. Figure 3 shows SEM images of Arizona Road Dust (ARD) and subbituminous fly ash used in recent deposition studies. Composition measurements using X-Ray Diffraction and Energy Dispersive Spectroscopy show the presence of numerous oxides (though primarily $Al_2O_3$ and $SiO_2$). Given the random shapes typical of ingested particulate, it seems inappropriate and unnecessary to base particle rebound models solely on spherical structural mechanics. In many cases, a simpler phenomenological model of a complex process can provide greater insight into parametric dependencies that are obfuscated by a seemingly more sophisticated (yet equally empirical and approximate) analysis.

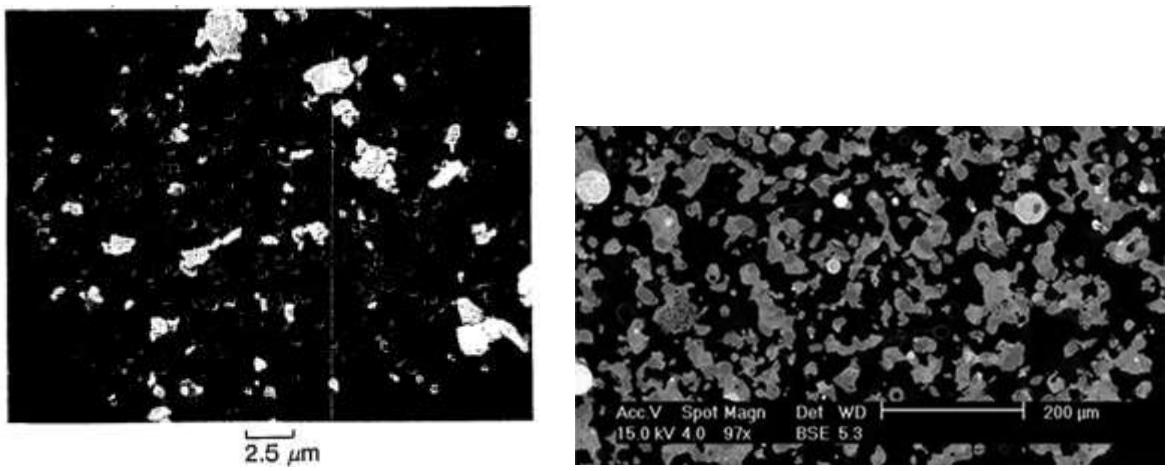


**(a)** **(b)**

**Figure 3: SEM images of (a) ARD particles (from Hindman et al.) and (b) subbituminous ash particles (from Whitaker and Bons)**

The model presented here is intended to capture the observed dependencies of particle rebound and deposition for particles typically ingested in gas turbines. It incorporates the following physical phenomena: elastic deformation, plastic deformation, adhesion, and shear removal. It also incorporates material property sensitivity to temperature and tangential-normal velocity rebound cross-dependencies observed in experiments. The goal is to have the model be as simple as possible so that it can be easily incorporated in a CFD simulation of complex gas turbine flows with an algebraic formulation (without extensive iteration or numerical integration). Hopefully, this "simple" approach will allow users to more readily identify the fundamental physics being modeled so that parametric dependencies are easily evaluated. The balance of this section outlines the model and subsequently demonstrates its accuracy relative to several rebound and deposition data sets available in the open literature.

#### MODEL DEVELOPMENT

Since airborne particles come in all shapes and sizes, the model dispenses with the spherical representation in favor of a circular cylinder that contacts the surface end-on (Fig. 4). This allows the elastic and plastic deformation of impact to be modeled simply as 1-D cylinder compression rather than 3-D combined compression/tension of a sphere. Though it is recognized that the actual contact between a particle and the surface will first occur at protrusions and asperities along the plane of impact, this 1-D model assumes that the bulk of the particle mass responds as a 1-D spring with spring constant $\kappa = AE/\ell$. The effect of surface asperities will be accounted for later in the adhesion model.

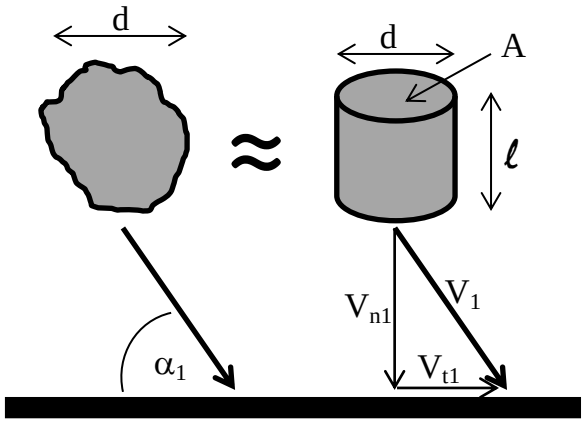


**Figure 4: Particle representation as circular cylinder.**

The elastic energy absorbed in the compression of a cylinder (spring) is related to the applied load (P) and deflection (w) by

$$E_{el} = \int_0^w P dw \qquad [1]$$

For a circular cylinder of cross-section area A, the applied load is simply $P = \sigma A$. The elastic stress-strain relation of $\sigma = E\varepsilon$ can then be employed with $\varepsilon = w/\ell$ to rewrite Eq. 1 as:

$$E_{el} = \int_0^w \frac{EA}{\ell} w dw = \left(\frac{EA}{\ell}\right)\frac{w_{el}^2}{2} \qquad [2]$$

The definite integral can be solved directly if A and $\ell$ are treated as constant during the elastic deformation ($w_{el}$).

The elastic deformation phase of the model converts inbound normal kinetic energy directly to elastic energy, similar to other spherical models. Setting this equality allows the determination of the elastic particle deformation ($w_{el}$) for a given change in normal kinetic energy ($\Delta KE_n$). Assuming a cylinder of diameter, d, and length $\ell$ = 2d/3 (which corresponds to the same volume as a sphere of diameter d) the elastic deformation is

$$w_{el} = \left(\frac{16}{3\pi}\frac{\Delta KE_n}{d\ E}\right)^{0.5} \quad [3]$$

For reference, this can be compared to the expression derived by Singh and Tafti for spherical particles,

$$w_{el} = \left(\frac{15}{4\sqrt{2}}\frac{\Delta KE_n}{d^{0.5}\ E}\right)^{0.4} \quad [4]$$

Following a linear stress-strain relation, elastic compression of the particle will continue until the yield stress ($\sigma_y$) is reached. At this point, the model assumes that elastic energy storage ceases and all remaining normal kinetic energy is expended in plastic deformation. This is depicted in Fig. 4. From the figure, it is clear that the critical deformation, $w_{crit}$, is equal to $\sigma_y\ell$/E and the maximum elastic energy storage is,

$$E_{crit} = \left(\frac{EA}{\ell}\right)\frac{w_{crit}^2}{2} \quad [5]$$

For the particles evaluated in this study, $w_{crit}/\ell$ was always less than 1%, thus validating the use of constant cylinder geometry in the integration of Eq. 2.

Following the stress-strain path depicted in Fig. 5, the load during plastic deformation of the particle is $\sigma_y$A. Thus one can derive an expression for the maximum deformation ($w_{max}$) when all of the normal kinetic energy is expended,

$$KE_{n1} = E_{crit} + \int_{w_{crit}}^{w_{max}} \sigma_y A dw \quad [6]$$

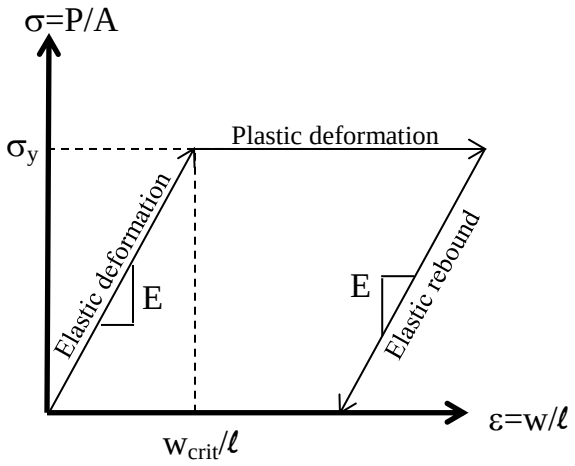


**Figure 5: Stress-strain plot indicating impact phases.**

Since plastic deformation of solids is generally considered to be a constant volume process, one can replace A with Vol/($\ell$-w) and integrate Eq. 6 directly to yield an explicit expression for $w_{max}$.

$$w_{max} = \ell - exp\left[ln(\ell - w_{crit}) - \frac{KE_{n1} - E_{crit}}{\sigma_y Vol}\right] \quad [7]$$

In this case, accounting for the variation of A with w is necessary since $w_{max}/\ell$ values can exceed 10%.

Again referring to the stress-strain diagram in Fig. 5, it is assumed that following the maximum deformation, the elastic energy ($E_{crit}$) is available for rebound. If no other physics are accounted for (e.g. adhesion or fluid shear), the rebound normal velocity and ideal normal coefficient of restitution ($CoR_{ni}$) can be computed directly:

$$\tfrac{1}{2}mV_{n2i}^2 = KE_{n2i} = E_{crit} = \frac{Vol\sigma_y^2}{2E} \quad [8]$$

$$\text{Thus,} \quad CoR_{ni} = \frac{V_{n2i}}{V_{n1}} = \sqrt{\frac{\sigma_y^2}{\rho E}}\frac{1}{V_{n1}} = \frac{C}{V_{n1}} \quad \text{for } w > w_{crit} \quad [9]$$

$$\text{and} \quad CoR_{ni} = 1 \qquad \text{for } w \le w_{crit}$$

From this derivation it is clear that the ideal $CoR_n$ is only a function of material properties ($\sigma_y$, E, and $\rho$) and not particle size (d). This is because both elastic energy storage and kinetic energy are directly related to particle volume; thus it cancels out of the energy exchange. The same is true for the spherical particles in Singh and Tafti's model (except for sub-micron particles where the $CoR_{ni}$ increases slightly with decreasing diameter). Based on Eq. 9, the dependency of $CoR_{ni}$ on $V_{n1}$ is shown in Fig. 6 for material properties representative of ash particulate (E = 136GPa, $\nu$ = 0.2, $\rho$ = 2320 kg/m$^3$, and $\sigma_y$ = 100, 200, and 300MPa) impacting a surface with matched properties (i.e. $E_c$ = 70.8GPa). The critical normal velocity at which plastic deformation begins is $V_{n1crit} = \sigma_y/(\rho E)^{0.5}$ and in the plastic regime $CoR_{ni}$ is inversely proportional to $V_{n1}$. As will be presented shortly, these trends mirror those found in experimental $CoR_n$ data.

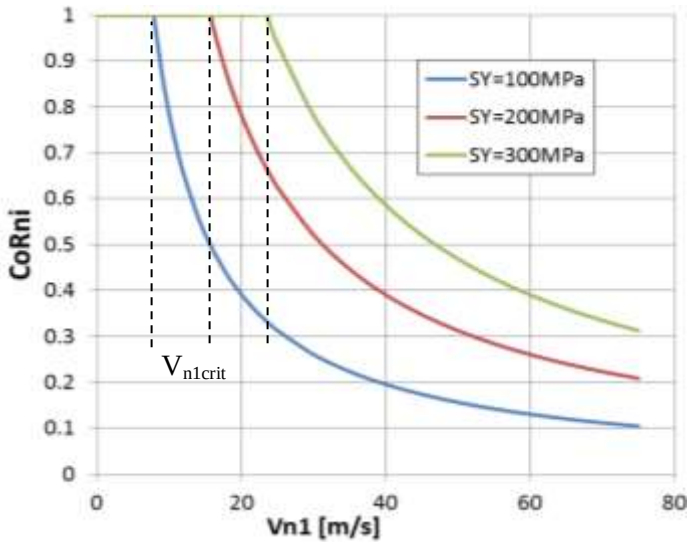


**Figure 6: Ideal normal CoR ($CoR_{ni}$) vs. normal impact velocity ($V_{n1}$) for different $\sigma_y$ (SY) values of ash particulate.**

In keeping with all other particle impact models, the appropriate Young's modulus to use in the above relations is the composite modulus defined as,

$$\frac{1}{E_c} = \frac{1-\nu_1^2}{E_1} + \frac{1-\nu_2^2}{E_2} \qquad [10]$$

where the subscripts 1 and 2 refer to the particle and surface respectively. This accounts for the fact that both the particle and the surface deform under impact, each depending on their relative stiffness. If the particle impacts previous deposits of the same material, then the composite $E_c = E/(2(1-\nu^2))$. The Poisson's ratio ($\nu$) accounts for the transverse strain under axial compression of the particle. Common values for metals are 0.3 and for airborne particles formed from materials found in earth's crust the values are closer to 0.2. The yield stress in Eq. 9 is the lower of either the surface or the particle since the weaker material will plastically deform first.

The ideal rebound normal velocity ($V_{n2i}$) can be reduced by adhesion from van der Waals forces or electrostatics. Johnson et al. proposed a work of adhesion ($W_a$) required to overcome adhesion forces of $W_a = \pi a_{cont}^2 \gamma$ where $A_{cont} = \pi a_{cont}^2$ is the contact surface area and $\gamma$ is the surface free energy. The surface free energy ($\gamma$) depends on properties of the particle and surface materials. Unfortunately, these properties are not generally available for airborne particles that are ingested in gas turbines. Typical values of $\gamma$ in the open literature are of order one and a constant value of $\gamma = 0.8$ is used for the results in this paper. This value may be adjusted to match data from different particle and surface types. Analytical expressions for the contact radius "$a_{cont}$" of a spherical impact have been derived by others. The non-spherical particle representation employed in this model necessitates a semi-empirical derivation for $A_{cont}$ .

$$\frac{A_{cont}}{A_{crit}} = a + b\left(\frac{w_{max}}{w_{crit}}\right)^c \qquad [11]$$

The form of Eq. 11 is such that $A_{cont}$ increases with increased maximum plastic deformation ($w_{max}$). The physical basis for this relationship is that increases in deformation beyond $w_{crit}$ signal greater plastic deformation. The contact surfaces are not smooth to begin with, so plastic deformation will increase the engagement of asperities on the surfaces and thus $A_{cont}$ will rise. The constants a=0.1, b=1/7, and c=0.5 were determined based on empirical fit to rebound and deposition data which will be shown hereafter. There is an apparent contradiction between a model that represents particle impact mechanics with an end-on cylinder impact and yet a contact area for adhesion that is other than the cylinder cross-sectional area. The physical justification for this apparent contradiction is that the impact mechanics are derived from a "macro" view of the 1-D particle response while the adhesion accounts for the "micro" perspective of numerous, small surface asperities engaging during impact.

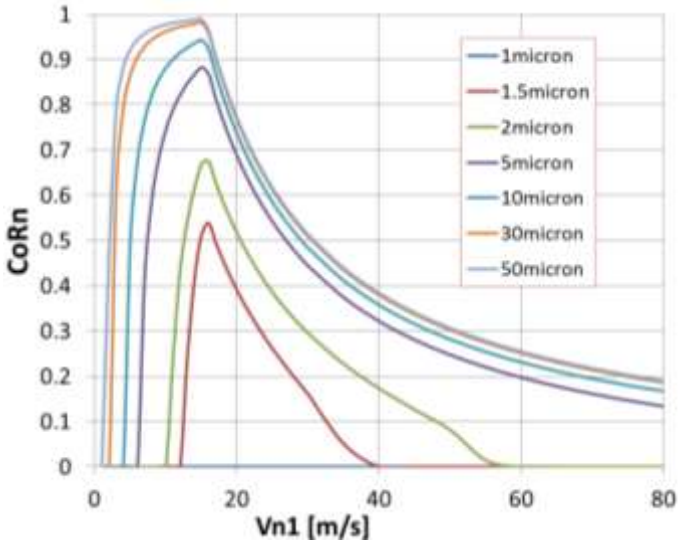


**Figure 7: Normal CoR vs. normal velocity ($V_{n1}$) for 1 < d < 50μm. Ash particles with Fig. 6 properties.**

The rebounding normal kinetic energy ($KE_{n2}$) is derived by subtracting the work of adhesion ($W_a$) from the critical elastic energy ($E_{crit}$). As such, the actual $CoR_n$ will always be smaller than the ideal $CoR_{ni}$. Figure 7 shows $CoR_n$ vs. $V_{n1}$ for particle diameters of 1 to 50micron for the $\sigma_y$=200MPa case of Fig. 5. One of the first things that is evident from Fig. 7 is that unlike the ideal $CoR_n$, the actual CoR (accounting for adhesion) depends on particle diameter. This is because the work of adhesion is proportional to surface area ($d^2$) while elastic energy is proportional to volume ($d^3$). Thus, adhesion has a dominant effect for small diameter particles. Also, for a given diameter, there is a critical diameter below which $CoR_n = 0$. This represents particle deposition. This is the same result predicted by Brach and Dunn's "critical velocity" model. For this parameter set, the 1μm particles deposit at all velocities, whereas the velocity below which particles stick drops non-linearly from 13m/s at 1.5μm to 2m/s at 50μm. The smallest particles can also experience deposition at very high normal velocities, where the plastic deformation is excessive. In Fig. 7, the 1.5micron particle experiences a maximum plastic deformation of $w_{max}/\ell$ = 4% at $V_{n1}$=80m/s.

The result depicted in Fig. 7 is for a normal (90°) particle impact. It was observed by the authors that since the tangential velocity does not figure into the $CoR_n$ calculation, a 1 micron

particle impacting with $V_{n1}$ = 10m/s and zero tangential velocity (a 90° impingement angle) will have the same propensity to deposit as a particle impacting with $V_{n1}$ = 10m/s and $V_{t1}$ = 100m/s (a 6° impingement angle). Since the adhesion force acts on the lower extremity of the particle, a large $V_{t1}$ will produce a significant moment from the particle's center of gravity to the surface ($\ell/2$) that will no-doubt reduce the ability of adhesion to capture the plastically deformed particle, a fact that the model completely ignores. This non-physical result can be corrected by multiplying $W_a$ by $\sin(\alpha_1)$. The use of this cross-dependency between tangential and normal impact velocity greatly improved the agreement with experimental deposition data.

Since deposition in gas turbines often occurs in the presence of significant fluid forces due to high flow velocities, another aspect that is included in the present model is the effect of fluid shear. The critical moment theory was used to account for the tendency of fluid shear to create a rolling moment on the particle and thus overcome the adhesion force. While the same fluid flow could also cause a particle to slide along or lift-off from the surface, Zoeteweij et al. showed that for particles less than 100micron diameter, the rolling mechanism is dominant. The model follows the incorporation of the critical moment theory used previously by others in that the particle is assumed to reside in the linear region of a turbulent boundary layer and the drag force is dependent on the local Reynolds number. Consistent with the present model's cylindrical particle representation, the drag relation employed is for flow around a cylinder at low Re rather than over a sphere. The model uses the cylinder-in-crossflow drag correlation found in White and integrates the drag-moment from the contact surface to the top of the cylinder ($\ell$). The resulting shear drag-moment relation is shown in Eq. 12. Similar to Soltani and Ahmadi, the drag-moment is multiplied by a correction factor of 1.7 to account for wall effects.

$$M_{drag} = \frac{\rho^3 u_\tau^4 d \ell^4}{8\mu^2} + \frac{3\rho^{5/3} d^{1/3} u_\tau^{8/3} \ell^{10/3}}{2\mu^{2/3}} \qquad [12]$$

(obtained using $c_d = 1 + \frac{10}{Re_d^{2/3}}$ from White)

To account for the effect of this shear drag-moment on the deposition process, the counterbalance between shear, adhesion, and elastic rebound is assessed as follows. It is observed that this shear moment will reduce the effectiveness of adhesion forces in overcoming the elastic energy that is attempting to liberate the particle. The adhesion force acts with a moment arm of d/2 about the leeward point of the cylinder as it rests on the surface. Thus $M_{drag}/a_{cont}$ represents the reduction in effectiveness of the adhesion force to restrain the particle. Equivalently, this "liberating" shear force could be added to the elastic force of the compressed cylinder. Since the force exerted by a cylinder in compression is easily related to its deformation (w), and finally to elastic energy ($0.5\kappa w^2$), the shear drag moment has the effect of increasing the value of $E_{crit}$ available for rebound. This is how the shear force is implemented in the present model. It is assessed at the point of maximum plastic deflection and has the effect of increasing the $CoR_n$ in high velocity flows. As a practical matter, the $CoR_n$ is capped at the ideal value. This implementation is different from previous attempts to incorporate the effects of fluid shear in that the shear removal is evaluated concurrent with the rebound determination between elastic energy and adhesion. All previous implementations perform the shear removal calculation after the particle is deposited, when shear competes with adhesion only. This simultaneous treatment

in the present model was considered to be more representative of the physics that are in play at the time of particle impact.

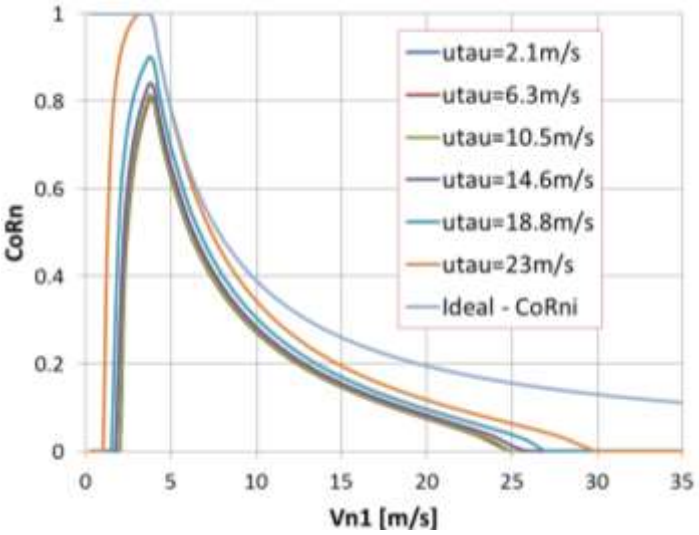


**Figure 8: $CoR_n$ vs. $V_{n1}$ for a range of shear velocities from 2-23m/s and $CoR_{ni}$. Data for 50μm ash particle with low strength ($\sigma_y$=50MPa).**

Figure 8 shows the effect of accounting for shear in the rebound/deposition calculation. Results are shown for a range of $u_\tau$ (the turbulent shear velocity) from 2-23m/s as well as the ideal (no adhesion) $CoR_{ni}$. The plot was generated for a large (50μm) ash particle with low strength ($\sigma_y$=50MPa) to exaggerate the effect. The composite modulus is the same as Fig. 6 ($E_c$ = 70.8GPa) and the fluid properties were set to match those found in the first stage of a modern high pressure turbine (OPR = 33, $T_{t4}$ = 1600K) operating at 3km altitude. These operating conditions and $u_\tau$ levels correspond to a local fluid velocity from 50-550m/s at a flow Reynolds number of $Re_x \cong$ 1e6 ($c_f$ = 0.0035). High shear reduces the deposition at low (<2m/s) and high (>25m/s) normal impact velocities in Fig. 8. As is evident in Eq. 12, the effect of shear scales with particle size to the 4th and 3rd power (for the 2 terms in Eq. 12 respectively). It also scales with velocity to approximately the same powers. Thus, shear has its greatest influence at high flow velocity and large particle diameter. Since the majority of particle deposits predicted by the model are for small particles at low velocities (Fig. 7), the influence of shear has a negligible effect on the predictions included in this study. Its effect has been included nonetheless. As deposits accumulate on a surface and increase the "effective" diameter of the obstruction to the flow, shear will certainly play a more dominant role. At some point, deposit buildup will begin to have a first order effect on the flow over the surface which would necessitate a new flow calculation.

Since the objective of the present model is to provide predictions of both particle deposition and rebound, one final relation is needed – the tangential rebound velocity ($V_{t2}$). Brach and Dunn provide a kinematic relation for $V_{t2}$ that was modified slightly to improve agreement with rebound data as follows. The original Brach and Dunn relation is shown in Eq. 13 below. The expression is also presented in terms of the quantities that are available from the present model.

$$V_{t2} = V_{t1} - \mu V_{n1}(1 + CoR_{n1i})\sqrt{1 - \frac{2W_a}{mV_{n1}^2 CoR_{ni}^2}}$$

$$V_{t2} = V_{t1} - \mu(V_{n1} + V_{n2i})\left(\frac{V_{n2}}{V_{n2i}}\right) \quad [13]$$

This expression was modified for the present model by multiplying the second term in Eq. 13 by $\cos^2(\alpha_1)$. This was done to account for the experimental observation that the normal velocity has a rapidly decreasing influence on the tangential rebound velocity as the impingement angle is increased. This will be made evident in the results that follow. In this expression, μ is the impulse ratio. To quote Brach and Dunn, "μ generally is not a coefficient of friction; it is a ratio of impulses, not a ratio of forces. In some special cases (such as for sliding throughout the entire contact duration), μ can be equal to the coefficient of friction." A value of μ =0.3 was generally employed, though this was adjusted to match experimental data where needed.

## RESULTS

### Case 1: Quartz on aluminum

The first model validation was performed using quartz particle impact data from Bons et al. The experimental data were acquired for 100-400μm quartz particles impacting a 2024 aluminum plate at 30-80m/s. The properties used in the model are for quartz (E=72GPa, ν=0.17, ρ=2200kg/m$^3$) and aluminum (E=69GPa, ν=0.32) yielding an $E_c$=38GPa. The model results are for a particle size (150μm) and velocity (50m/s) centered on the experimental distribution. The yield stress was adjusted to a value of $\sigma_y$=120MPa to match the trend in the CoRn data and the impulse ratio was set to μ=0.55 to match the CoRt data. Figures 9a & b also include legacy data from Grant and Tabakoff for comparison. Grant and Tabakoff studied 200μm quartz particle impacts on a AL2024 plate at 75m/s.

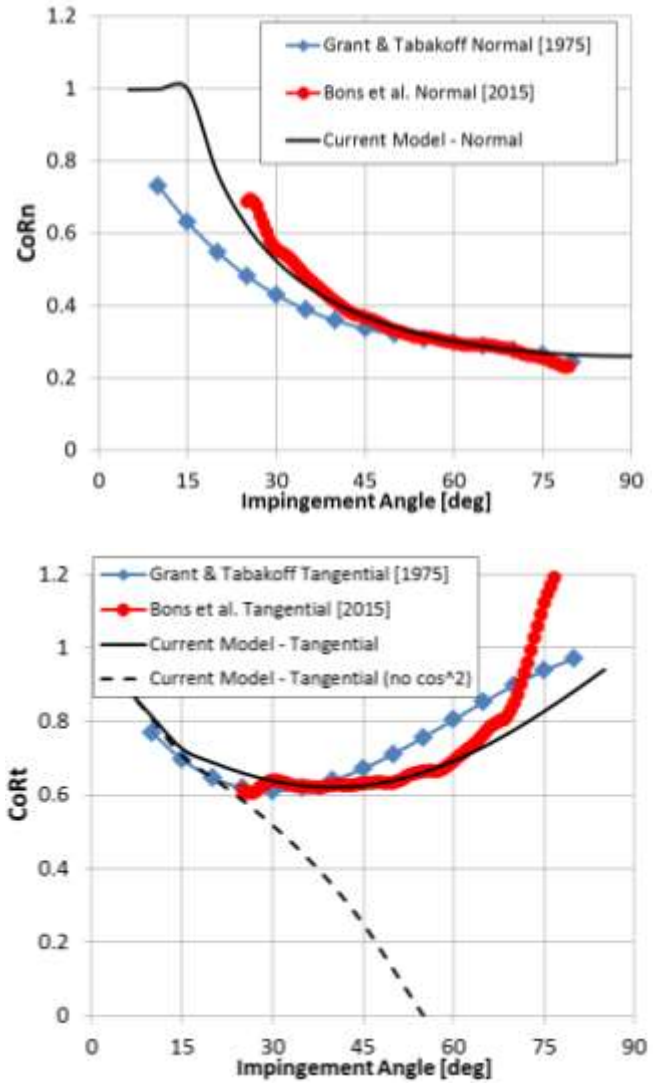


**Figure 9: $CoR_n$ and $CoR_t$ vs. $\alpha_1$ for quartz particle impact on aluminum. Model for 150μm particles compared to data from Bons et al. and Grant and Tabakoff.**

The agreement in both Figs. 9a and 9b is truly remarkable, granted it was only achieved by "tuning" the yield stress and impulse ratio. That said, in the region where CoR data are reliable ($CoR_n$ data are highly erratic at low $\alpha_1$ and likewise $CoR_t$ data are less meaningful for high $\alpha_1$), the match is compelling. Admittedly, the value of $\sigma_y$=120MPa is about half the published value for AL2024. Physically, this lower yield strength could be a result of the sharp quartz protrusions that dig readily into the soft aluminum upon impact, reducing the effective yield strength of the interaction. The match with Grant and Tabakoff's data for the same materials provides additional validation. The $CoR_t$ plot also includes the model prediction without the $\cos(\alpha_1)^2$ factor to the impulse ratio (see discussion of Eq. 13). The data certainly suggest that the intuition for reducing the effect of friction on the tangential velocity as impingement angles become more normal is sound. The experimental data of Delimont et al. for 30μm ARD particles impacting steel plates likewise exhibit a relative insensitivity of $CoR_t$ to $\alpha_1$ that can only be matched with any accuracy using the $\cos(\alpha_1)^2$ factor.

**Case 2: Ash on 410 Stainless Steel**

The second case study was performed using ash particle impact data from Whitaker and Bons. The experimental data were acquired for 3 different types of coal ash (subbituminous, bituminous, and lignite). The size range was 30-130μm and the particles impacted normally ($\alpha_1$=90°) on 410 stainless steel plate. The properties for the 3 ashes and 410SS are shown in Table 1. The values for E and ρ were obtained using the known chemical constituents of each ash and employing the law of mixtures, as outlined in Whitaker and Bons. The yield stress is an estimate derived by comparing CoR data to various impact models as outlined in Whitaker and Bons.

**Table 1: Material Data for Ash and 410SS for Case 2.**

| | Subbituminous | Bituminous | Lignite | 410SS |
|---|---|---|---|---|
| E [GPa] | 136 | 228 | 161.5 | 200 |
| ν | 0.174 | 0.157 | 0.188 | 0.27 |
| ρ | 2320 | 2892 | 1114 | |
| $\sigma_y$ | 360 | 500 | 160 | 290 |
| $E_c$ [GPa] | 85 | 112 | 94 | |

Figure 10 includes a comparison of the model predictions for all 3 ash types alongside the experimental data. The model was exercised using 60μm as the particle diameter since this was the median of the experimental size distribution (the result is not very sensitive to diameter over the range indicated). The subbituminous and bituminous cases used the yield stress of 410SS (290MPa) since it was lower than the values derived by Whitaker and Bons, while the lignite case was conducted using 160MPa. In general, the model predictions using the yield stress values indicated produce a higher $CoR_n$ prediction compared to the experimental data. The plots also include a model case that was run with lower values of $\sigma_y$ to demonstrate the ability to "tune" the model based on this derived quantity.

Figure 10 also includes predictions using the Singh and Tafti model for comparison. The model was exercised using the values shown in Table 1 and the same surface free energy (γ=0.8) as the current model. Over much of the velocity range, the Singh and Tafti result more closely matches the experimental data, though at low velocities it does not follow the rise in $CoR_n$ shown in the data and the current model.

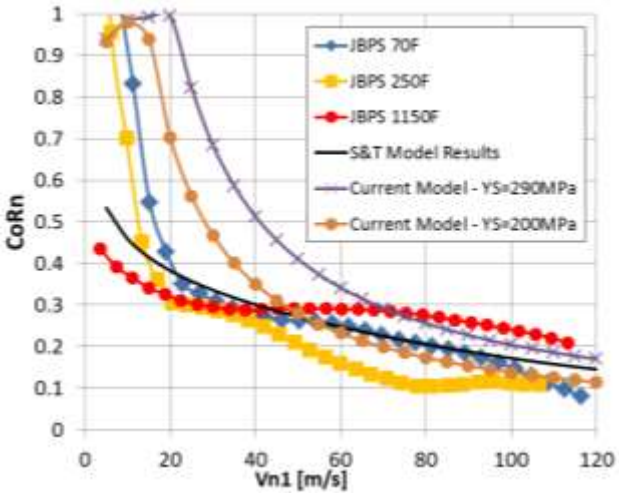


**(a) JBPS Subbituminous**

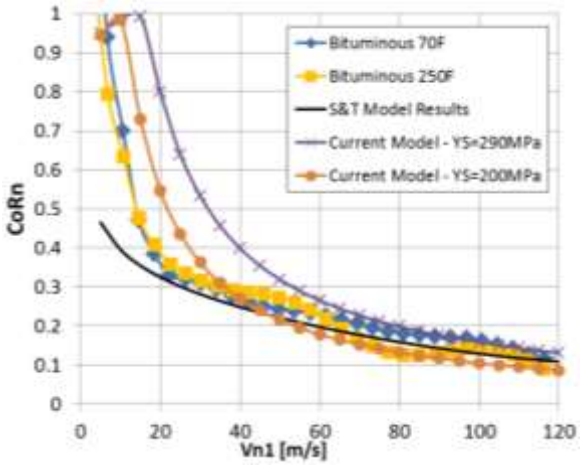


**(b) Bituminous**

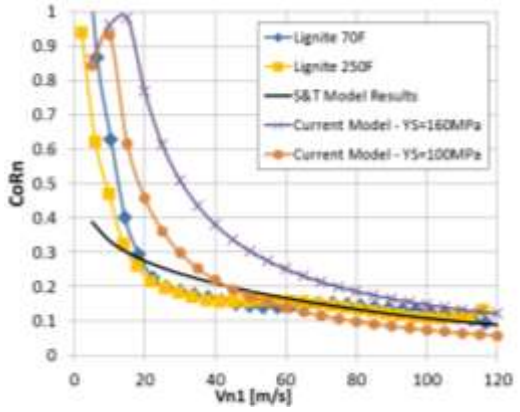


**(c) Lignite**

**Figure 10: $CoR_n$ vs. $V_{n1}$ for 3 ash particle types impacting on 410SS. Model for 60μm particles compared to data from Whitaker and Bons. Model predictions using Singh and Tafti included.**

**Case 3: ARD on 304 Stainless Steel**

The third case study was performed using ARD particle impact data from Reagle et al. The experimental data were acquired for 20-40μm Arizona Road Dust impacting a 304 stainless steel plate at a constant velocity of 27m/s over a range of $\alpha_1$ from 20-80°. The properties for ARD were estimated using the law of mixtures ($\sigma_y$ = 130MPa, E=104GPa, $\nu$=0.18, $\rho$=2650kg/m$^3$). The yield stress was varied from 110-130MPa to obtain the most favorable match with the experimental data. The material properties (E=196.5GPa, $\nu$=0.29) for 304SS are very similar to 410SS.

Figure 11 shows the model predictions compared to the experimental data from Reagle et al. The range of yield stress bounds the experimental results quite well for both $CoR_n$ and $CoR_t$. The $CoR_n$ plot also includes predictions using the Singh & Tafti model with both the authors' original elastic formulation for adhesion and an elastic-plastic variation as developed by Whitaker et al. The comparison is not as satisfactory in this case as it was in Fig. 10. The $CoR_t$ comparison again underscores the importance of modifying the impulse ratio with the $\cos(\alpha_1)^2$ factor to capture the trend in the experimental data.

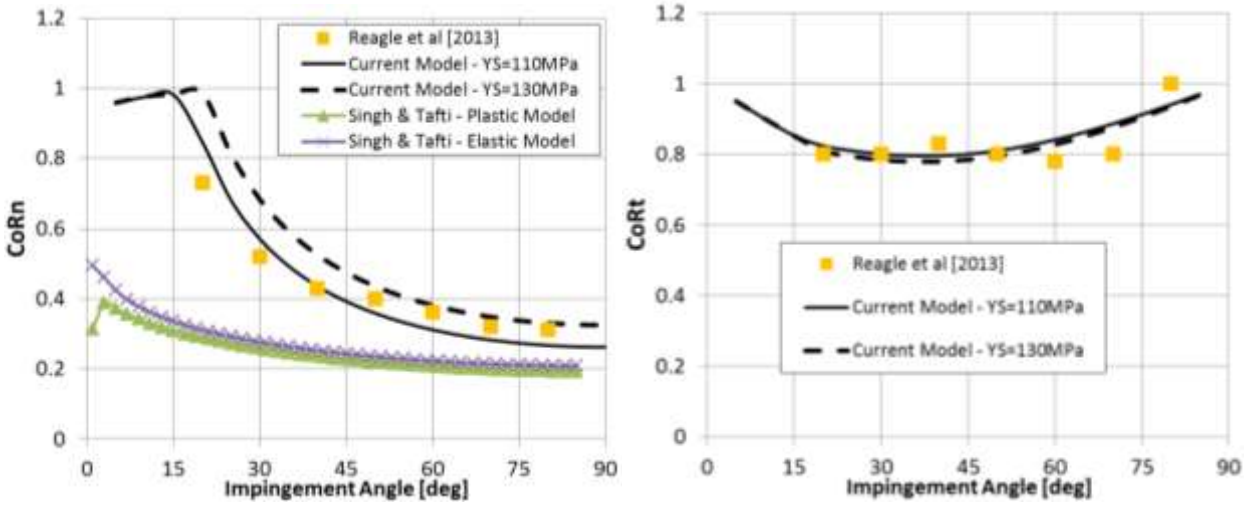


**Figure 11: $CoR_n$ and $CoR_t$ vs. $\alpha_1$ for ARD particle impact on 304SS. Model for 30μm particles compared to data from Reagle et al. Model predictions using Singh and Tafti for $CoR_n$ included.**

The first 3 cases focused exclusively on the rebound prediction capabilities of the model (both normal and tangential). Attention is now turned to the deposition prediction capability and specifically the ability of the model to capture deposition trends with temperature.

**Case 4: Ash Deposition on Inconel at High Temperature**

The fourth case study was performed using ash particle deposition data from Ai and Fletcher. The experiments were conducted with JBPS subbituminous ash particles delivered via a heated jet to a 2.5cm diameter Inconel coupon. The jet impingement angle was 45° and the velocity was maintained constant at roughly 173m/s. The experiments were conducted over a gas temperature range from 1290K to 1450K.

The size distribution for the ash particulate used in the experiment was converted to a piecewise linear distribution for purposes of the model (Fig. 12). Using this size distribution, a

2D Fluent model was created for the jet and target coupon similar to that described in Ai and Fletcher. A schematic of the flow grid is shown in Fig. 13. The mesh consisted solely of unstructured cells, and was heavily refined in the region between the pipe exit and the coupon, as well as around the coupon walls. The model is a RANS formulation with k-w SST turbulence model. Velocity was set to the value prescribed in, with turbulence intensity estimated as 8% and turbulence length scale was set by the hydraulic diameter and correlation in FLUENT. Total temperature at the inlet was set to the measured temperature in each case. The entire domain is enclosed by a pressure outlet boundary, with static pressure set to atmospheric conditions to replicate the experiment.

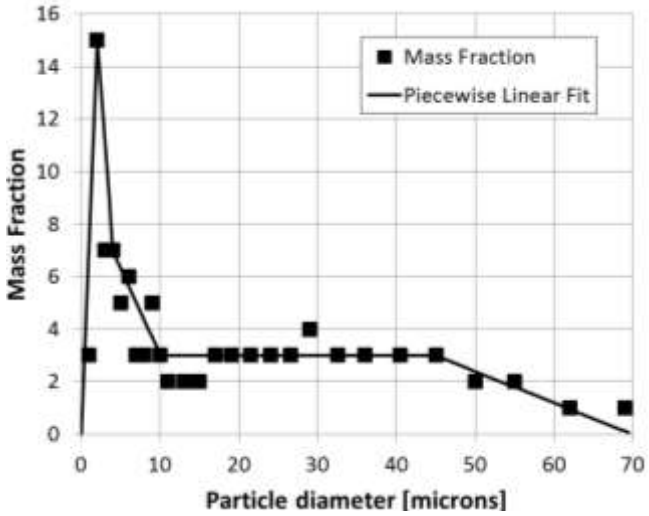


**Figure 12: Size distribution for JPBS subbituminous ash used by Ai and Fletcher with piecewise linear distribution used in model.**

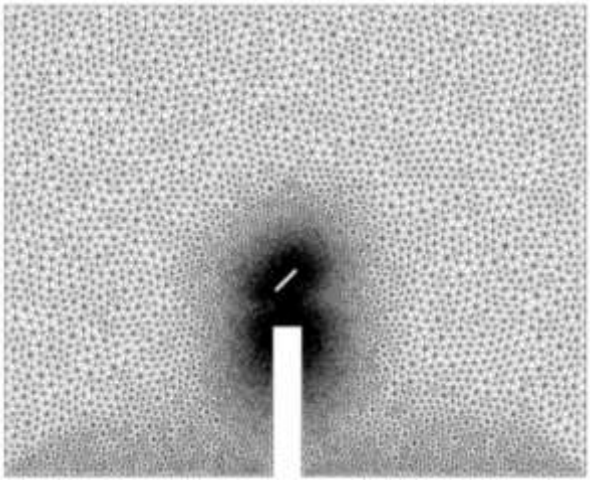

**Figure 13: 2D Fluent model of Ai and Fletcher experimental apparatus used in Case 4 comparison.**

The Discrete Phase Model (DPM) included in FLUENT was used to track particles. This model computes the trajectory of particles by balancing the flow induced forces on the particle with the particle's inertia. The Eulerian-Lagrangian model separates the particulate modeling into two phases. The flow solution is computed in the first phase, absent of particulate. A large amount of dispersed particles are then tracked in the second phase, each trajectory predicted by computing the local forces at each step along the particle's path. This trajectory is stored for each particle. The turbulent dispersion of particles was also modeled using the stochastic tracking random walk feature in FLUENT. In these simulations the volume fraction of particles is sufficiently small that inter-particle collisions as well as the effect of particles on the flow can be neglected.

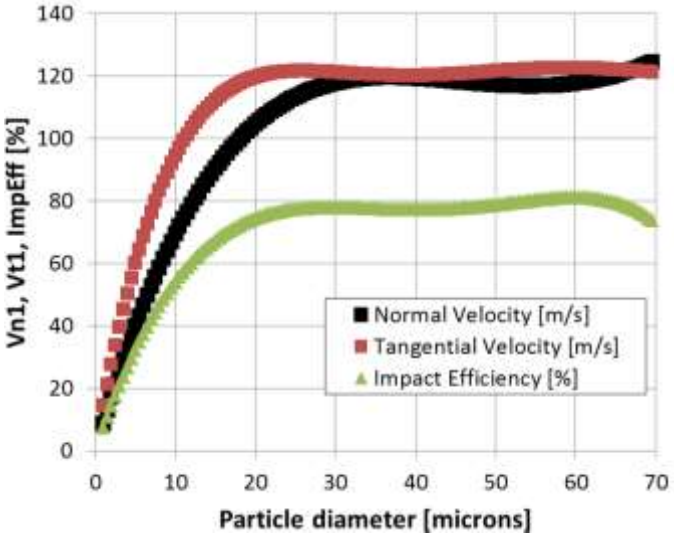


**Figure 14: Variation of particle normal and tangential impact velocity as well as impact efficiency vs. diameter.**

The coupon is modeled as adiabatic such that the particle temperatures are very near the jet exit temperature at all times. Due to the particle model's strong sensitivity to diameter (Fig. 7), it was desirable to inject particles in very fine diameter increments to obtain the most accurate representation of the actual flow. To avoid repetitively exercising the Fluent model for such a fine range of diameters, simulations were conducted for 1, 5, 15, 35, 45, 55, and 65micron diameter particles and the velocity and impact efficiency data were curve fit with polynomials based on diameter. These curve fits were then used to interrogate the model at a much finer ($\Delta d$=0.5micron) resolution for the case study. These curve fits are shown in Fig. 14. The particle impact velocities predicted by the Fluent model vary considerably for particle diameters less than 20micron as shown in Fig. 14. Small particles (with a very small Stokes number) follow the flow and impact the coupon at a very low percentage, while particles >30micron impact the coupon ballistically at approximately the jet exit velocity. The impact efficiency indicates that even at the largest diameter only 80% of the particles strike the surface. This is because the projected diameter of the 45° angled coupon is approximately 20% smaller than the jet exit diameter.

With these particle data, the particle impact model can now be exercised and capture efficiency determined to compare to the experimental data from Ai and Fletcher. In doing so, it

was immediately obvious that the material properties of the ash would need to be functions of temperature to produce the observed increase in particle deposition with temperature. Most engineering materials experience a drop off in yield stress and Young's modulus with temperature. The two most prevalent oxides in the JBPS subbituminous ash are $SiO_2$ and $Al_2O_3$ (50% and 12% by mass, respectively). Property data obtained for $SiO_2$ suggest that E actually increases linearly by 10% from 400K to 1400K while $Al_2O_3$ experiences a 20% drop in E over the same range. Since no data are available for the case where these oxides are combined into JPBS ash, the Young's modulus was held constant with temperature. The yield stress however was adjusted in the particle impact model to yield the most favorable comparison with the experimental data. Since the experimental data indicated no visible deposition for T<1300K, the following linear dependency was used (T is in °K):

$$\sigma_y(T) = 200 - 0.225\,(T - 1000)\ \text{MPa} \qquad [14]$$

For particle temperatures below 1000K, the yield stress value of 200MPa that produced the best fit to rebound data in Fig. 10(a) for subbituminous ash was used. The Young's modulus and density are taken from Table 1 (136GPa and 2320kg/m$^3$ respectively). Since the particles are expected to be depositing on an Inconel surface gradually covered with ash deposits, the material properties for the surface are assumed to match the particulate (similar to Ai and Fletcher).

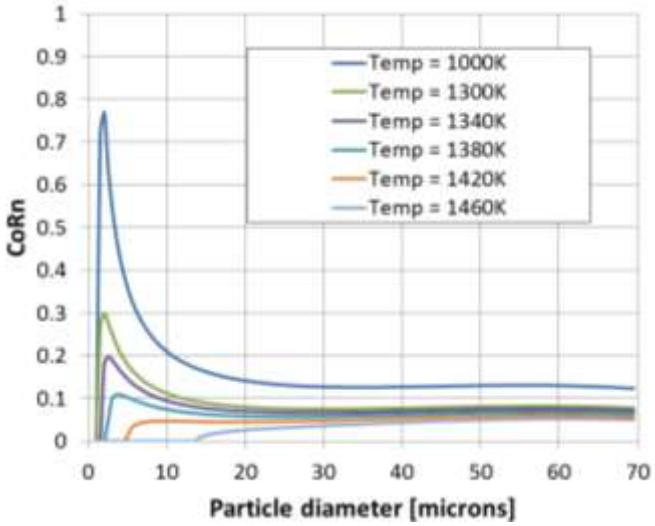


**Figure 15: Variation of $CoR_n$ vs. diameter as a function of temperature for JBPS subbituminous ash.**

Figure 15 shows the model prediction of $CoR_n$ vs. particle diameter for the temperature range of the experimental study. Clearly, the softening of the particle with temperature (modeled as a 50% reduction in yield stress over the range indicated) has the effect of substantially increasing the plastic deformation and thus the contact surface area for adhesion. The diameter below which all particles deposit ($V_{n1crit}$) increases from 2 micron at 1340K to 14micron at 1460K.

The impact efficiency (plotted in Fig. 14) is defined as the % of particles that impact the surface relative to the number injected into the Fluent model. For a given diameter and temperature, Fig. 15 allows an estimate of capture efficiency to be obtained (for all diameters with $CoR_n = 0$). Then, using the mass fractions from Fig. 12 an aggregate deposit mass

(integrating over all diameters) can be calculated and compared directly to the experimental result reported by Ai and Fletcher. This result is plotted vs. temperature in Fig. 16.

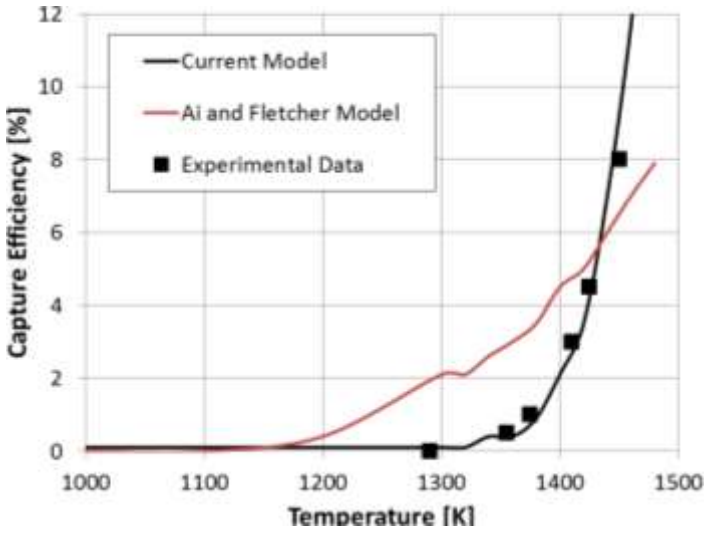


**Figure 16: Predicted capture efficiency vs. temperature including comparison to experimental data from. Prediction from Ai and Fletcher also included.**

Since the $\sigma_y(T)$ variation (Eq. 14) was tuned to match the data, excellent agreement is assured. The significant conclusion therefore is not the agreement, but rather that the simple impact model is versatile enough to capture the experimental deposition trend with temperature. Also, because the model is physics-based, the specific material properties that are needed to predict the deposition behavior (without curve-fitting) are clearly identified. This is in contrast to the deposition model used by Ai and Fletcher to match their experimental data. They used Brach and Dunn's critical velocity model which only accounts for elastic deformation. They tuned the E(T) dependency as shown in Eq. 15 to obtain a capture efficiency prediction that matched the experimental trend:

$$E(T) = 3x10^{20} \exp(-0.02365T) \text{ Pa} \qquad [15]$$

Over the temperature range of 1290-1450K this yields a Young's modulus that varies by a factor of 42 from 17 to 0.4GPa. The dramatic decrease in E is required because the model is based on incomplete physics – it only includes elastic deformation and adhesion, not plastic deformation. Clearly, at temperatures above 1300K, plastic deformation is a significant factor, which is reflected in the current model. Incidentally, the reason that the Ai and Fletcher model results shown in Fig. 16 do not appear to match the experimental data as well as they did in the original paper by the authors is because this model result was generated with the refined diameter distribution of $\Delta d$ = 0.5micron noted in Fig. 12. Ai and Fletcher used a coarse diameter distribution of 2,4,6,8, & 10microns, noting that the predicted capture for particles above 10 microns was zero.

We are currently in the process of implementing the model in more sophisticated particle deposition studies to determine its robustness and universality. Results will be forthcoming in the open literature.

## Experimental and Computational Deposition Studies

Since the new model presented above was not available during the course of this research effort, all 3 phases of the effort were conducted using the critical viscosity model developed by Tafti and Sreedharan. Deposition experiments were conducted for the uncooled and cooled vane, with and without hotstreaks, to provide validation data for companion CFD simulations using Fluent. Since the experimental and computational efforts were always accomplished simultaneously, the results will be presented together as well. This section will document in order: deposition with hot streaks, deposition with a cooled vane, and deposition with hot streaks on a cooled vane. Equation numbers are unique for each of these sections. Following this, the computational efforts with modeling deposition in a full turbine stage will be addressed. Since the TuRFR facility does not have the capability of simulating rotation, there are no experimental results for this section.

### I: Deposition with Hot Streaks:

During the first phase of this effort, several experimental and computational tests were run with simulated hot streaks and deposition. A two-dimensional, high pressure turbine vane geometry was used to fabricate the four-vane annular section used in this study. The two-dimensional geometry was extruded without any span-wise variation, and the vanes were uncooled and had no film cooling holes (Fig. 17). This was chosen to allow for easier comparison to computational results. The annular test section comprises three full vane passages and two half passages.

Hot streaks were simulated in the TuRFR facility by introducing cold gas jets upstream of the vane cascade. Hole size and mass flow were designed to allow penetration at least half way into the core flow. For each experimental test, pressure, temperature, and mass flow were continuously measured in the core flow below the dilution jets, and in the dilution jet supply lines.

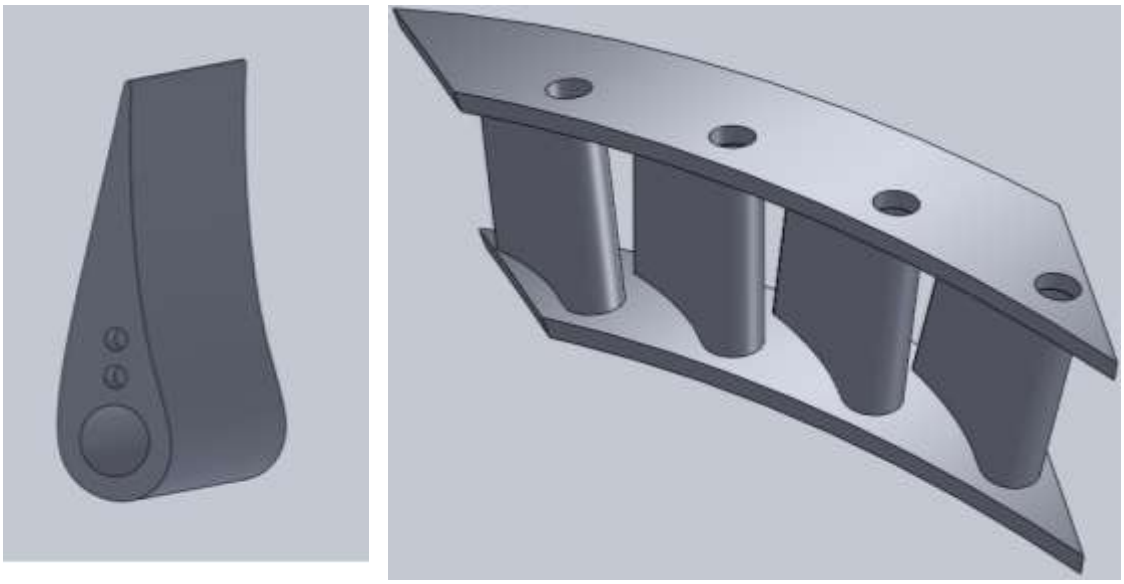

**Figure 17: Vane model used for hot streak studies**

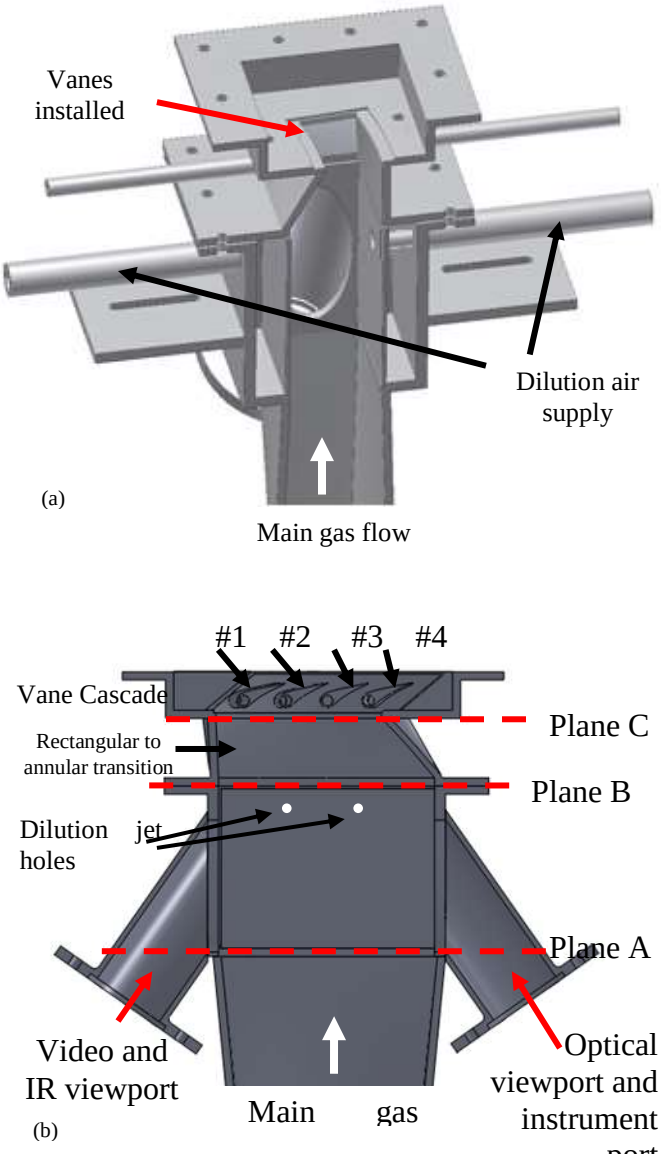


**Figure 18 - Top portion of TuRFR facility, showing cold dilution jet hole locations.**

**FLOW SOLVER**

The flow solution was calculated using Fluent™ software. Unstructured grids were created using Gridgen™ and the geometries of the test regions of the TuRFR facility. The grids included the rectangular to annular transition piece (beginning at Plane B in Fig. 18) and the four-vane cascade test section. The grid was refined in the regions of interest, near the vane walls and at the vane inlet at Plane C. Two grid geometries were created, one without the vanes installed and one with the vanes installed. Illustrations of the two grids are shown in Fig 19.

The governing equations that define the flow solution are the conservation of mass, momentum, and energy for compressible, turbulent flow. The k-ω model was used to model turbulence. The boundary conditions required for the solution are total pressure and temperature at the inlet, static pressure at the outlet, and adiabatic walls with no slip. The flow solution was considered converged when residuals decreased more than four orders of magnitude. The

Reynolds Averaged Navier Stokes and k-ω model contain 7 equations and all converged for the simulations reported in these studies.

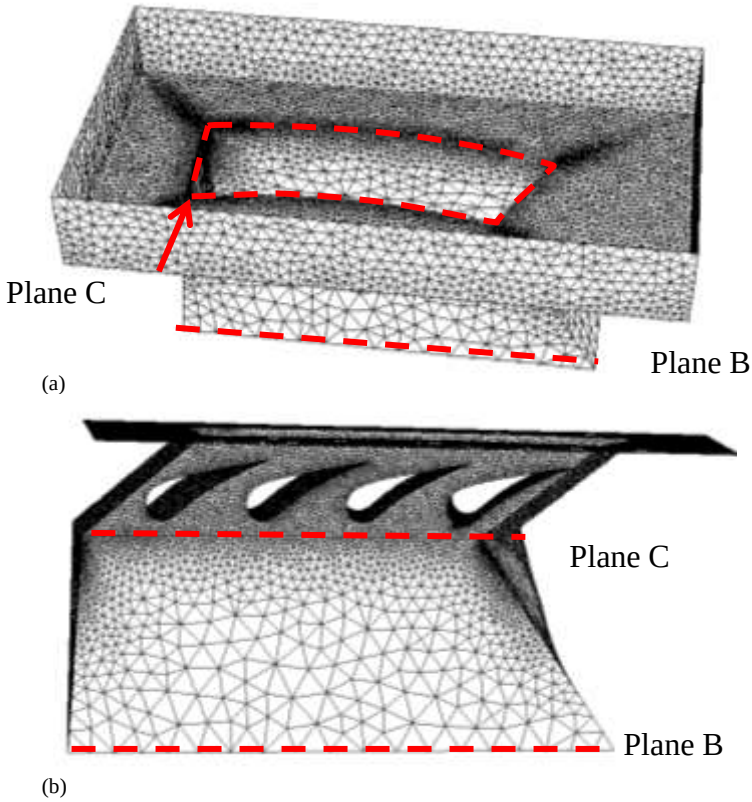


**Figure 19 - Computational grids used in this study. Top section of TuRFR (a) without and (b) with vane cascade installed.**

**Hot Streak Definition**

At this point in the research program it was not possible to experimentally measure the temperature of the gas at the inlet plane of the vanes while the vanes are installed. For this reason, temperature maps were acquired experimentally without the vanes installed at the plane representing the leading edge of the vanes (Plane C). Only the geometry from Plane B to the outlet was modeled [Fig 19(a)]. This provides a solution methodology that is efficient for interrogating different hot streak operating conditions readily. The process to obtain a suitable inlet boundary condition to match the experimental condition is described below.

Hot streak temperature maps at Plane C were acquired experimentally without the vanes installed. A CFD solution using a uniform total pressure and temperature inlet (Plane B) was also generated on the geometry without the vanes installed [Fig. 19(a)].

With the uniform pressure inlet condition, path lines were tracked to determine inlet locations at Plane B that correspond to locations in the vane inlet plane (Plane C). The experimentally acquired temperatures at Plane C were then mapped upstream (without modification to temperature values) to Plane B as a new temperature inlet condition. This second iteration of the CFD solution was then converged to determine the resulting temperature distribution at the vane inlet plane (Plane C), which resembled the hot streak temperature map acquired experimentally.

The second iteration showed that the hot streak had slightly dissipated from Plane B to Plane C, and as such the temperature maps deviated from experimental data. This was corrected by approximating the amount of dissipation, and adjusting the inlet (Plane B) temperature distribution accordingly. This was done by assuming that energy is conserved and dissipation in the streamwise direction is negligible. With these assumptions, an approximate form of the unsteady energy equation is

$$\rho c_p \frac{dT}{dt} = k\left(\frac{d^2T}{dx^2} + \frac{d^2T}{dy^2}\right) \quad [1]$$

Approximating the temporal derivative using a backward difference, and assigning the temperature at Plane B to the temperature at time $t$, and the temperature at Plane C to $t + \Delta t$, the projected temperature is determined by

$$T_B = T_C - \alpha \Delta t\left(\frac{d^2T_C}{dx^2} + \frac{d^2T_C}{dy^2}\right) \quad [2]$$

where $\Delta t$ is the convective time between the two planes. This term is estimated using the mean velocity and distance between planes.

The inlet plane (B) temperature profile was recalculated using Equation 2, with hot regions becoming hotter and cold regions becoming colder, until the difference between CFD and experiment at Plane C was minimized and a third solution was converged. The resulting temperature maps at the Plane C vane inlet are shown in Fig. 20.

This new temperature boundary condition (Plane B) was then applied to the second CFD geometry that included the vanes (Fig. 19b), under the assumption that while the addition of the vanes would certainly change the flow at Plane C, the change to the flow four axial chords upstream at Plane B would be minimal. This new solution applied the new temperature boundary condition with a constant total pressure for the subsequent deposition simulations. The process was repeated for both the hot streak condition and the baseline case (without hot streaks).

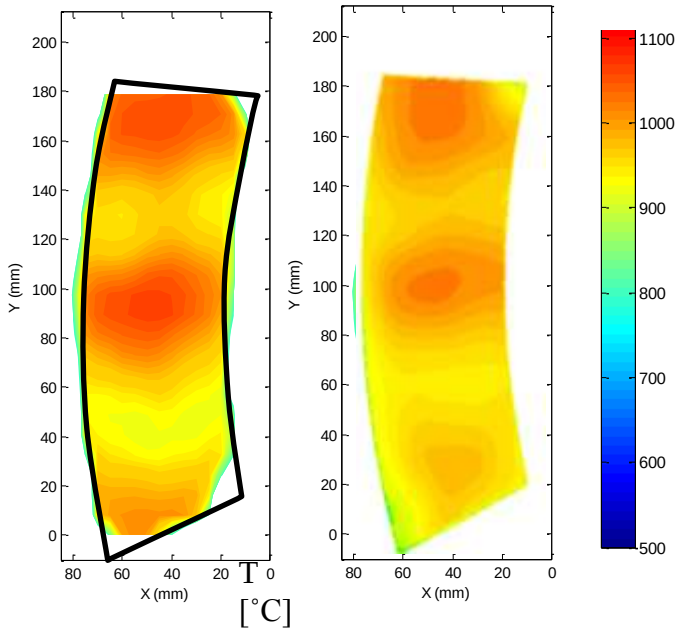


**Figure 20 - Temperature map [˚C] at the Plane C vane inlet (a) measured at Plane C in TuRFR and (b) in CFD through projection method.**

## Particle Tracking Model

The particle trajectory modeling was done using the Discrete Phase Model (DPM) module in Fluent. The DPM module allows for flow induced forces to be computed as they determine the flow path of the particles. Fluent predicts the trajectory of a discrete phase particle by the balance of particle inertia with the forces acting on the particle.

The Eulerian-Lagrangian model splits the particulate modeling into two phases. The first phase (Eulerian) is generating the flow solution absent of particulate. The flow solution phase is treated as a continuum and the Navier-Stokes equations are solved throughout the fluid domain. The second phase is tracking a large number of dispersed particles traveling through the flow. The trajectory of each particle is predicted and can be stored for analysis.

The particles in this study were injected at evenly spaced locations across the inlet boundary at Plane B, far enough upstream to allow for turbulent diffusion before reaching the regions of interest. A 20 x 10 grid at the inlet was used for the geometry. Particles were assumed to be in thermal equilibrium with the flow at the inlet and were injected at the local flow velocity.

### CRITICAL VISCOSITY MODEL

Given that the current initiatives to develop an improved sticking model are still in process, the sticking model developed by Tafti and Sreedharan was used for this study. The model assumes the particle viscosity changes with temperature and the relationship can be predicted based on the coal ash properties. The ash softening temperature is assumed to be the critical sticking temperature, $T_S$. Particles above this temperature are assumed to have a sticking probability of one. Particles with temperatures less than the critical sticking temperature will have a sticking probability based on the following function

$$P_s(T_P) = \frac{\mu_{crit}}{\mu_{T_P}} \quad [3]$$

The viscosity –temperature relationship is give by:

$$\log\left(\frac{\mu}{T_P}\right) = A + \frac{10^3 B}{T_P} \quad [4]$$

where *A* and *B* are constants which depend on the chemical composition. Senior and Srinivasachar [16] conducted experimental tests to develop a curve fit for determining *A* and *B*.

### COAL ASH PROPERTIES

The ash used for this study was JBPS subbituminous ash, with composition shown in Table 2.

**Table 2 – JBPS Coal Ash Composition**

| Element Weight % | | | | | | | | | |
|---|---|---|---|---|---|---|---|---|---|
| $SiO_2$ | CaO | $Al_2O_3$ | $Fe_2O_3$ | MgO | $TiO_2$ | SrO | $SO_3$ | $K_2O$ | $Na_2O$ |
| 49.9 | 9.4 | 11.5 | 14.5 | 1.7 | 3.0 | 0.7 | 1.2 | 1.6 | 3.7 |

The density of the particulate was measured to be 2320 kg/m$^3$. The specific heat and thermal conductivity were assumed to be 984 J/kg-K and 0.5 W/m-K respectively. For the critical viscosity model, the elemental composition in Table 2 was used to calculate the model coefficients, which were *A* = -11.31 and *B* = 15.96. The critical sticking temperature was assumed to be 1422 K, which was the temperature at which point the ash experienced significant sintering and melting in a thermal expansion test. These are summarized in Table 3.

**Table 3 – JBPS Coal Ash properties**

| Density ($kg/m^3$) | Specific Heat (J/kg-K) | Thermal Conductivity (W/m-K) | Diameter (μm) | Viscosity Model Constants | | Critical Sticking Temperature (˚K) |
|---|---|---|---|---|---|---|
| | | | | A | B | |
| 2320 | 984 | 0.5 | 2 – 20 | -11.31 | 15.96 | 1422 |

The size distribution is shown in Fig. 21, showing that the particle diameter ranges from about 2 – 20 μm, which corresponds to particle Stokes numbers of 0.04 – 5.1. The Stokes number is defined as

$$St_k = \frac{\rho_p d_p^2 V_i}{18 \mu l_c} \qquad [4]$$

Where $\rho_p$is the particle density, $d_p$ is the particle diameter, and $\mu$ is the fluid viscosity. $V_i$ is a characteristic velocity and $l_c$ is a characteristic length scale. For this study $l_c$ is the vane leading edge diameter [1.65 cm] and $V_i$ is the average axial velocity at the inlet of the vane passage [79 m/s]. Particles with a Stokes number much less than unity follow trajectories dominated by drag forces and closely follow the fluid pathlines. Particles with a Stokes number much greater than unity follow trajectories dominated by inertia and deviate from fluid pathlines.

**Flow characterization**

For each test in this study, the total mass flow and core flow temperature were held constant. The temperature of the gas was measured upstream of the dilution jets and held constant at 1366˚K. The flow at the vane cascade has an exit Reynolds number of 152,000 based on chord length. The vane pressure ratio is 0.79 and the exit Mach number is approximately 0.6. The total mass flow was held at 0.363 kg/s. In the instances when the hot streak was applied, a percentage of the mass flow was diverted from the main combustion flow to the dilution jets, so that the mass flow through the vane cascade was unchanged.

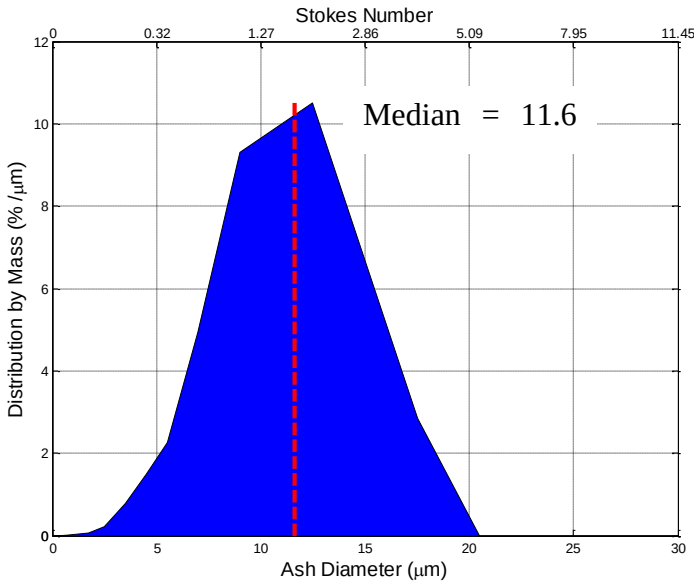


**Figure 21 - JBPS ash size distribution used in experiments. Computations used uniformly sized particles of 11.6 μm diameter, equal to the mass median diameter.**

To characterize the flow downstream of the dilution jets, temperature maps were acquired at Plane C without the vanes installed. These temperature maps showed that the dilution jets result in two distinct cold streaks downstream of the jets, framing a hot streak in the center, as shown in Fig. 20. Though Plane C was inaccessible with the vanes installed, infrared images confirmed that the surface temperature of Vane 2 consistently decreased with increasing levels of dilution flow.

**Experimental Deposition on Turbine Vane**

Temperature maps were acquired for several dilution rates without the vanes installed. It was determined that a total dilution mass flow rate of 10% was sufficient to create distinct hot streaks, with 5% supplied to each side. Two temperature profiles are shown in Fig. 22.

The profile in Fig. 22(b) shows distinct "cold streaks" corresponding to the dilution jets with a hot streak in the center. After this flow was characterized, several tests were run with the vanes installed and particulate injected. Two deposition tests were run with no dilution to serve as baseline cases. Two tests were run with 5% of the mass flow supplied as dilution to each side. An additional test was performed with 2.5% dilution to each side. The results of the deposition tests are tabulated in Table 4. After each test, the vanes were scanned and the deposit from Vane 3 (hot vane) and Vane 2 (cold vane) was measured. The table shows the hot vane consistently accumulated more deposit than the cold vane in each of the hot streak tests, while the vanes accumulated similar amounts of deposit in the baseline cases. Capture efficiencies are defined as the deposit accumulated on each vane relative to the total mass of particulate matter injected into the system, divided by four (because of the four vane passages).

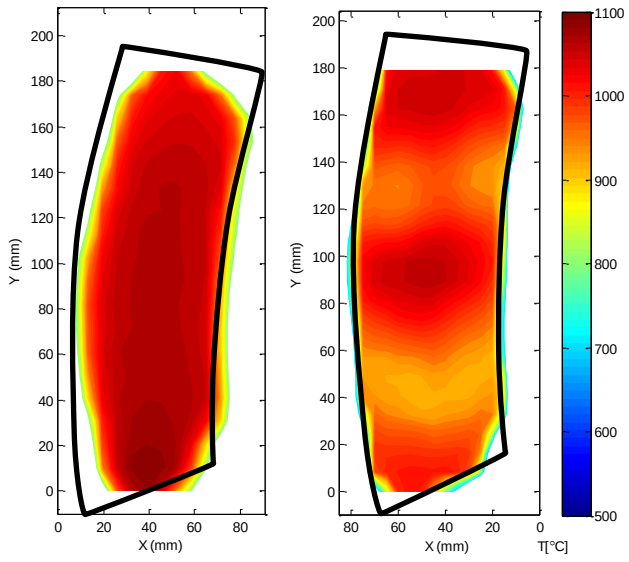


**Figure 22 - Temperature maps [˚C] at Plane C without vanes installed for (a) 0% dilution and (b) 5% dilution.**

Post-test photographs and thickness scans are shown in Figs. 23 & 24. Thickness scans show that in all cases, deposit is thickest at the leading edge and trailing half of the pressure surface. No deposit accumulated on the suction surface in any of the tests. Unfortunately, large-scale deposits on the leading edge flaked off of the vanes prior to scanning for the baseline cases,

(but the mass was still measured), thus leading edge deposition is not accurately represented in Figs. 23 & 24. Minor flaking also occurred at the trailing edge, seen while monitoring the test by video. This deposit was lost before measuring, and led to increased variability in the results.

**Table 4 – Experimental Hot Streak Deposition Results**

| | Test A | Test B | Test C | Test D | Test E |
|---|---|---|---|---|---|
| Mass Flow Rate (kg/s) | 0.363 | 0.363 | 0.363 | 0.363 | 0.363 |
| Cold Jet Flow Per Side % | 0 | 0 | 2.5 | 5 | 5 |
| Core Flow Temperature (˚C) | 1093 | 1093 | 1093 | 1093 | 1093 |
| Total Ash Injected (g) | 97.9 | 93.7 | 95.7 | 117 | 108.5 |
| Deposit on Vane 2 (g) | 0.46 | 0.55 | 0.22 | 0.09 | 0.06 |
| Capture Efficiency Vane 2 (%) | 1.88 | 2.35 | 0.92 | 0.31 | 0.22 |
| Deposit on Vane 3 (g) | 0.56 | 0.42 | 0.34 | 0.43 | 0.43 |
| Capture Efficiency Vane 3 (%) | 2.29 | 1.79 | 1.42 | 1.47 | 1.59 |
| Capture Efficiency Ratio - Vane 3 to 2 | 1.22 | 0.78 | 1.55 | 4.78 | 7.17 |

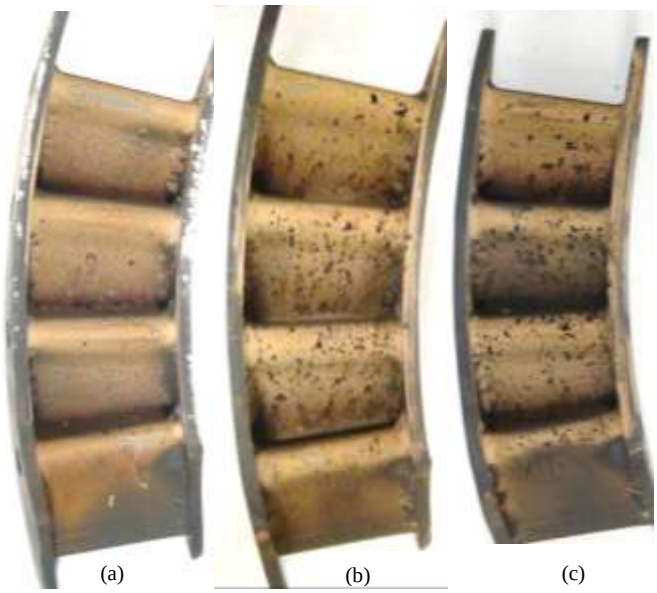


**Figure 23 - Post-test photographs of deposition with (a) 0% dilution, (b) 2.5% dilution and (c) 5% dilution.**

Photographs in Fig. 23 show that a majority of the leading edge and pressure surface accumulated at least a thin layer of deposit, with only minor variation in the span-wise direction. Experimental scans of the deposits, taken from tests B and E, (Fig. 24) reveal that peak deposits

occur at the leading edge, evidenced despite the flaking cited earlier. Scans also reveal that for the baseline case, a narrow band on the pressure surface just downstream of the leading edge is nearly devoid of particulate.

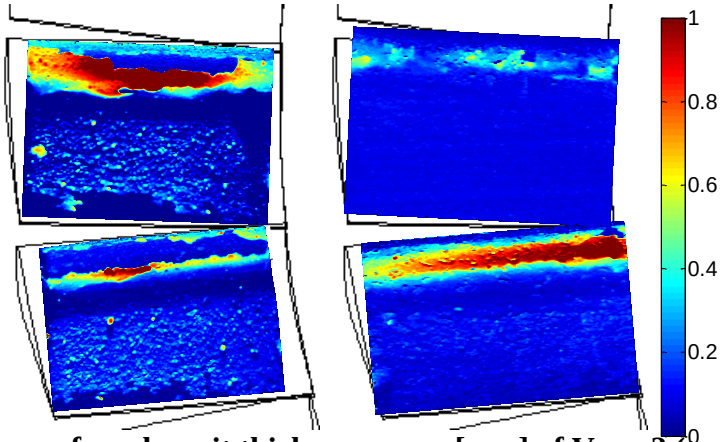


**Figure 24 – Pressure surface deposit thickness scans [mm] of Vane 2 (top) and Vane 3 (bottom) from baseline test (left) and 5% dilution (right).**

Chord-wise traces of deposition thickness at midspan were extracted from both the experimental scans and computational predictions. Figure 25 shows a comparison of these deposition thicknesses from the baseline and 5% dilution tests for Vane 2 and Vane 3, normalized by the respective mass of ash injected. Experiments show deposition peaks at the leading edge and a thin layer over the pressure surface, thicker toward the trailing edge. For the experiments, trailing edge deposit flaked off beyond about 80% chord.

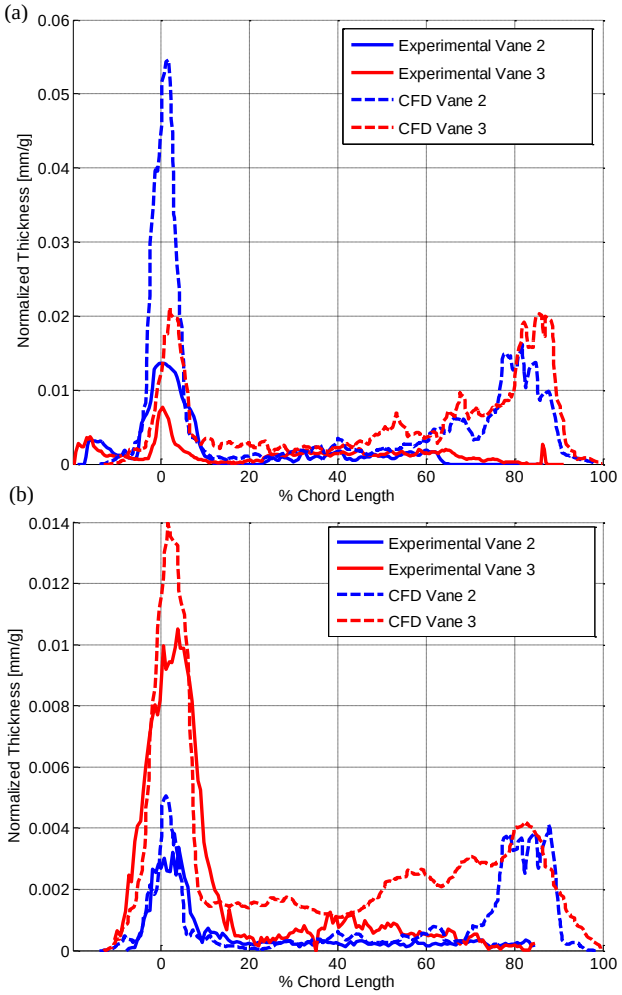


**Figure 25 - Midspan chord-wise traces of deposition rates for (a) baseline case and (b) 5% dilution, CFD vs. experiment on Vanes 2 and 3**

## Computational Flow Solution

Each experimental test was reproduced computationally by imposing the measured temperature map as the thermal boundary condition, following the projection method discussed previously. The inlet was specified as a pressure inlet, with values chosen to match the total mass flow rate used in the experiment. Once the desired temperature profile for the inlet was found, and the solution with vanes installed was converged, deposition was simulated. The number of particles used in each case was sufficiently large such that the results were statistically averaged, forming a representative solution from which deposition locations and rates were extracted. Table 5 lists the details and results of each simulation. The corresponding surface temperatures of the vane set for each simulation are shown in Fig. 26.

**Table 5 - Numerical Hot Streak Deposition Results**

| | Baseline | 5% Hot Streak |
|---|---|---|
| Mass Flow Rate (kg/s) | 0.363 | 0.363 |
| Cold Jet Flow % | 0 | 5 |
| # Particles Injected | 400,000 | 400,000 |
| Capture Efficiency on Vane 2 (%) | 18.41 | 3.34 |
| Capture Efficiency on Vane 3 (%) | 21.17 | 9.50 |
| Capture Efficiency Ratio- Vane 3 to 2 | 1.15 | 2.84 |

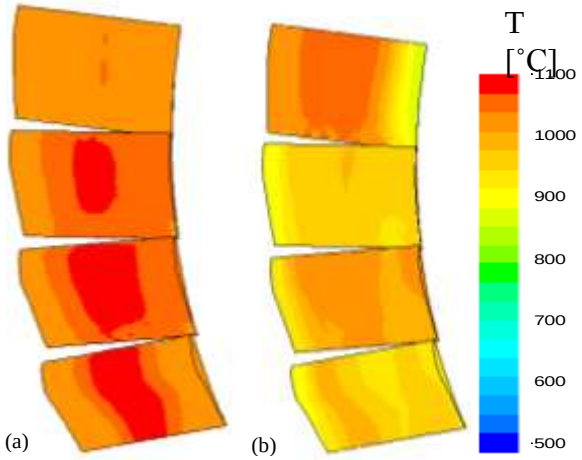


**Figure 26 - Computed surface temperatures [˚C] on Vanes 2 and 3 for (a) baseline case (b) 5% dilution hot streak.**

The vane surface temperatures for the baseline case are relatively uniform with a slightly higher temperature on Vane 3. These variations in temperature are a result of both the small non-uniformities inherent in the facility and any errors associated with the projection method. The effect of the hot streak in Fig. 26(b) (see Fig. 22(b)) is clear, showing that vanes 1 and 3 have higher average temperatures than vanes 2 and 4. The vane surface temperatures shown in Fig. 26(b) give a good approximation of the flow and particle temperatures before they impact the vane.

Deposition rates on the vanes were calculated and are shown in Fig. 27 and Table 5. While the deposition pattern predicted by the computational model for the baseline test does not match the experimental results exactly, there are several similarities. Fig. 27(a) shows deposition with minor variation in the span-wise direction on the majority of the two center vanes. This result is expected, as the temperature profile at the inlet is relatively uniform, and the same trend is seen in the experimental tests. The experiment (Fig. 24) also shows elevated deposition on the leading edge and the trailing half of the pressure surface, caused by an elevated number of particle impacts in these regions. Particles impact the leading edge due to inertia. Particles are also known to rebound off of the leading edge and impact the trailing edge of an adjacent vane.

For the computations, all of the particles were the same size. A distribution identical to the experiment would show more variation in particle trajectories, leading to more variation in particle impacts and deposition.

While the spatial distribution of deposition predicted by the model matches relatively well, there is a significant difference between the capture efficiencies predicted for each vane and those measured experimentally. Figure 25(a) shows that the chord-wise trends in both computational and experimental deposition correspond reasonably well, however, the peaks at the leading and trailing edges predicted by the model are much higher than the values obtained from the scan. This may be due, in part, to the flaking that occurs in these regions during cool down in the experiment. Though every effort is made to catch the flaking deposit before it is lost so it can be included in the deposit capture efficiency estimate, it is not included in the thickness scan. The computational model may under predict particle detachment due to shear at the trailing edge where the velocities are highest. Another consideration is that the CFD model uses adiabatic walls, while the experiment suffers from reduced trailing edge temperatures due to conduction from the pressure to suction surface (which radiates to ambient). The experimental and computational capture efficiencies for the baseline tests, listed in Tables 4 & 5, also show that the computational model predicts roughly nine times higher amounts of deposition for each vane than what is measured. Clearly the sticking model over predicts deposition at these temperatures. It should be noted that only the pressure surfaces are shown in Fig. 27 as no deposition was predicted on any of the suction surfaces, consistent with the experiments.

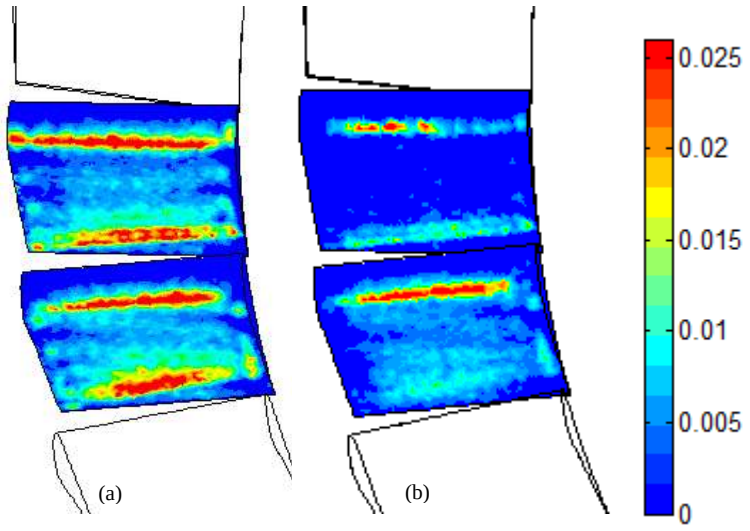


**Figure 27 - Computed deposition rates [mm/g] on Vanes 2 and 3 for (a) baseline case (b) 5% dilution hot streak**

The computational model for the 5% dilution case [Fig. 26**Error! Reference source not found.**(b) and Fig. 27(b)] predicts higher amounts of deposition on the hot vane compared to the cold vane, which agrees with Tests D and E. The largest peaks occur at the leading edge, with limited deposit on the pressure surface, and deposition rates are relatively uniform in the spanwise direction. The experimental data for both vanes show that a majority of the deposit is concentrated at the leading edge. The computations also predict a peak at the trailing edge which is not seen experimentally.

Similar to the baseline case, the computational model overpredicts total deposition rates compared to the experiments, with six times the predicted rate on the hot vane and ten times the predicted rate on the cold vane. The capture efficiency ratio between vanes 2 and 3 (Table 5) is also much smaller than what is measured in the experiments (Table 4).

The critical viscosity sticking model, while showing that deposition is elevated at higher temperatures, does not account for other potentially important variables, such as particle size or impact velocity. As an example, for the difference in peak inlet temperature [Fig. 26(b)] from the hot streak to the cold streaks, the respective sticking probabilities are separated by a factor of 50. This illustrates the sensitivity of the sticking model to temperature. Small changes in the temperature profile at plane B can significantly alter the resultant deposition rates predicted on the vanes. These experiments suggest that the effect of temperature on deposition is much less severe than predicted by the model.

A successful computational simulation of turbine deposition relies on the accuracy of four critical parts: turbine geometry, flow solution, particle tracking method, and particle sticking/rebound model. Since the experimental geometry was replicated exactly in the computations, and given the established accuracy of the flow and particle tracking models in Fluent, it is evident that the sticking model is primarily responsible for the discrepancies between experiments and computations noted above. While previous research has made use of the critical viscosity model in nearly isothermal simulations, this is the first deposition study that incorporates large temperature variations in both experiments and computations, thus exposing the sticking model's lack of robustness. An attempt was made to tune the sticking model coefficients ($A$, $B$, and $T_S$) in order to better match experimental results. The result is illustrated in Fig. 28.

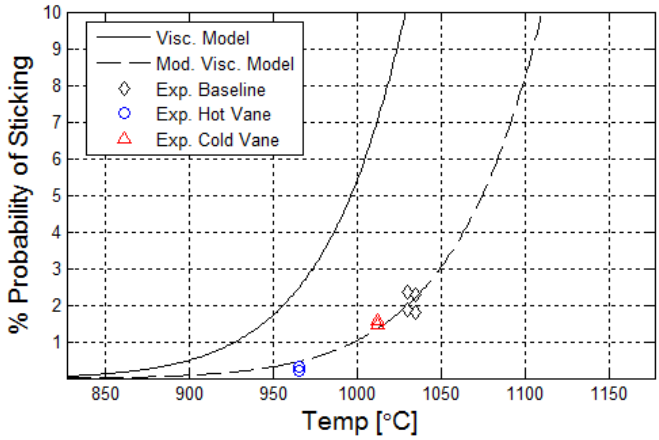


**Figure 28 - Comparison of sticking probabilities for the original and modified sticking models vs. experimental data.**

The experimental capture efficiencies from Tests A, B, D, and E in Table 5 are plotted in Fig. 28 vs. the vane surface temperatures taken from the corresponding flow solutions. The original sticking probability trend is seen to deviate substantially from the experiments. A new trend can be formed by modifying the viscosity model coefficients and calibrating the model to the experimental results. This modified model changes the $B$ coefficient from 15.96 to 16.3 and $T_S$ from 1422K to 1517K. Rerunning the deposit simulations with these new constants reduces the overall discrepancy between the experiments and simulations from a maximum factor of 900% to less than 25% for all experiments, which is comparable to the natural variation in

repeated experimental tests. While the model with these modified coefficients appears promising, the new values lack theoretical justification, and would not improve the accuracy in other simulations. In addition, the critical viscosity model includes no dependency of sticking on particle size or velocity; parameters which are known to be important for deposition. The new sticking model summarized at the beginning of this report does include these sensitivities and is now being implemented with this experimental data for validation.

**II: Deposition on a Cooled Vane:**

For this phase of the research effort, the annular test piece shown in Fig. 17 was modified to allow for slot cooling of Vane #3 (see Fig. 29). The diagram indicates which side coolant enters. This test article was used to perform multiple deposition studies with varying levels of coolant on the central vane (Vane #3) in the cascade. Table 6 summarizes the nominal test conditions.

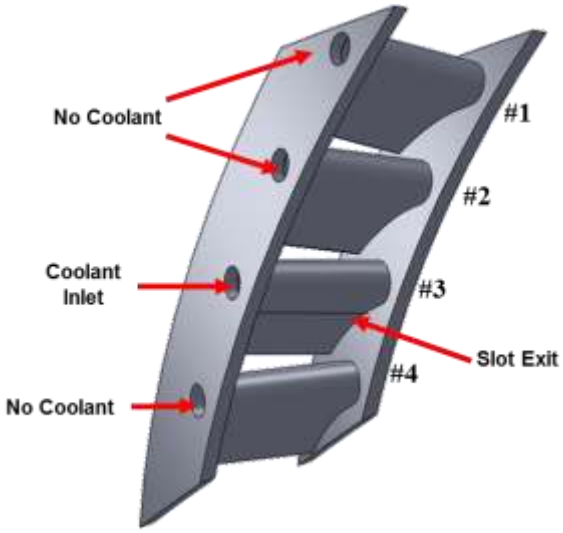


**Figure 29: Schematic of the annular test section**

**Table 6: Test conditions**

| | |
|---|---|
| Inlet Mass Flow Rate | 0.8 lbm/s |
| Nominal Inlet Flow Temp. | 1975 °F |
| Inlet Mach Number | 0.1 |
| Exit Re based on chord | 152,000 |
| Inlet Re based on LE diameter | 8,509 |

Coolant mass flow rate was held constant during each test, with several flow rates tested. The coolant is not actively heated, but is rather passively heated by the facility to reach a cooling cavity inlet temperature that depends on coolant flow rate. This temperature was measured for each coolant mass flow rate, and is accounted for in the results to allow appropriate comparison with CFD.

As coolant mass flow rate and temperature were varied between tests, a new variable is introduced to better capture the differences between tests and allow for comparison to other studies that have different facilities and test articles. The non-dimensional thermal capacity ratio is defined as,

$$\Phi = \frac{\rho_c u_c A_c (T_\infty - T_{c,i})}{\rho_\infty u_\infty A_s T_\infty}$$

where $\rho_c$, $u_c$, $A_c$ are the density, velocity and area at the slot exit. The temperature $T_{c,i}$ is the coolant temperature at the inlet to the cooling cavity. The variables with the '$\infty$' subscript are all evaluated in the free stream, and $A_s$ is the area of the surface being cooled. This parameter allows comparison of experiments with different free stream and coolant conditions, as well as different cooled-surface sizes (through $A_s$). The product $\rho_\infty u_\infty A_s$ scales with passage mass flow rate (or equivalent depending on the respective facility), thus $\Phi$ gives a measure of the thermal capacity ratio between the coolant and free stream. The thermal capacity ratio corresponding to each coolant mass flow rate is also listed in Table 7.

**Table 7: Cooling parameters**

| $\frac{\dot{m}_c}{\dot{m}_p}$ % | $T_{c,i}$ [K] | $Re_h$ | $DR(DR_{in})$ | $M(M_{in})$ | $\Phi$ |
|---|---|---|---|---|---|
| 0.62 | 926 | 172 | 1.13(1.54) | 1.16(1.58) | 0.00139 |
| 0.88 | 834 | 274 | 1.21(1.74) | 1.74(2.50) | 0.00245 |
| 1.27 | 705 | 434 | 1.30(2.31) | 2.67(4.37) | 0.00443 |

**Coolant Characterization Revisited**

To provide surface temperature data for comparison with CFD modeling predictions, infra-red imaging was employed as has been discussed in previous reports. Images for each flow rate are shown in Fig. 30.

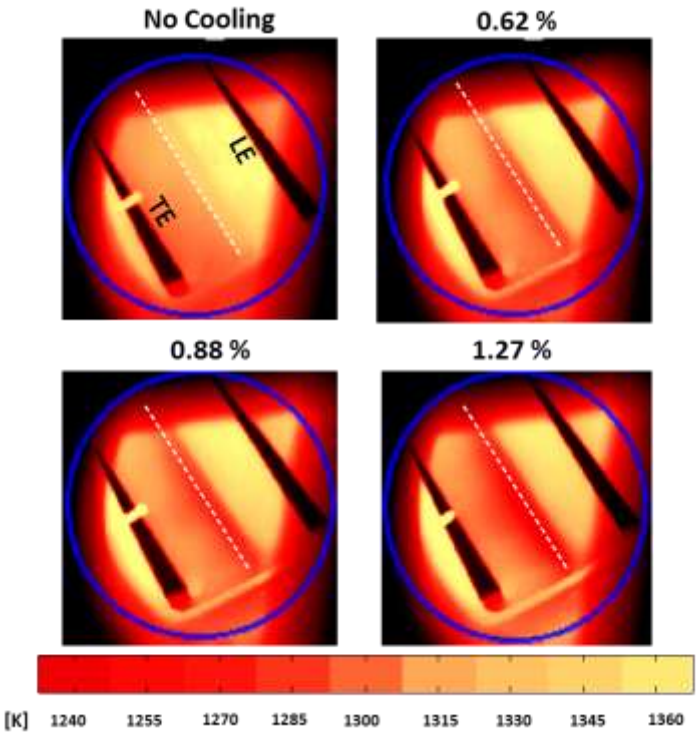


**Figure 30: IR images of the pressure surface at different mass flow ratios. Coolant enters from the lower right hand side of the vane.**

Converting these IR images into surface temperatures allows for proper characterization of the slot cooling scheme by examining the film cooling effectiveness at the different coolant mass flow rates. As the coolant temperature at the inlet to the cooling cavity varies with coolant flow rate (the coolant is passively heated by the facility), a non-dimensional parameter was defined to account for both the coolant inlet temperature and local variations already present in the baseline,

$$\theta = \frac{T_{St} - T_{s,c}}{T_{s,b} - T_{c,i}} - \frac{T_{St} - T_{s,b}}{T_{s,b} - T_{c,i}} = \frac{T_{s,b} - T_{s,c}}{T_{s,b} - T_{c,i}}$$

where $T_{St}$ is the stagnation temperature, $T_{s,b}$ is the surface temperature for the baseline non-cooled test, $T_{s,c}$ is the surface temperature for the cooled test investigated, and $T_{c,i}$ is the respective coolant inlet temperature. By normalizing the temperature difference by the relevant coolant inlet temperature and subtracting the baseline term, this parameter provides the cooling effectiveness relative to the local baseline temperature and respective coolant inlet temperature.

**Computational Simulations**

Numerical simulations of the slot cooled vane were conducted using the commercial finite volume package FLUENT. Steady, 3D RANS simulations were run, using measurements from the experimental tests as boundary conditions, in an attempt to match the experimental conditions as closely as possible.

**Computational Domain and Mesh**

The domain consists of two half passages, one on either side of the cooled vane. Periodic boundary conditions were implemented to simulate the cascade condition. The passage, cooling cavity, slot, and the solid vane were all meshed to allow for conjugate heat transfer calculations. The main inlet of the domain was located approximately one chord upstream of the vane leading edge, with the outlet a similar distance from the trailing edge.

Mass flow rate and total temperature were specified at the main flow and coolant inlets, with static pressure specified at the outlet. The endwalls were set as adiabatic walls. The $k-\omega$ SST turbulence model was employed, with turbulence intensity and length scale specified at both inlets (5% and 0.1m at main inlet, 3% and 0.0125m at coolant inlet). Temperature dependent polynomials were specified for the relevant properties of air and Inconel.

A 2D hybrid mesh was initially created, and consisted of unstructured tetrahedral cells and pseudo-structured anisotropic tetrahedrals near the external walls that form a boundary layer mesh. This was achieved by using the anisotropic tetrahedral extrusion capability of Gridgen 15, and provides a low cost, high quality boundary layer mesh. The mesh was also refined on the vane-side of the walls to better predict wall heat transfer. The 2D mesh was extruded in uniform steps to create the 3D grid, depicted in Fig. 31. The 3D grid thus retains the anisotropic boundary layer mesh at relatively low cost in cell count. In this `coarse' mesh, the regions of interest were not sufficiently resolved, resulting in irregularities in the heat transfer results. The mesh was refined in these areas to create a `medium' mesh, eliminating the issues present in the coarse mesh. To further examine sensitivity, a `fine' mesh was constructed by increasing the number of cells by 25%. Chordwise traces of surface temperature at midspan of the medium and fine grids were compared and temperatures were within 1-2\% over the whole chord. The medium mesh was thus used for computations presented in this study. The details of each mesh are provided in Table 8.

**Table 8: Mesh details**

| Mesh | Number of Cells | $y^+$ |
|---|---|---|
| 2D | 110,730 | <1 |
| 3D Coarse | 2,980,451 | <10 |
| 3D Medium | 4,683,120 | <2 |
| 3D Fine | 5,870,670 | <1 |

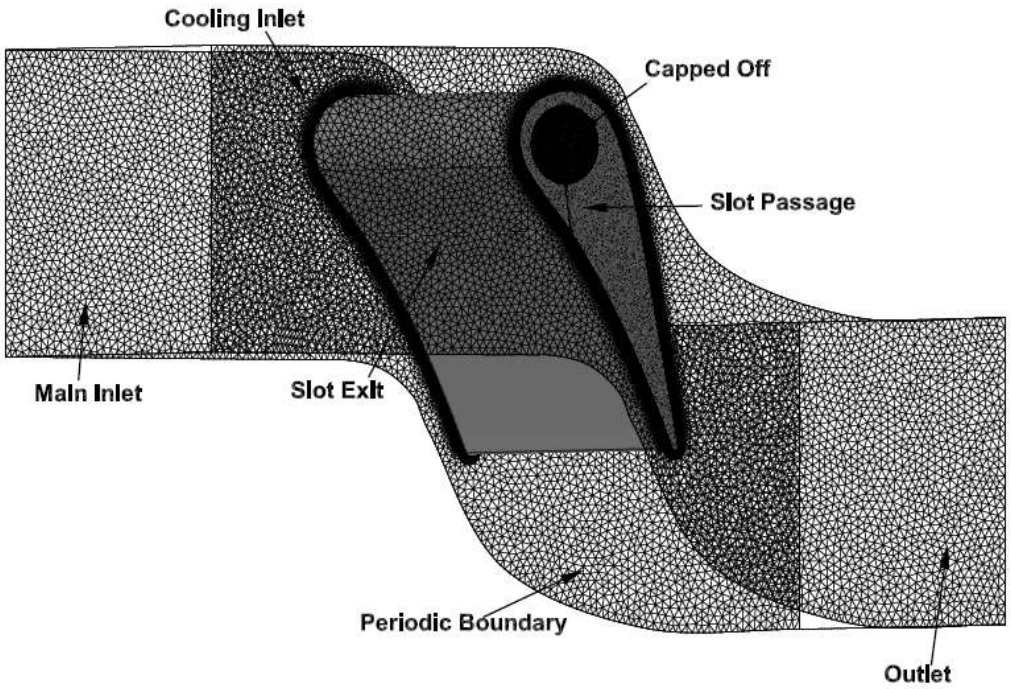


**Figure 31: Computational domain and mesh**

## Computational Flow and Heat Transfer Results

Three dimensional, steady computational flow and heat transfer calculations were performed to reproduce the experimental tests for each coolant flow rate. Contours of Mach number in a midspan slice are shown in Fig. 32. Figures 33 and 34 show non-dimensional temperature contours for the $\Phi = 0.00443$ case. The temperature distribution within the vane is shown in Fig. 33 and gives an idea of the large amount of conduction occurring between the slot-passage and vane pressure surface. The coolant picks up a considerable amount of heat in the passage and exits at a higher temperature. The spanwise non-uniformity in surface temperatures present in Fig. 34 are qualitatively similar to what is observed in experimental results. Examining the predicted slot exit velocity at various spanwise locations confirmed that the cooling cavity is plenumized, and that the temperature non-uniformity along the span is caused by the coolant picking up heat along the span rather than exiting at different velocities. Assuming no leaks in the facility, this conclusion could apply to experimental results as well. The surface temperature contour map also shows the effectiveness of the slot passage in cooling the region just upstream of the slot, also observed in IR data and experimental deposition results.

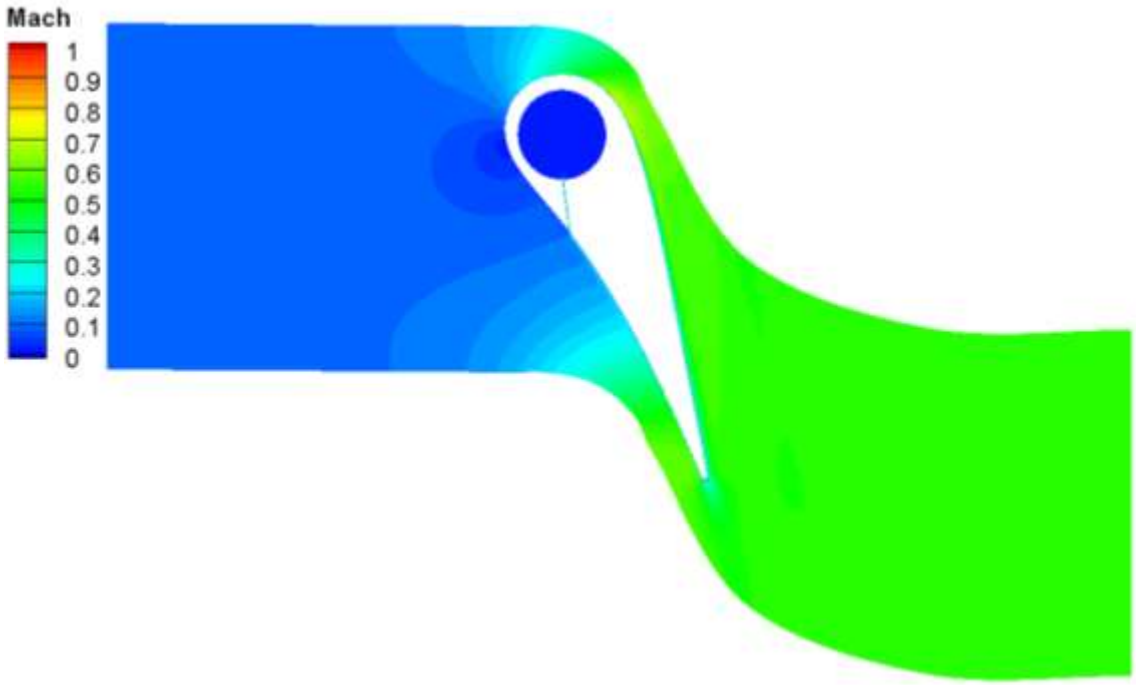


**Figure 32: Contours of Mach number in a midspan slice for Φ = 0.00443**

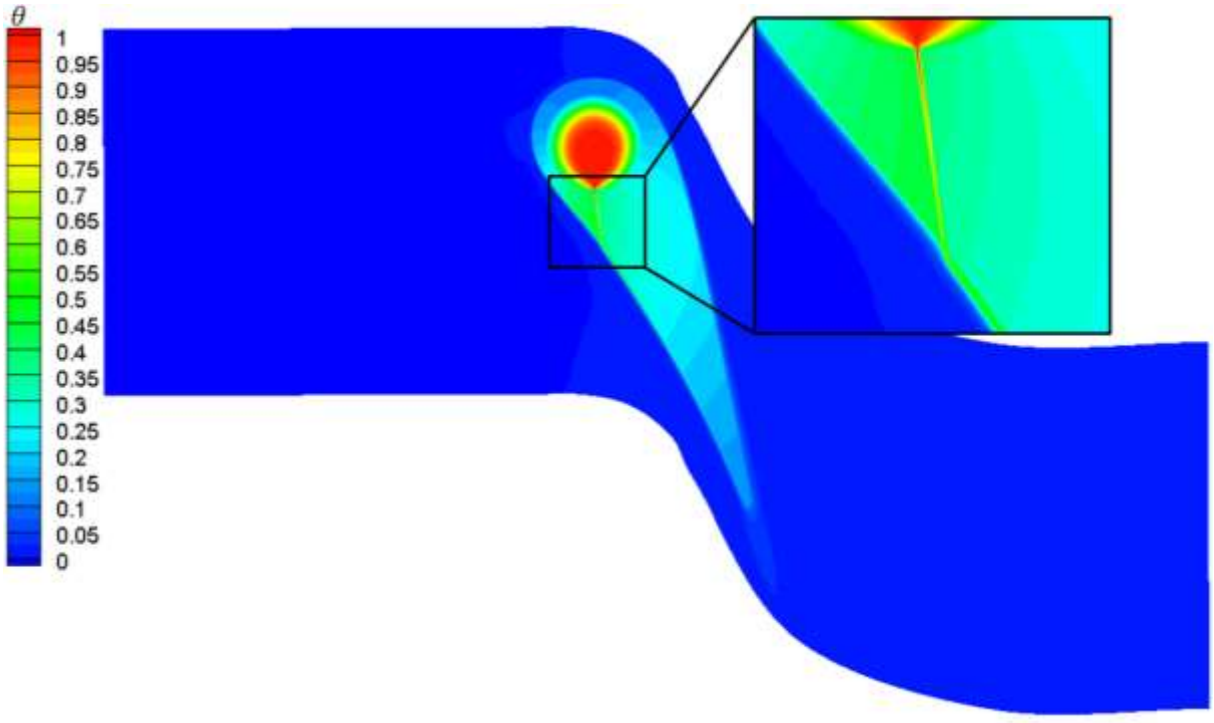


**Figure 33: Contours of $\theta$ in a midspan slice for Φ = 0.00443**

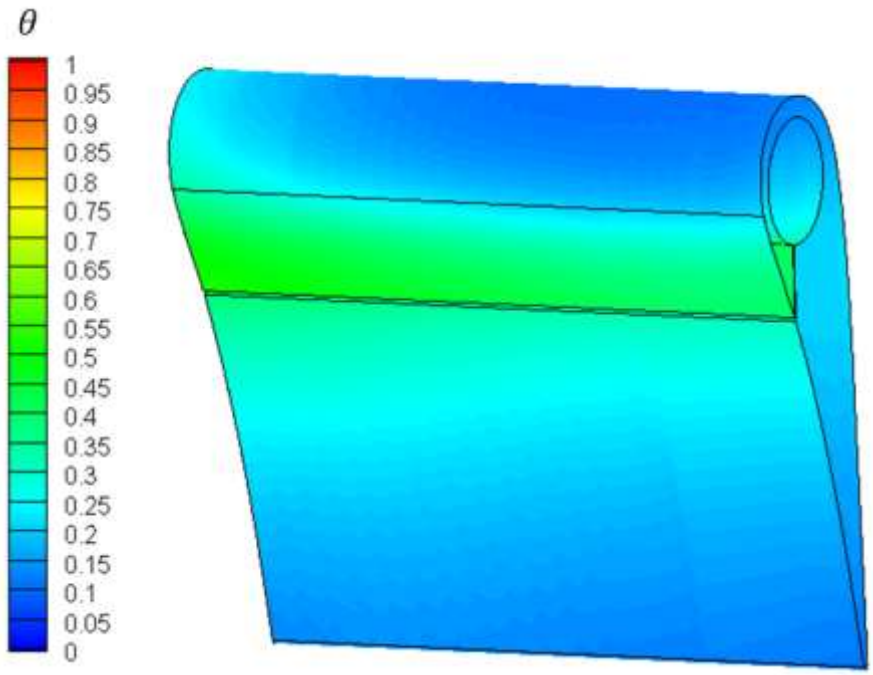


**Figure 34: Contours of $\theta$ on the vane pressure surface for $\Phi$ = 0.00443. Coolant enters on the left hand side.**

Chordwise linear traces of $\theta$ were compared to experimental measurements, presented Fig. 35. The CFD clearly over predicts the effectiveness of the cooling scheme, especially in the region just upstream of the slot. In addition to the disparity in magnitudes, the jump in effectiveness over the slot is exaggerated in the computational prediction. There are several factors that could contribute to this mismatch. There may be more coolant mass flow being simulated than what occurs in the facility, resulting in higher convection heat transfer in the slot passage and thus lower surface temperatures through conduction. As the measured coolant mass flow rate was applied as a boundary condition, this would only occur if leaks were present in the facility during testing. Though every effort was made to seal the coolant line, this possibility cannot be entirely ruled out; though there was no physical evidence of leakage. Alternatively, external heat transfer to the blade may be under predicted by the code. The predicted decrease in effectiveness trend over the trailing portion seems to match the trend in experimental results relatively well, though the values are still over predicted.

An order of magnitude analysis shows that radiation heat transfer contributes a considerable portion of the heat balance, and is not modeled in the simulation. The inclusion of radiation modeling would improve the match between experimental results and CFD predictions in Fig. 35. As the majority of the pressure surface of the vane faces the internal walls of the TuRFR test section and combustion chamber, the surface would most likely be `seeing' a higher temperature. If accounted for in CFD, the non-linear temperature dependence of radiation ($T^4$) would then cause the surface temperatures to be raised by different amounts. This would not only raise the magnitude of surface temperatures but also lower the jump in temperature over the slot. It seems the modeling of radiation is absolutely necessary for the accurate prediction of heat transfer in a facility such as the TuRFR. Unfortunately the radiation models included in

FLUENT are either incompatible or not suitable for this problem, which includes periodic boundary conditions and conjugate heat transfer. An attempt to model external radiation to the vane as a source term using a UDF encountered convergence problems and a satisfactory solution was not obtained. Radiation modeling was thus not included in these simulations.

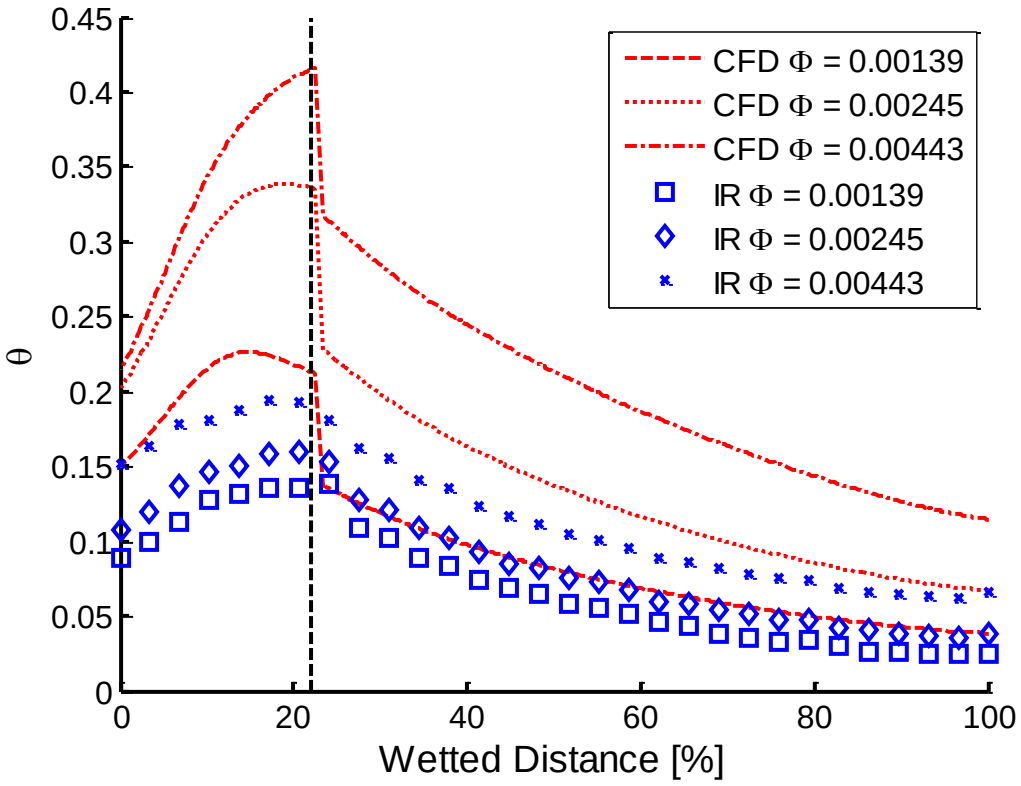


**Figure 35: Chordwise linear traces of $\theta$ at midspan**

**Computational Deposition Results**

Experimental deposition tests were repeated computationally using the particle tracking and sticking models already described. As particles are tracked in a Lagrangian fashion, it would be prohibitively expensive to simulate a number of particles on the order to that injected into the facility during a test. Thus a sufficiently large number of particles was used to produce capture efficiency rates independent of the number of particles injected. Initially, the model severely under predicted capture efficiency. By lowering the critical sticking temperature from 1422 K to 1380 K, improved predictions of deposition were obtained. Capture efficiencies (CE) for each simulation with the altered critical sticking temperature are listed in Table 9 with corresponding experimental results. The capture efficiency for the baseline, $\Phi$ = 0.00139, and $\Phi$ = 0.00245 cases was under predicted by the model, and over predicted for the $\Phi$ = 0.00443 case. The capture efficiency ratio to the baseline was consistently under predicted. This suggests that the sticking model is not sufficiently sensitive to the changes in temperature between each test. Additionally, the critical viscosity model has no dependence on the temperature of the surface

that the particle impacts. This could also contribute to the under prediction of capture efficiency reduction factors in each test. Tuning the model parameters A, B, and $T_s$, as was done in the hot streak study reported above, can improve capture efficiency predictions. However, the alterations do not have any theoretical justification and are only valid for the experiment upon which they were calibrated. This is not a desirable approach when a computational model with the ability to predict deposition without conducting experiments is the goal. Thus the inclusion of a surface temperature dependency seems the more prudent approach.

**Table 9: Computational deposition results**

| Φ | Exp | | CFD | |
|---|---|---|---|---|
| | $CE_{vane\ 3}$ [%] | $CE_{base}/CE_{vane\ 3}$ | $CE_{vane\ 3}$ [%] | $CE_{base}/CE_{vane\ 3}$ |
| 0 | 3.09 | 1 | 2.10 | 1 |
| 0.00139 | 2.06 | 1.41 | 1.72 | 1.22 |
| 0.00245 | 1.37 | 2.30 | 1.61 | 1.30 |
| 0.00443 | 0.89 | 3.33 | 1.43 | 1.47 |

## III: Deposition with Hot Streaks on a Cooled Vane:

This phase of the research effort represents the culmination of the previous two studies: deposition with hot streaks and deposition with coolant. As such, three different test conditions were considered in this test plan. First, a baseline case with no dilution air (no hot streak) and no film cooling. For this case, the vanes are subjected only to the temperature non-uniformities present in the facility due to combustion and other effects. The second test case utilizes dilution air to produce a hot streak, with Vane 3 remaining uncooled. The third case considers both a hot streak and film cooling. The test conditions are summarized in Table 10 with corresponding labels that are used throughout the following sections.

**Table10: Test cases.**

| Test | Hot Streak | Film Cooling | $\dot{m}_{dil}/\dot{m}_{inlet}$ |
|---|---|---|---|
| B | × | × | 0 |
| HS | ✓ | × | 7.2% |
| HS+FC | ✓ | ✓ | 7.2% |

The simplified Rolls Royce research profile vane cascade was again used as the test piece in these experiments. This vane set is shown again in Fig. 36 for reference to the cooling geometry. As indicated in the figure, only one of the vanes (Vane 3) is cooled. The coolant supplied to this vane is not actively heated, but is rather passively heated by the facility to reach a cooling cavity inlet temperature. To characterize the coolant flow, the density ratio and blowing ratio are defined as,

$$DR = \frac{\rho_c}{\rho_\infty}$$
$$M = \frac{\rho_c u_c}{\rho_\infty u_\infty}$$

Note that because the slot has a large $L/h$ ratio of 28.7, there is a substantial amount of heat pick up in the slot passage, and the density ratio above will have significantly different values when referencing the cooling cavity inlet conditions and the slot exit conditions (for the numerator). Both values are thus reported, with $DR_{in}$ denoting the value based on cooling cavity inlet density. It should be noted that $DR_{in}$ is determined experimentally, while $DR$ is estimated using the CFD simulation. These values, as well as mass flow ratio and cooling cavity inlet temperature $T_{c,i}$, are listed in Table 11. Note that $T_{c,i}$ is measured at the inlet plane to the cooling cavity, not within the cavity.

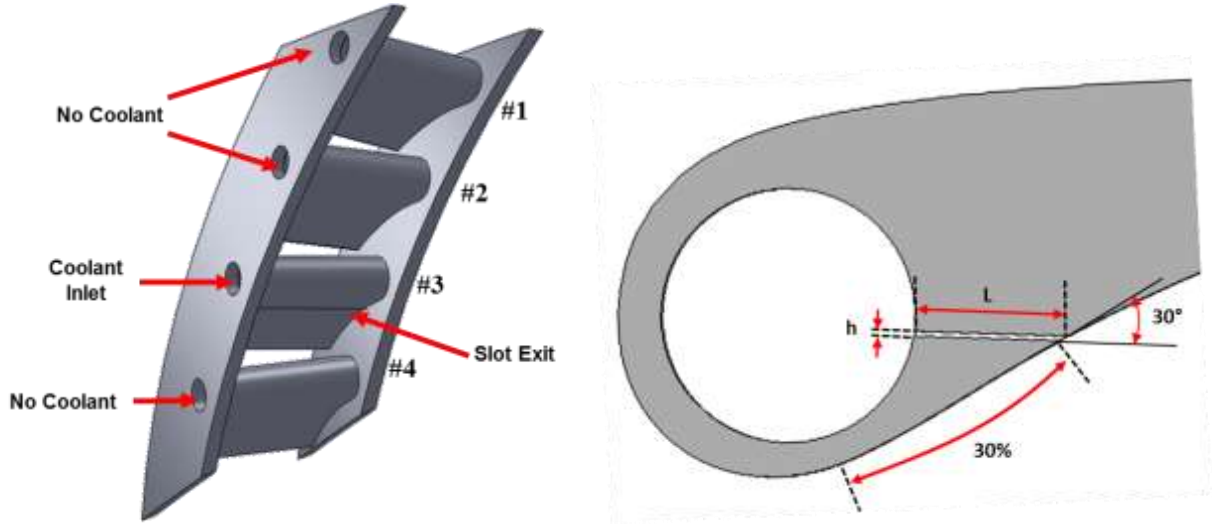


**Figure 36: Left: Schematic of the annular test section. Right: Diagram of cooling scheme.**

**Table 11: Cooling parameters.**

| h[mm] | L/h | $\dot{m}_c/\dot{m}_p$ | $T_{c,i}$ | $Re_h$ | $DR(DR_{in})$ | M |
|---|---|---|---|---|---|---|
| 0.254 | 28.7 | 1.27 | 705 | 434 | 1.30 (2.13) | 2.78 |

**Inlet Temperature Profiles**

The method used for obtaining temperature measurements just upstream of the vane inlet has been outlined previously. A final set of inlet temperature profiles for both the baseline and hot streak cases were thus acquired, and are shown in Fig. 37. The baseline profile is non-uniform in the pitchwise direction, with temperatures monotonically rising across the inlet in this direction. This non-uniformity is thought to be due to the combustion process upstream and geometry of the facility. The profile is relatively uniform in the spanwise direction. For the baseline case,

Vane 2 has a higher surface temperature than Vane 3, as it is exposed to the higher temperature flow.

Figure 37 also shows the inlet temperature distribution when the dilution jets are used. The effect is clear, with two cold streaks framing a distinct hot streak near the center. One of the cold streaks is at a higher temperature than the other, this is due to the underlying baseline profile. To quantify the relative effect of the dilution jets, the baseline profile is subtracted from the hot streak profile, producing the difference in temperature between the two cases. This is plotted in Fig. 37, and shows that while the top pair of jets are at a higher temperature than the lower pair, they have a larger effect relative to the baseline. The hot streak case produces higher surface temperatures on Vane 3 than on Vane 2, as the hot streak almost impinges on the leading edge of Vane 3, while Vane 2 is exposed to the cold streak.

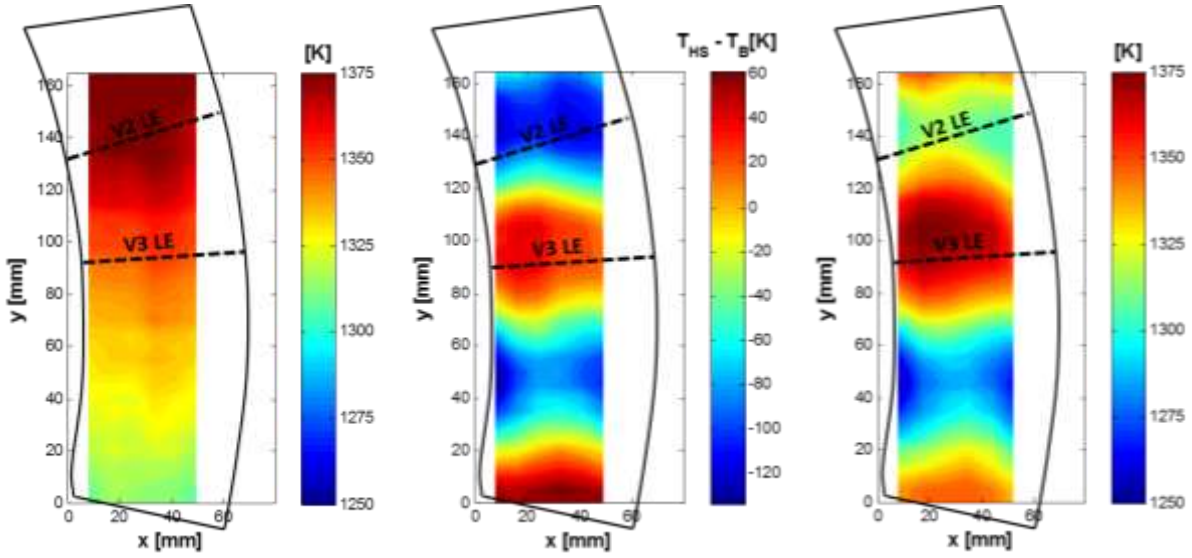


**Figure 37: Inlet temperature profiles overlaid on the inlet, with vane leading edge locations indicated. Left: Baseline, Middle: Hot streak, Right: Hot streak – Baseline.**

**External Deposition Results**

External deposition tests were conducted at the three test conditions (Table 10), with two tests at each case for repeatability. Ash was injected for 15 minutes for each test, at a constant rate, to attempt to keep the amount of ash injected similar between tests. This amount does vary in practice, due to the variability of the ash packing in the hopper used to introduce ash into the flow. After each test the deposit was removed from the vanes and weighed. Photographs of Vane 3 post-test from each of the three cases are provided in Fig. 38 as a visual example of typical deposit levels achieved. The deposit weights were used to determine the capture efficiency of each vane,

$$\eta_{v,i} = N\frac{m_{v,i}}{m_t}$$

where $m_{v,i}$ is the mass of deposit accumulated on `Vane $i$', $m_t$ is the total mass of particulate injected during the test, and $N$ is the number of passages in the annular test piece ($N$ = 4). Capture efficiencies for Vane 2 and 3, as well as their ratio, are listed for each test case in Table 12 and the ratios are plotted in Fig. 39. For the baseline tests, the capture efficiency of Vane 2 was higher than Vane 3, due to the non-uniform inlet temperature profile. Vane 2 is subjected to higher temperature flow in this condition, resulting in the increased capture efficiency. A ratio of Vane 2 to Vane 3 closer to unity would be an ideal baseline, this would require a more uniform baseline temperature profile however. Nevertheless, the results obtained for this test case are still useful, as the hot streak case is considered relative to this baseline. In the hot streak tests (HS1 & HS2) Vane 3 is subjected to the hot streak, while Vane 2 experiences colder flow from the dilution jets. The capture efficiency ratio is significantly different from the baseline, with a Vane 3 capture efficiency around twice that of Vane 2. The effect of the hot streak is clear, matching the trend reported previously in this report. The capture efficiency ratios from the previous study are plotted in Fig. 39 as well. It should be noted that the dilution air mass flow rate to main mass flow rate ratio, $\dot{m}_{dil}/\dot{m}_{inlet}$, was slightly lower for their tests (around 5% total, or 0.55% lower for each jet).

The capture efficiencies from Vane 2 for the HS and HS+C tests are relatively consistent, between 3.4-4.4%. This is expected, as Vane 2 is nominally subjected to the same conditions between these two test cases. The tests involving hot streak and film cooling again show a distinct change in the capture efficiency ratio. Vane 3, which is subjected to the hot streak but also cooled in this case, had approximately 2.7 times less deposit than Vane 2, compared to having almost twice as much in the hot streak-only tests. While this indicates that the slot film cooling was very effective in reducing deposition even in the presence of a hot streak, it raises several questions. Is the reduction in deposition due only to particles being cooled as they travel through the film? Are particles cooled significantly in the thermal boundary layer in regions that are away from the film? And is there a vane surface temperature effect that also contributes during impact? Insight can be gained by considering the distribution of deposition on the cooled vane, as well as from particle temperature histories obtained from the numerical simulation.

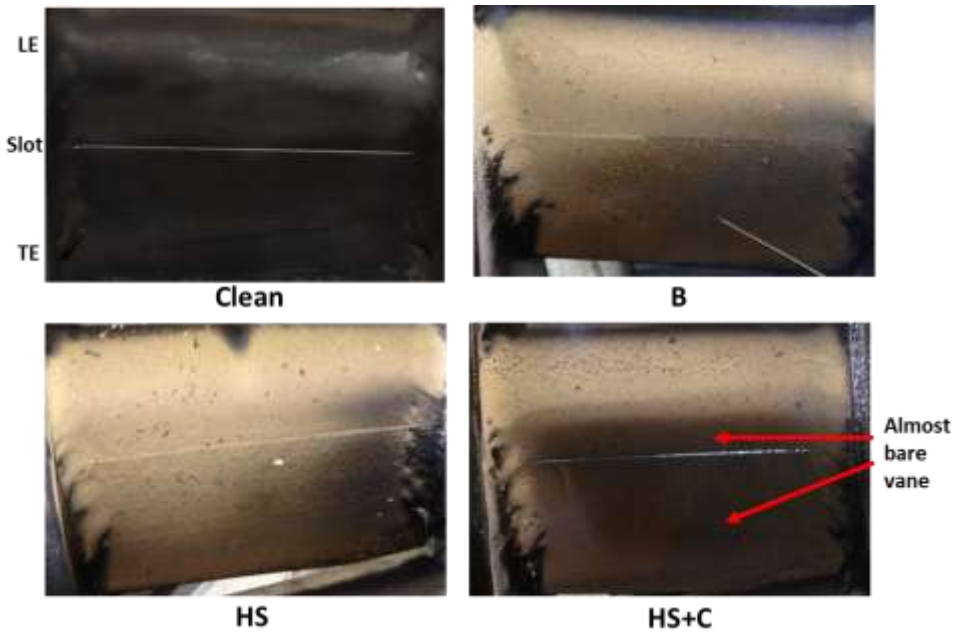


**Figure 38: Photographs of Vane 3 post-deposition for each test case.**

**Table 12: Capture efficiency results.**

| Test | $m_t$ | $\eta_{v,2}$ | $\eta_{v,3}$ | $\eta_{v,2}/\eta_{v,3}$ |
|---|---|---|---|---|
| B1 | 74.87g | 7.05% | 5.88% | 1.20 |
| B2 | 81.77g | 6.24% | 4.79% | 1.30 |
| HS1 | 76.43g | 3.40% | 7.48% | 0.45 |
| HS2 | 85.78g | 3.92% | 6.07% | 0.65 |
| HS+C1 | 63.03g | 4.38% | 1.59% | 2.76 |
| HS+C2 | 75.98g | 3.74% | 1.42% | 2.63 |

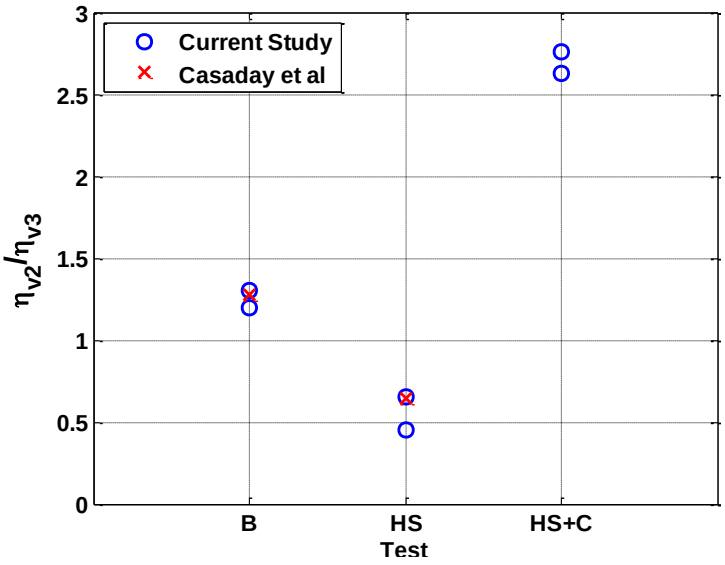


**Figure 39: Capture efficiency ratios.**

Another quantitative result from the external deposition tests conducted is deposit thickness distribution. To obtain this distribution, deposit-laden vanes are scanned with a multi-laser scanner post test. The deposit is then removed, and the vanes are scanned again. Deposit thicknesses are obtained by subtracting the clean-vane scan depth data from the deposit-laden scan data. The thickness distribution from an HS test, as well as corresponding linear traces, are shown in Fig. 40. Note that thicknesses were measured in the inlet flow (axial) direction. The contours and linear traces both show thicker deposit on Vane 3, which is expected as Vane 3 is subjected to the hot streak. Deposits are thickest at the leading edge (for both vanes) and become thinner toward the trailing edge. This trend was also found in previous studies.

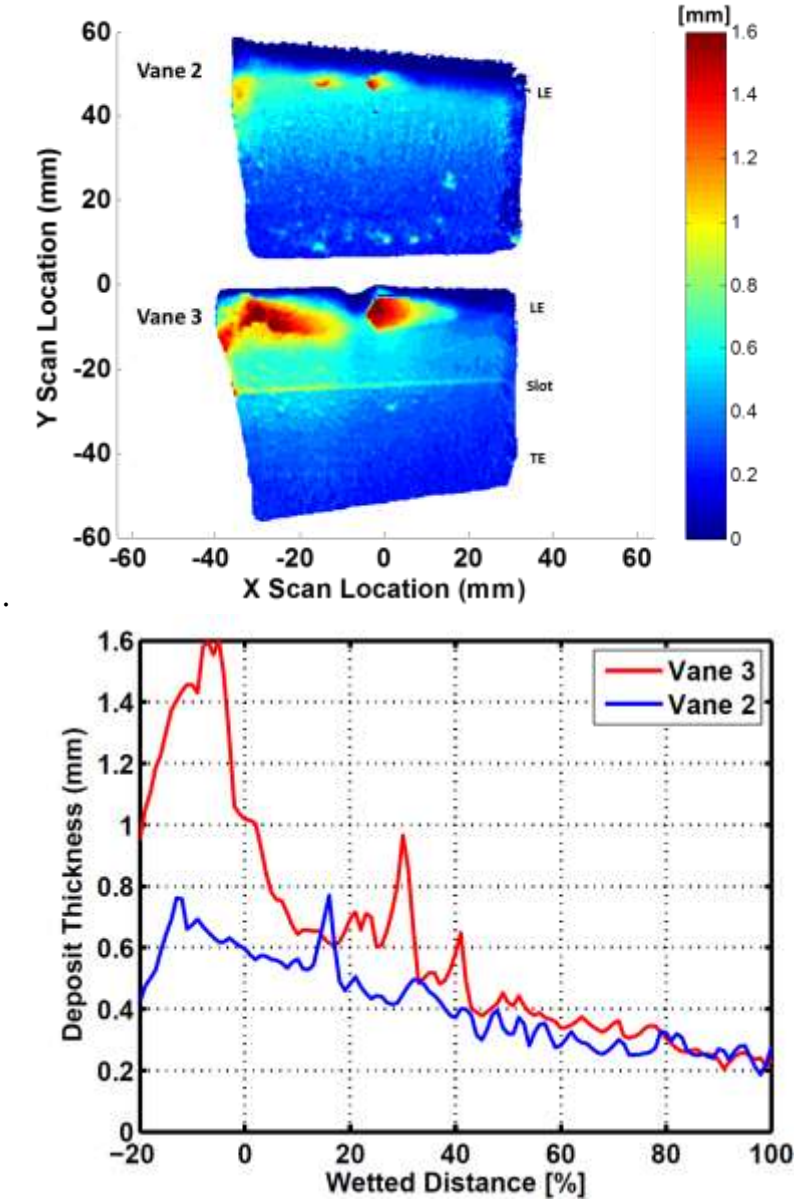


**Figure 40: Top: Contours of deposit thickness for Vanes 2&3 after an HS test. Bottom: Corresponding linear traces taken from representative regions on the vanes.**

## Computational Model

Computational fluid dynamics and conjugate heat transfer calculations of the uncooled vane (Vane 2) and slot cooled vane (Vane 3) were conducted using the commercial finite volume code FLUENT 13.0. Three-dimensional RANS simulations were performed on a domain consisting of a vane doublet. Periodic boundary conditions were implemented to simulate the cascade condition. The passage, cooling cavity, slot, and the solid vane were all meshed to allow for conjugate heat transfer calculations. The main inlet of the domain was located approximately one axial chord upstream of the vane leading edge, coinciding with the experimental inlet

temperature measurement plane. The outlet is located approximately one half axial chord from the trailing edge. The mesh is shown in Fig. 41.

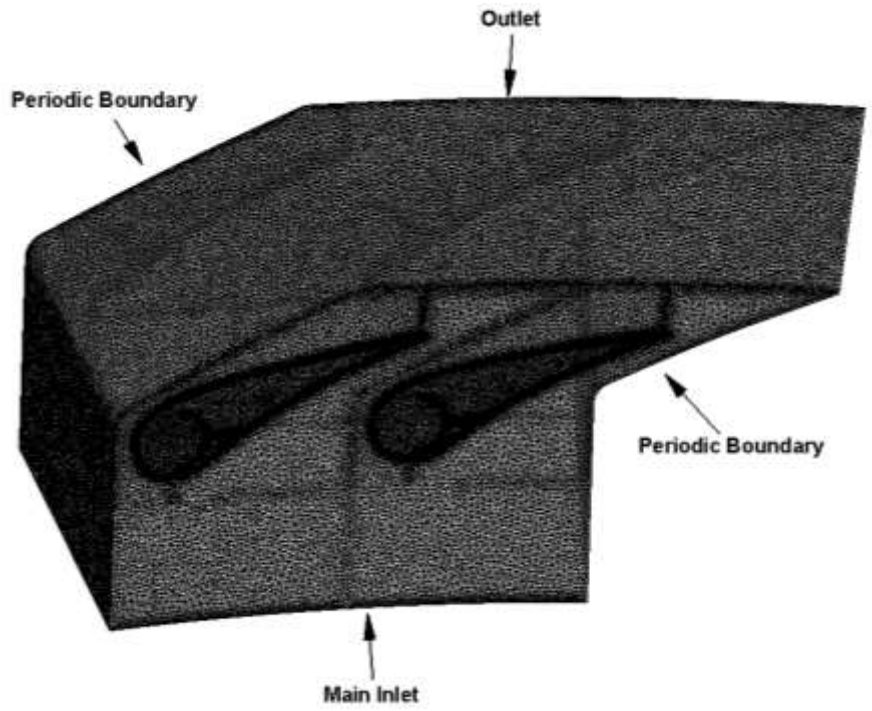


**Figure 41: Computational domain and mesh.**

Total pressure and total temperature were specified at the main flow and coolant inlets, with static pressure specified at the outlet. The endwalls were set as adiabatic walls. The $k-\omega$ SST turbulence model was employed, with turbulence intensity and length scale specified at both inlets. Whitaker et al. conducted hot film and PIV measurements to obtain turbulence data at the vane inlet of the TuRFR while running cold and hot. The mean turbulence intensity was found to be approximately 8.4%. The turbulence length scale was set by specifying the hydraulic diameter of the test section duct, which FLUENT uses in a correlation to obtain length scale. It is not possible to measure turbulence quantities in the coolant supply line, and thus a turbulence intensity of 3% was estimated for the coolant inlet boundary, with the diameter used to specify length scale. Temperature dependent polynomials were specified for the relevant properties of air and Inconel.

**Computational Flow and Heat Transfer Results**

Simulations were performed to reproduce the experimental tests for each case. This was achieved by applying the experimentally measured inlet temperature profiles as the main inlet thermal boundary condition in the simulation. Contours of Mach number in a midspan slice are shown in Fig. 42, taken from the baseline case. Figures 43-45 show temperature contours in a midspan slice for all three cases. Note that the change in colorbar scale for the HS+C case. The temperature distribution within the vane for the HS+C case gives an idea of the large amount of conduction occurring between the slot-passage and vane pressure surface. The coolant is considerably heated in the passage and exits at a higher temperature. Qualitatively, the vane

temperatures are as expected and match the experimental deposition trends. That is, the amount of ash captured by the vanes increases with increased vane temperature.

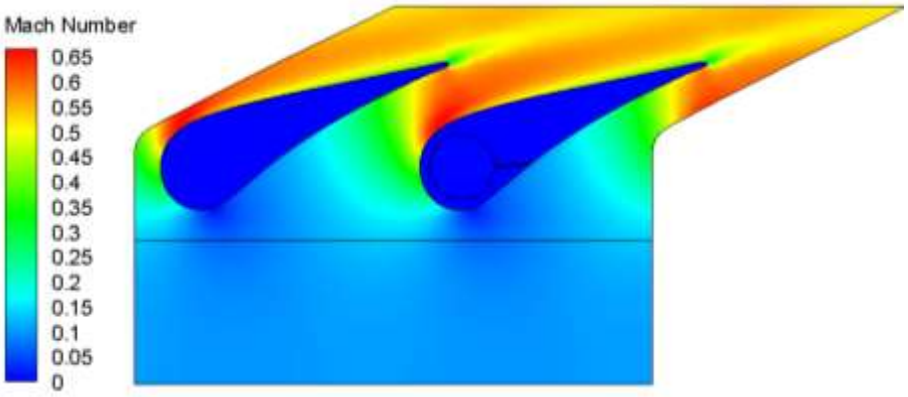


**Figure 42: Contours of Mach number in a midspan slice taken from the baseline case.**

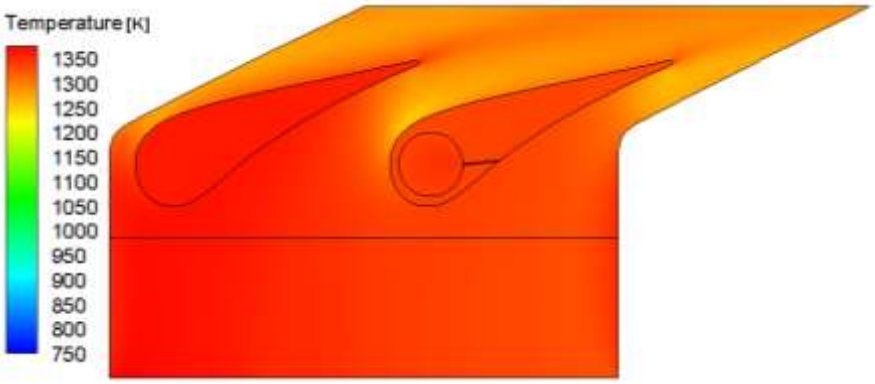


**Figure 43: Contours of total temperature in a midspan slice for the baseline case.**

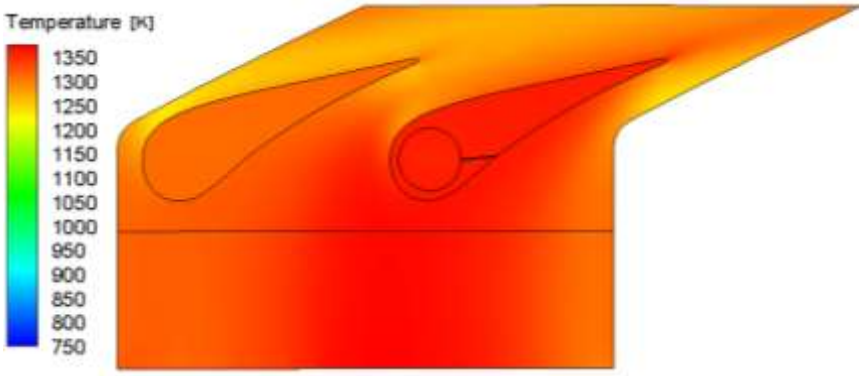


**Figure 44: Contours of total temperature in a midspan slice for the hot streak case.**

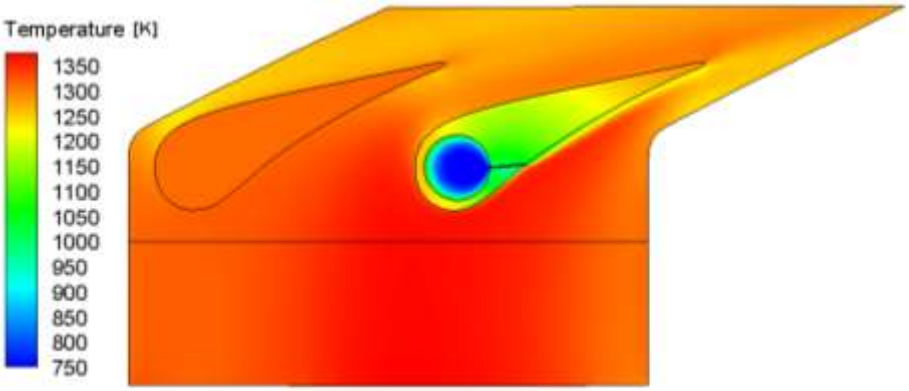


**Figure 45: Contours of total temperature in a midspan slice for the hot streak with cooling case.**

Exit temperature traces were also obtained experimentally at approximately midspan for each of the cases. They are compared to traces taken from the simulations in Fig. 46. Results from the baseline test show a good match between the simulation and experiment. The exit temperature measurements for the HS and HS+C cases are over a shorter distance, due to unforeseen difficulties during the experiment. The position of the hot streak is predicted relatively well by the simulation for the HS case. The temperatures from the simulation stray from the data in the HS+C case, however, with the CFD over predicting the effect of the coolant.

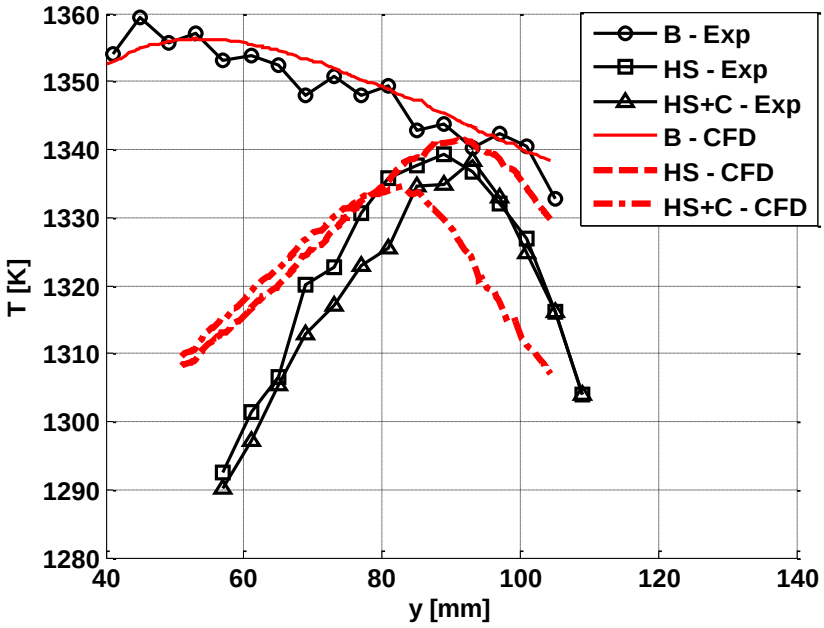


**Figure 46: Exit temperature traces from experiments and CFD.**

## Computational Deposition

Experimental deposition tests were repeated computationally using the particle tracking model in FLUENT and a tuned version of the Critical Viscosity sticking model. Deposition simulations were run for each test condition, the results of which are listed in Table 13 along with the corresponding experimental results. Average particle impact temperatures were used in the tuning process, and while this was an improvement over the method in Casaday et al., a measure of variability in the results can still be expected. Nevertheless, the model predicted capture efficiency values quite well, to within the repeatability of the experimental results in the majority of cases, with only one outlier out of the six results. The capture efficiency results, which are also plotted in Fig. 47, show that reasonable predictions of external deposition rates on a turbine vane can be obtained by experimentally tuning the sticking model. While this method lacks the grounding in physics of a fundamental model, it does show that with regard to capture efficiencies the critical viscosity model can be calibrated to a specific experiment (geometry, ash type, flow etc.) and then used to investigate many test cases without the need for further experiments.

**Table 13: Computational deposition results compared to averaged experimental data**

| Test | $\eta_{v,2}$[%] | | $\eta_{v,3}$[%] | |
|---|---|---|---|---|
| | EXP | CFD | EXP | CFD |
| B | 6.64 | 6.20 | 5.33 | 4.16 |
| HS | 3.66 | 3.97 | 6.78 | 6.25 |
| HS+C | 4.06 | 3.41 | 1.50 | 1.81 |

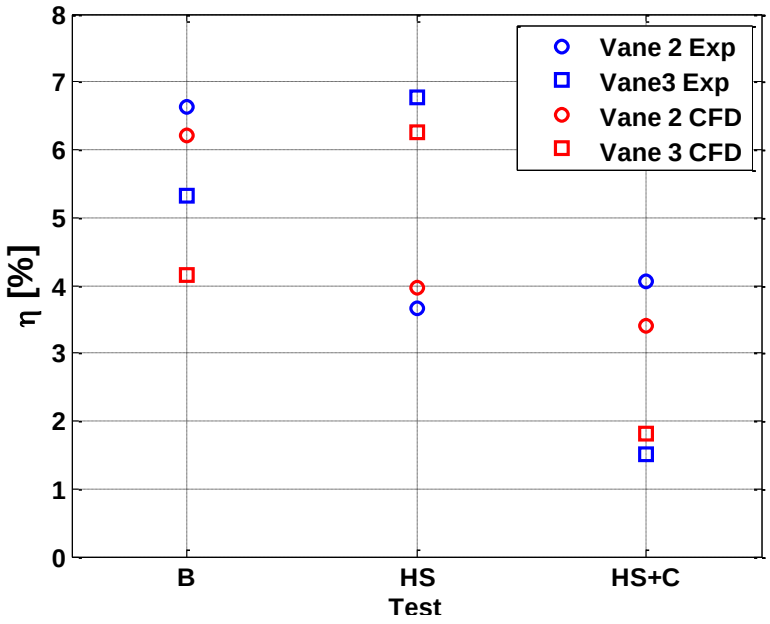


**Figure 47: Capture efficiencies from experiments and CFD for each test case.**

Contours of normalized deposit thicknesses are presented in Fig. 48 to show the distributions predicted by the simulations. The thicknesses are normalized by the maximum thickness out of all three cases (as absolute thicknesses are not on any reasonable scale). Deposition distribution is one of the main weaknesses of the critical viscosity model. In Fig. 48 each of the cases show a significant amount of deposit near the trailing edge. The simulation predicts many impacts in this region, and because the model is only statistically dependent on temperature, this results in the high frequency of deposits. However, it has been observed experimentally that deposition thicknesses are low near the trailing edge. It is thought that this is due to the high shear rates on this portion of the vane, which either removes deposit from the surface or prevents particles sticking outright. As the critical viscosity model depends only on particle temperature, the sticking probability is unaffected by the local flow shear rate, and the model misses this effect. Despite this discrepancy, there are also similarities between the predicted distributions and those seen experimentally. The CFD predicts significant deposition on the leading edge in all cases which agrees with experimental results, even for the film cooled case. Deposition patterns in the non-cooled cases are relatively uniform in the spanwise direction, and distributed over the pressure surface. For the HS+C case, the simulation predicted a significant reduction in deposition in the region downstream of the slot on Vane 3. This effect was also found in experiments.

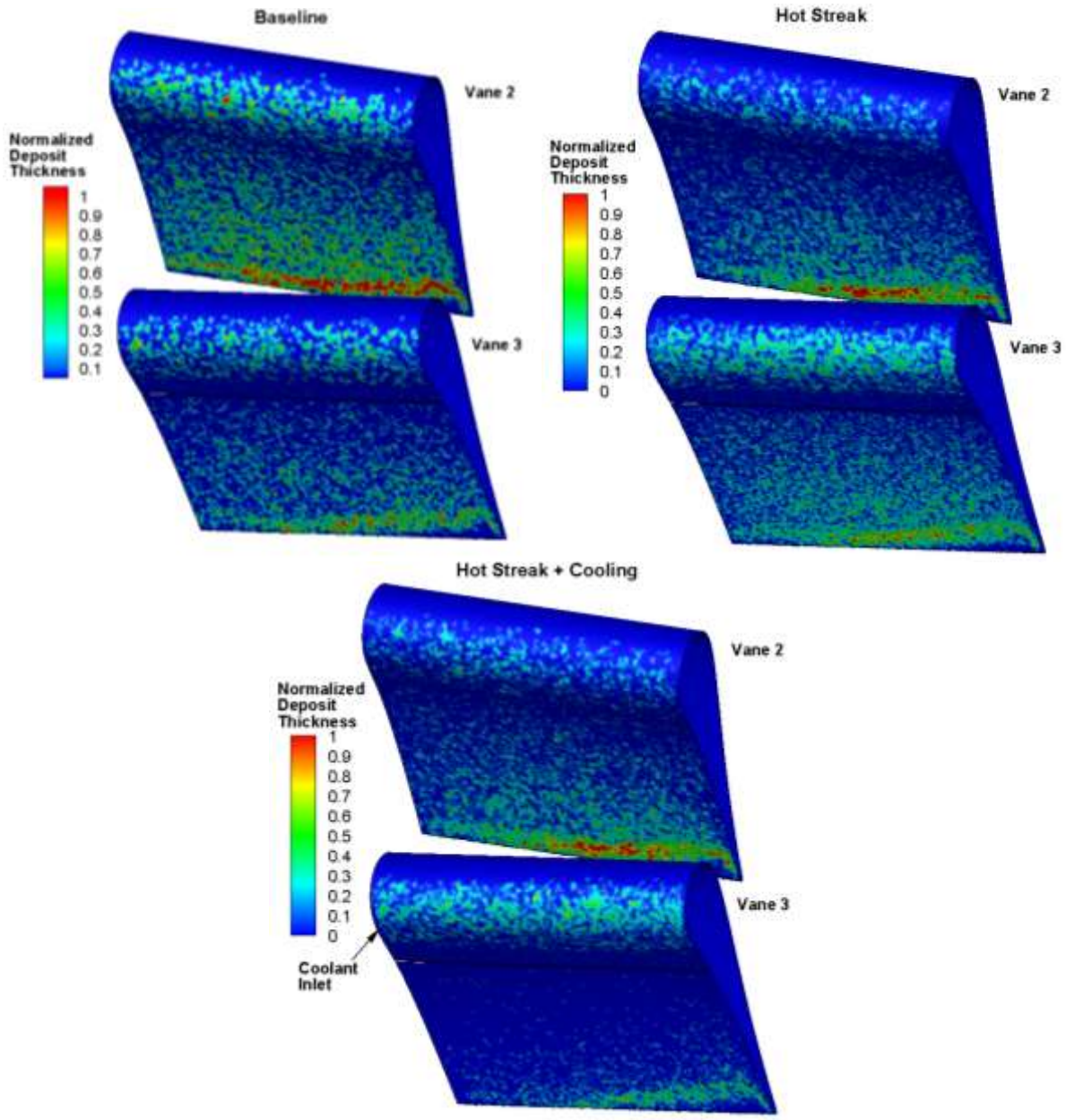


**Figure 48: Contours of normalized deposit thickness for each case.**

One of the interesting experimental results already discussed is the reduction of deposition in the region just upstream of the slot (in the HS+C case). The film is not present in this region, which suggests that particles are either cooled while they travel through the thermal boundary layer or are affected during impact with the colder surface (or both). To gain more insight into these questions, the temperature history of a single particle impacting in this region was obtained. The trajectory of the particle is shown in Fig. 49 against temperature contours, along with its temperature history. The two plots are aligned, so that changes in temperature can be referenced to the trajectory. A particle temperature history from the case without film cooling (HS), with almost the same trajectory, is also included for comparison. The simulation shows that in the film cooled case the particle loses approximately 70 K in the thermal boundary layer before

impacting the vane surface. Considering the critical viscosity model, this temperature drop translates to a significant reduction in sticking probability. The particle in the non-cooled case, by comparison, ends up sticking upon impact. Thus, it is plausible that particle cooling in the thermal boundary layer could be responsible for the reduction in deposition upstream of the slot exit, though this result does not rule out any effect from vane surface temperature.

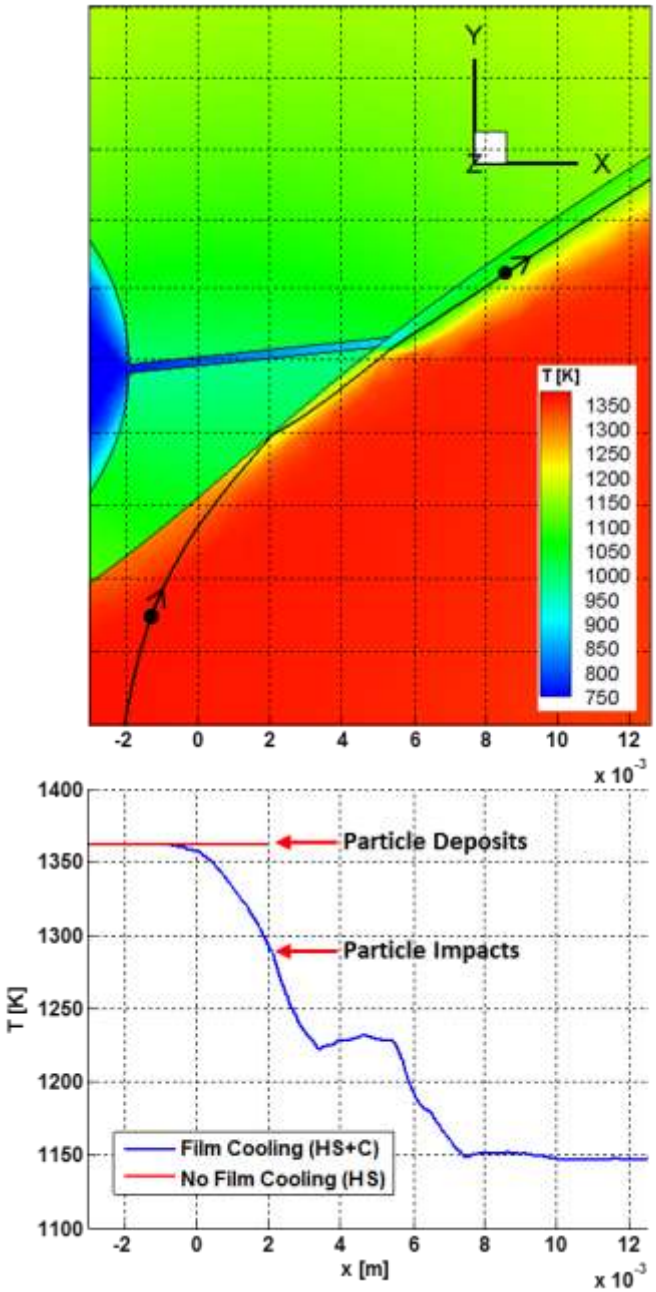


**Figure 49: Top: Trajectory of a single particle that impacts in the region upstream of the slot exit. Bottom: Temperature history of the tracked particle (aligned with the top image for reference) for the HS and HS+C cases.**

## Computational Deposition Studies in a Rotating Frame

The goal of this phase of the research was to perform calculations of a full turbine stage, including rotor and stator along with combustor hot streaks, vane cooling, and particulate deposition. The calculations are being performed on Honeywell HPT rotor and stator meshes with periodic boundaries and a sliding interface in between. These simulations use Haldeman et al (2012) in order to extract useful boundary condition information and to corroborate results. Haldeman et al.'s experiments were performed at the Ohio State University Gas Turbine Laboratory and they included non-uniform inlets and cooled hardware, but they did not include deposition.

For this phase of the effort only, the new deposition model described above was implemented into the CFD model as a wall boundary condition, with various particle sizes investigated in the simulation. The methods utilized in the numerical calculation and the results obtained are described in more detail in the following sections.

### Governing Equations and Solution Methods

The steady and unsteady forms of the continuity, momentum, and energy equations were numerically solved using the commercial finite volume code FLUENT. The working fluid is a compressible gas with properties determined using temperature dependent polynomials. The effects of turbulence were simulated using the k-ω-SST turbulence model within the RANS and URANS frameworks. This model relates the Reynolds stresses to the mean velocity gradients and the turbulent (or eddy) viscosity $\mu_t$ by the Boussinesq hypothesis, and is described in further detail in Menter (1994). A density-based solver was utilized in the implicit formulation, with convective fluxes determined using Roe's flux-difference splitting scheme.

For the steady calculations, a mixing plane was employed at the vane-rotor interface to account for the rotation of the blades. In mixing plane simulations, total pressure and total temperature at the exit of the vane domain are circumferentially-averaged in radial bands and passed as the inlet boundary condition to the rotor domain. Static pressure from the rotor domain is communicated upstream and acts as an outlet boundary for the vane domain. These two boundary conditions vary as the flow solution is computed, and thus also converge simultaneously with the rest of the flow. In the unsteady simulations a rotating mesh with sliding interface is used for the rotor domain. In this formulation all flow properties are passed directly through the interface as the rotation of the domain fully accounts for the rotation of the rotors. The physical time step in the unsteady simulations was chosen such that one period (a blade passing a full vane passage) would be divided by 20 time steps. This corresponds to $\Delta t = 5\times10^{-6}$ s, and resulted in residuals converging within 25 sub-iterations.

### Computational Domain and Boundary Conditions

While the domain and mesh have been shown in previous reports, they are presented again here for convenience. The computational domain in both the steady and unsteady simulations consists of two full vane passages and three full rotor passages. The actual number of vanes and rotors in the experiment were 24 and 38 respectively, which unfortunately does not provide a convenient ratio for periodic calculations. Thus, a 24 to 36 vane/rotor count was

assumed so that the 2 to 3 periodic configuration could be used. This small approximation allows for a very significant reduction in computational cost. The main inlet to the domain (the vane inlet) was located approximately 0.5 vane axial chords upstream of the vane leading edge, and the main outlet (rotor outlet) was placed approximately 0.3 vane axial chords downstream of the rotor trailing edge. Periodic boundaries in both the vane and rotor domains were used to simulate the full annular configuration. A schematic of the computational domain is shown in Figure 50.

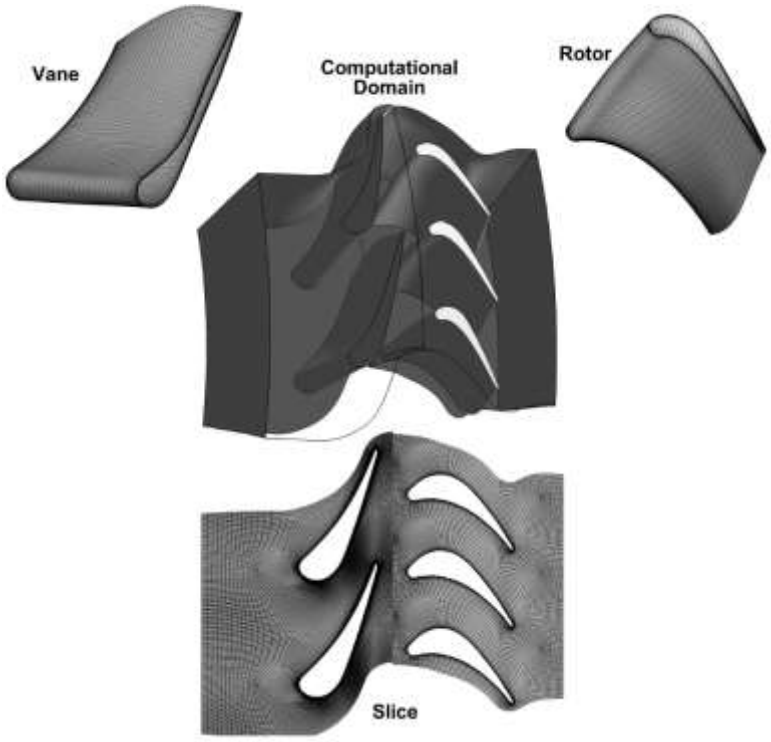


**Figure 50: Computational domain and mesh**

The experiment in Haldeman et al. (2012) was run at laboratory conditions, that is lower temperatures and reduced rotational speeds, while matching corrected speed and corrected mass flow of the machine. As temperature has been shown as a critical parameter in deposition, the temperature and pressure have been scaled up to engine relevant conditions in this simulation (while still matching the corrected speed and mass flow). Matching these corrected parameters ensures that the flow and blade Mach numbers match those in the experiment. In this manner it is possible to study deposition at engine-relevant conditions while still being able to compare to the measurements made by Haldeman et al. for validation of the flow solution. The main inlet total pressure was set to a value corresponding to a compressor overall pressure ratio (OPR) of 14. The stage exit static pressure was then set by matching the stage pressure ratio of 3.79 reported in Haldeman et al. The values of these boundary conditions are listed in Table 14 along with other boundary conditions to be discussed.

To simulate the non-uniformities present at the turbine inlet in actual engines, Gaussian total temperature profiles were superimposed on a base total temperature to represent hot streaks. The inlet profile for this calculation had a mass-averaged temperature of $T_{t,avg}$=1650 K, a

maximum-to-average temperature ratio of $T_{t,max}/T_{t,avg}$ = 1.07, and was created using the following expression,

$$T_t = A\exp\left(-\frac{(y-y_0)}{2{\sigma_y}^2}-\frac{(z-z_0)}{2{\sigma_z}^2}\right)+C$$

with A = 165, $\sigma_y$= $\sigma_z$ = 0.012, and C = 1600. The terms $y_0$ and $z_0$represent the hot streak center locations, which are clocked to mid-passage for this case. The resulting inlet total temperature profile is shown in Figure 51. The maximum-to-average temperature ratio was chosen based on ratios investigated in previous studies (Ong and Miller, 2008, Povey et al., 2007, Povey and Qureshi, 2008).

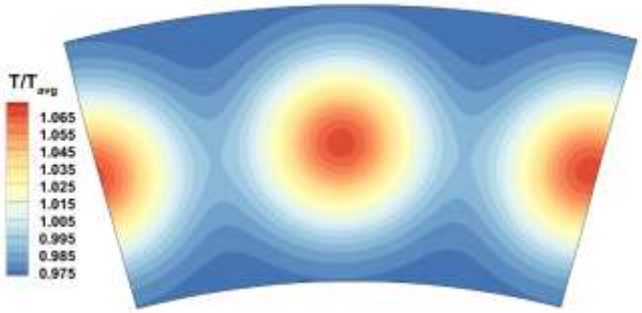


**Figure 51: Vane inlet total temperature profile**

It was not computationally feasible to use a grid that included discrete film cooling holes, as the unsteady simulations are quite expensive even with the current cell count, and a significant increase in this number would be required to adequately resolve the holes. As an alternative, the vane walls were set to a constant (cooler) temperature to simulate the effects of cooling without the considerable increase in computational cost. As fluid moves past the cool surface, a thermal boundary layer develops and yields cooler fluid in the vane wake, which is typical of the actual cooled case. While any hydrodynamic effects of the coolant being ejected over the vane surface are lost, the resulting non-uniform temperature profile at the exit of the vane and inlet to the rotor still provides an interesting condition to study (especially within the context of deposition). The vane wall temperature was set to $0.71T_{t,avg}$as reported in Haldeman et al., corresponding to approximately 1170 K. The rotors were not cooled in this simulation and their walls were set as adiabatic, along with the hub and case walls. A full list of the boundary conditions is provided in Table 14.

**Table 14: Boundary conditions**

| Boundary Condition / Scaling Parameter | Value |
|---|---|
| $N_{corr}$ | 9900 RPM |
| $P_{t,in}$ | 1,418,550 Pa |
| $P_{t,in}/P_{exit}$ | 3.79 |
| $T_{t,avg}$ | 1650 K |
| $T_{t,max}/T_{t,avg}$ | 1.07 |
| $T_{vane}/T_{t,avg}$ | 0.71 |

**Mesh**

A fully structured mesh was developed using multiple blocks of hexahedral cells, with refined boundary layer regions near all vane, rotor, and endwall surfaces. A grid independence study was conducted by generating a fine mesh and then coarsening it to create a medium mesh. Steady midspan vane and blade pressure traces were found to be within 3% between the two meshes, and thus the medium mesh was utilized for all computations reported in this study (steady and unsteady). The details of each mesh are listed in Table 15 and the medium mesh is shown in Fig. 50.

**Table 15: Mesh details**

| Mesh | Number of Cells | Average $y^+$ |
|---|---|---|
| Medium | 3,658,637 | ~1 |
| Fine | 7,431,764 | ~0.7 |

**Solution Validation**

The accurate prediction of deposition requires that particles be delivered to the surface in a realistic manner. This in turn relies on the accuracy of the particle tracking model and the flow solution. To evaluate the latter, midspan pressure traces from the steady mixing plane simulations are plotted against experimental measurements (from Haldeman et al.) in Fig. 52. Because the flow and blade Mach numbers are matched, it is possible to compare this scaled-up simulation to the experiment run at laboratory conditions. Except for a few locations, there is reasonable agreement between the simulations and the experiment, with all predicted pressures within 10% of the measured value. The simulation predicted a sharp rise in pressure on the blade suction surface just after the suction peak, which seems to be confirmed by the data. The sudden change in pressure on the vane suction surface at an axial distance of approximately 0.024m indicates the presence of a shock. Time-averaged blade pressures from the unsteady simulation are also plotted, and show similar agreement with the experimental data.

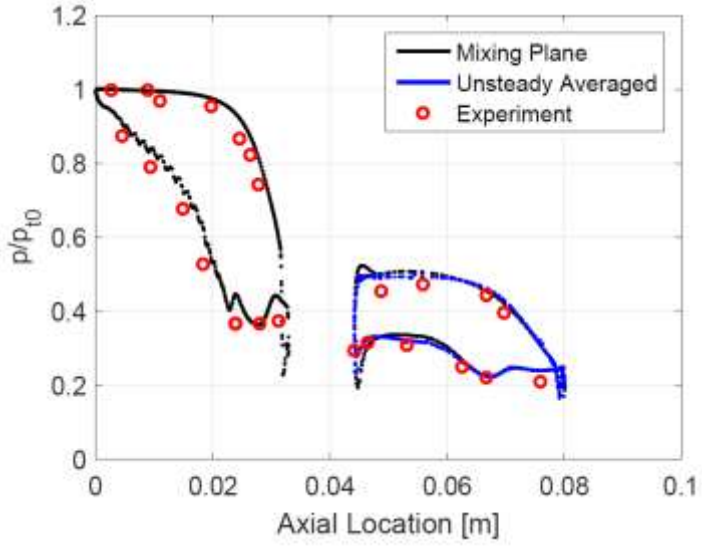


**Figure 52: Pressure traces at midspan of the vane and blade, comparing experimental data to mixing plane and unsteady predictions.**

**Particle Injection and Tracking**

Particle tracking was conducted using FLUENT's built-in Discrete Phase Model (DPM). This model calculates the trajectory of particles in the Lagrangian frame by balancing the flow-induced forces on the particle with its inertia. The DPM takes the Eulerian-Lagrangian approach, where the particle tracking is separated into two steps. In the first step, the flow solution is computed absent of any particulate. A large amount of dispersed particulate is then injected and tracked in the second step, where each trajectory is predicted by computing the local forces, as described above, at each step along the particle's path. This trajectory is stored for each particle. The k-ω turbulence model is known to produce unrealistic wall-normal velocities within $y^+ < 10$ of the wall due to the assumption of isotropic turbulence (Debhi, 2006). This error has produced unreasonably high impact efficiencies in previous studies, as particles were thrown into the wall repeatedly by simulated turbulent eddies. As such, turbulent dispersion was not employed in these simulations.

The particulate investigated is the Jim Bridger Power Station (JBPS) subbituminous coal fly ash studied experimentally by Ai (2009). This ash has a size distribution ranging from 0 - 70 μm, with a mass mean diameter of 13.4 μm. With such a large range, the natural question of which diameters to study arises. Several previous papers (e.g. Suzuki et al., 2008) involving unsteady particle tracking investigated only a single diameter, because of the computational cost associated with having to solve the unsteady flow field with each new diameter injected. Another method is to inject particles with a distribution of diameters representative of the size distribution of the particulate. The challenge with this method, however, is that a much larger number of the smaller particles is required to make up the mass fractions compared to the larger particles. As a result, a statistically significant number of larger particles will generally be accompanied by an unfeasibly larger amount of smaller particles.

An alternative procedure is implemented in this simulation, which allows the investigation of a range of diameters while avoiding the issues mentioned above. Ten diameters that span the range of the distribution are chosen, and a statistically significant number of each diameter is injected. The specific number of diameters chosen is not important, using more sizes does increase the accuracy of the method however. When particles are predicted to impact or deposit on a surface, a user defined function (UDF) keeps track of the separate sizes. This enables the calculation of the number impact efficiency and number capture efficiency for each diameter, defined by

$$\varepsilon_{N,i} = \frac{N_{imp,i}}{N_{inj,i}}$$
$$\kappa_{N,i} = \frac{N_{dep,i}}{N_{inj,i}}$$

where $N_{imp,i}$, $N_{dep,i}$, and $N_{inj,i}$ are the number of impacts, deposits, and particles injected at each diameter $i$, respectively. These number efficiencies can then be converted to mass efficiencies using the mass fraction at each diameter$f_{m,i}$,

$$\varepsilon_{m,i} = \varepsilon_{N,i} f_{m,i}$$
$$\kappa_{m,i} = \kappa_{N,i} f_{m,i}$$

In this manner, mass-based impact and capture efficiencies are determined using a representative range of diameters, with a statistically significant number of particles at each diameter. The fact

that this method is implemented in a single flow solution (as opposed to a separate flow solution for each diameter) is a considerable reduction in computational cost and time.

The diameters chosen for this study are 1, 3, 5, 10, 15, 25, 35, 45, 55, 65 μm, and are shown against the cumulative size distribution in Fig. 53. For both the steady and unsteady simulations 20,000 particles at each of the chosen diameters were injected, for a total of 200,000 particles. This injection was implemented over a full period in the unsteady case, to ensure that the position of the rotors at the initial injection time did not bias results. In the steady simulation, all particles were injected at once but required special treatment at the mixing plane. Particle locations at the vane outlet plane were stored and then randomly distributed in the circumferential direction while preserving their radial position. The question of whether to average particle variables (temperature, velocity, etc.) or preserve them was addressed by Zagnoli et al. (2015), who found no measureable difference between the two methods. Thus, in this study the particles' properties were preserved, and the new randomly distributed circumferential locations were used as an injection into the rotor domain.

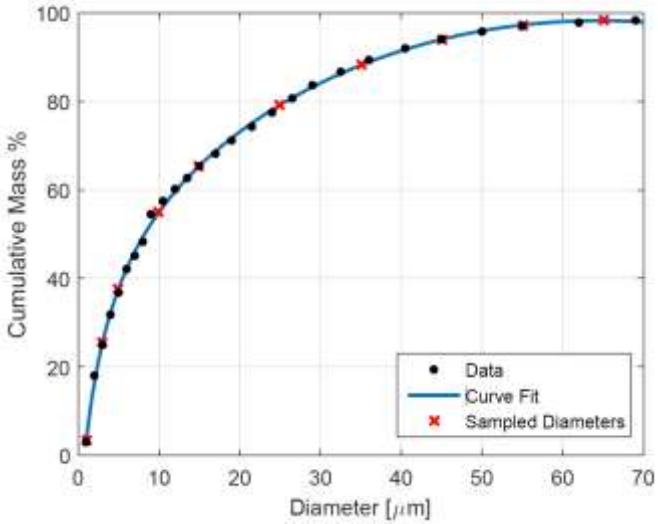


**Figure 53: Cumulative size distribution of JBPS ash, with sampled diameters indicated**

**Coefficient of Restitution and Deposition Model**

The model described earlier in the report was implemented in this simulation with the use of a User Defined Function (UDF). With its algebraic formulation, the model is ideal for implementation in CFD calculations such as the ones conducted here. The parameters of the model implemented here have been tuned to experimental data from Ai (2009), where the same JBPS ash was utilized.

**Results: Steady Mixing Plane Results**

Contours of total temperature in a midspan slice of the vane domain are shown in Fig. 54. The hot streaks which were initially clocked at mid-passage remain coherent as they travel through the passage to the vane exit. The effect of the simulated vane cooling is apparent in the cooler temperatures present in the vane wakes, which contribute to the non-uniform exit temperature profile despite some mixing. Figure 55 shows the footprint of the hot streaks and vane cooling at

the vane outlet. The reduction in spanwise passage width from the inlet to the outlet is equal from the hub and the case, thus the contours suggest a radial migration of the hot streaks toward the hub. The figure also illustrates how the circumferential variations are lost through the averaging of the mixing plane, resulting in a purely radial profile entering the rotor domain.

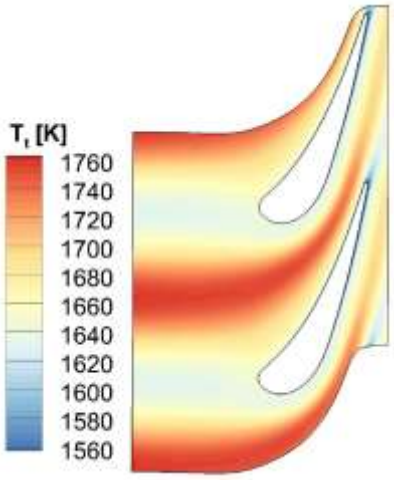


**Figure 54: Contours of total temperature in a midspan slice from the mixing plane simulation.**

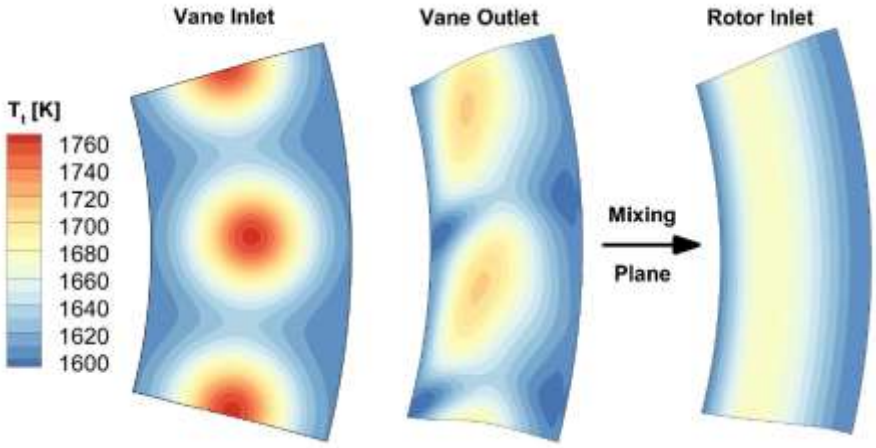


**Figure 55: Contours of total temperature at the vane inlet, vane outlet, and rotor inlet.**

Blade surface temperatures from the steady simulation are plotted in Fig. 56. It is apparent that the highest temperatures on the surface are at more outward radial station than one would predict from the rotor inlet profile in Fig. 55. This is because the static temperature at the rotor inlet, which is affected by the downstream rotor domain in the mixing plane formulation, has its maximum closer to midspan. This coupled with the initial movement of the warmer fluid outward on radius as it enters the blade passage results in the blade surface temperature profile observed. A band of cooler temperature on the suction side just downstream of the leading edge is visible, and corresponds to the suction-peak where static temperature of the flow is lowest.

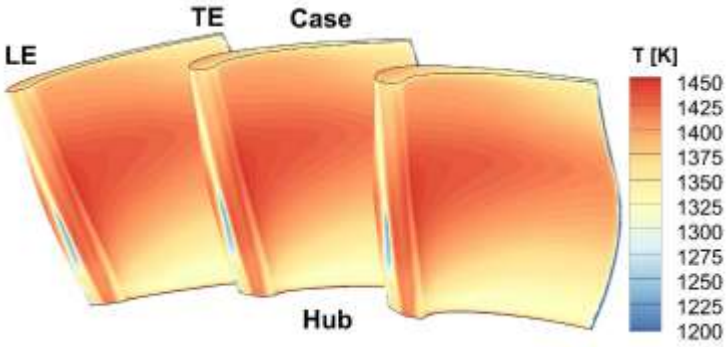


**Figure 56: Contours of blade surface temperature from the mixing plane simulation**

When investigating particle impact and deposition trends it is useful to consider the Stokes number, which is defined as the ratio of the particle relaxation time and the characteristic timescale of the flow or an obstacle,

$$St = \frac{\tau_p}{\tau_f} = \frac{\rho_p {d_p}^2 U_c}{18 \mu L_c}$$

where $U_c$ is the characteristic velocity of the flow away from the obstacle, and $L_c$ is the characteristic length scale of the obstacle. This non-dimensional parameter provides insight into the likelihood of a particle to follow the flow ($St \ll 1$) or follow a ballistic trajectory and strike the obstacle ($St \gg 1$). Two Stokes numbers are defined here, each based on the relevant values for the vane and rotor respectively. The chord of each airfoil is used for $L_c$, as one could argue that this is the characteristic length that particles are presented with as they move toward and through each passage. The velocity just upstream of each component is taken as the characteristic velocity. The vane and rotor Stokes numbers are listed in Table 16 for each diameter.

**Table 16: Vane and rotor Stokes numbers**

| $d_p$[µm] | 1 | 3 | 5 | 10 | 15 | 25 | 35 | 45 | 55 | 65 |
|---|---|---|---|---|---|---|---|---|---|---|
| **Vane *St*** | 0.0026 | 0.024 | 0.066 | 0.26 | 0.59 | 1.65 | 3.24 | 5.35 | 8.00 | 11.17 |
| **Blade *St*** | 0.018 | 0.162 | 0.45 | 1.80 | 4.06 | 11.28 | 22.11 | 36.55 | 54.60 | 76.26 |

Contours of impact and capture efficiency for the vane are presented in Fig. 57 for three different Stokes regimes. The trend in impact efficiency with Stokes number is clear, with increased impact efficiency as the non-dimensional parameter increases to and above unity. The majority of impacts are located on the aft portion of the pressure surface, and no impacts were found on the suction surface of the vane. The trend with capture efficiency is slightly different, with an initial increase with Stokes number before dropping to essentially zero for the larger particle sizes (despite the highest impact efficiency at these diameters). This is due to the deposition model which predicts that larger particles that have higher inbound kinetic energy, and thus more elastic energy to counter adhesive forces, do not deposit. Figure 58 provides a quantitative perspective of the impact efficiency trend with particle size. Because the deposition model allows for rebounds and multiple impacts, it is possible to obtain an impact efficiency greater than 100%. Unfortunately this obscures the quantitative trend with Stokes. To resolve this, a

separate particle tracking simulation was run where only the first impact was recorded. This data is included on the plot in Fig. 28 and shows the rise in impact efficiency with Stokes, asymptotic at 100%. The curve reaches this asymptote around St=1, suggesting that at least for the vane the chosen characteristic velocity and length scale were correct.

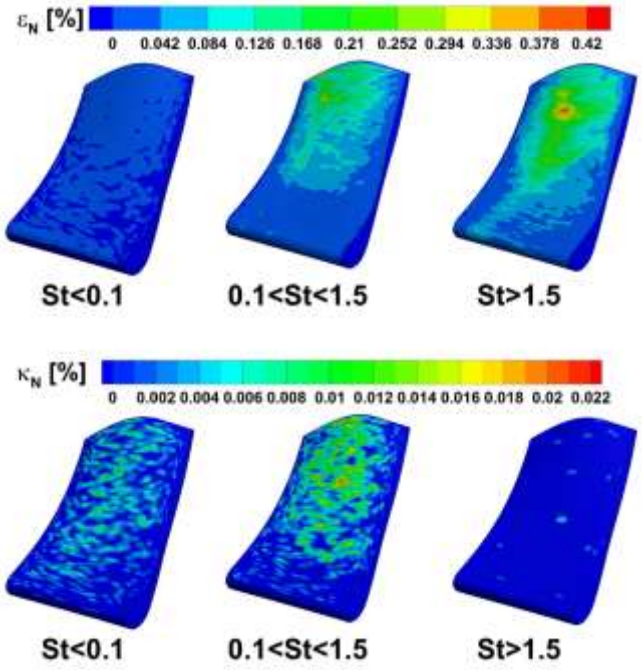


**Figure 57: Contours of number impact efficiency (top) and number capture efficiency (bottom) on the vane for various Stokes regimes (mixing plane).**

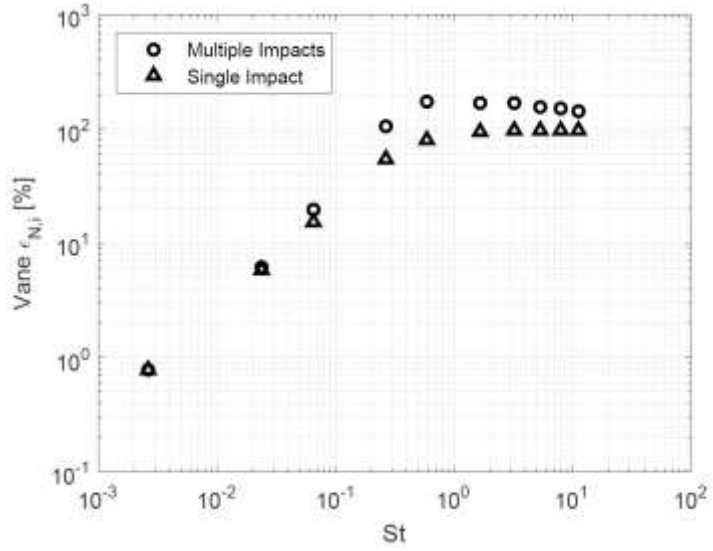


**Figure 58: Vane number impact efficiencies vs. Stokes number from the mixing plane simulation.**

The same impact and capture efficiency contours are shown for the blades in Fig. 59. Note that the values for the chosen Stokes regimes have been shifted to more relevant values for the blade

domain. A similar trend in impact efficiency is observed, with the increased efficiency with Stokes. While it may be difficult to discern from the summed contours, there is an obvious spatial trend with increasing particle size, where smaller particles impact closer to the hub and larger particles impact at increased radial locations. This pattern is quantified in Fig. 61 where the average impact location as a percentage of the span is plotted against Stokes number. Tabakoff et al. (1991) found a qualitatively similar trend, and attributed the effect to larger particles being centrifuged outward more quickly than their smaller counterparts. There is an apparent chordwise spread in impact locations with increased Stokes number, which may seem counter-intuitive at first. However, there are two factors that can explain this phenomenon. First, while one may assume that the larger particles would follow a more ballistic trajectory and thus have a more focused impact locus, the larger particles tend to impact the vane surface multiple times before entering the rotor domain. These impacts dramatically lower the inbound velocity of the larger particles, which are then affected by the simulated relative motion of the blades to a greater degree. Smaller particles, which avoid the vane, have rotor inlet velocities up to five times higher than the large particles. Secondly, larger particles tended to strike the rotor and then rebound multiple times. With the curved blade surface these multiple rebounds lead to a more distributed footprint. In the current study, larger particles were also found to impact the blade suction surface just downstream of the leading edge. These impacts will be shown when comparing to unsteady results in a later section. The single and multiple impact efficiency is plotted for each diameter in Fig. 60, and shows that the blade impact efficiency was relatively insensitive to Stokes number except for the largest particles (only due to the multiple rebounds). Again, as the particles enter the rotor domain with drastically different velocities and flow angles depending on their size, it may be that a single or traditional definition for Stokes number is not sufficient to describe the trend in the rotor domain.

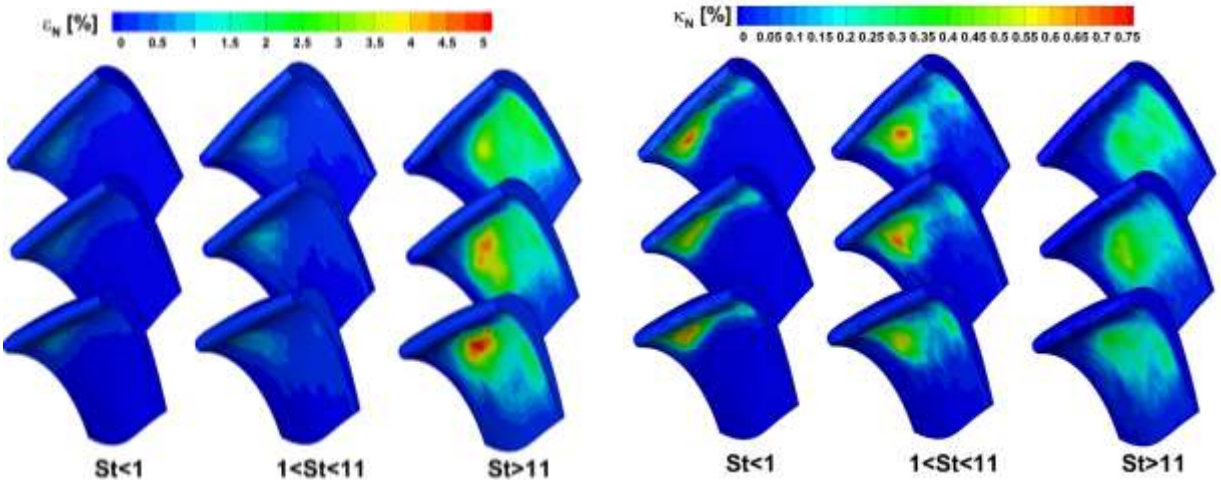


**Figure 59: Contours of number impact efficiency (left) and number capture efficiency (right) on the blades for various Stokes regimes (mixing plane).**

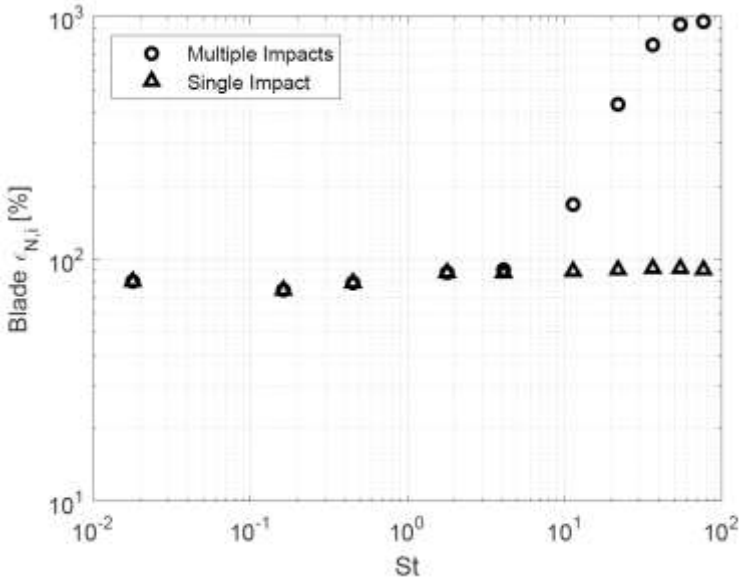


**Figure 60: Blade number impact efficiencies vs. Stokes number, from the mixing plane simulation.**

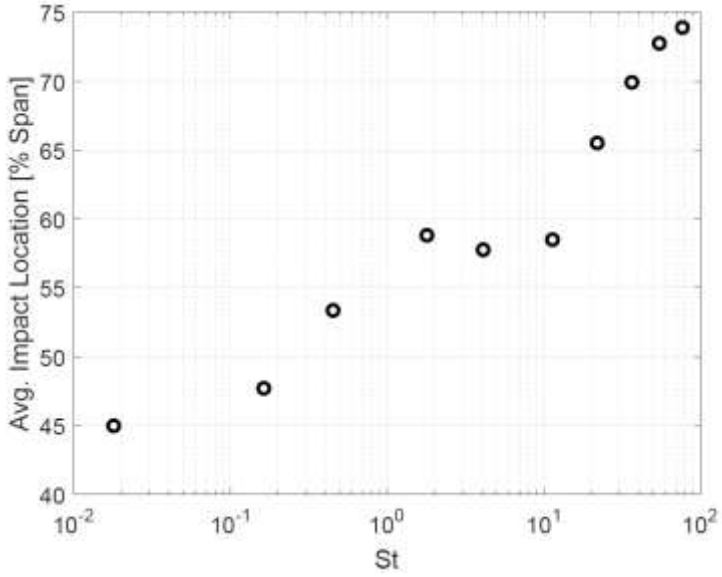


**Figure 61: Average radial impact location as a percentage of the blade span vs. Stokes number, from mixing plane simulation**

Average capture efficiencies for both the vane and rotor are plotted against Stokes in Fig. 62. As observed in the contours for the vane, there is an initial rise in capture efficiency as Stokes increases, followed by a sharp decline for the largest diameters due to their higher kinetic energy. In the case of the rotors, where impact efficiency was insensitive to Stokes number, the capture efficiency values do not vary much until approximately St=10 after which deposition is greatly reduced despite the corresponding rise in impacts at these diameters.

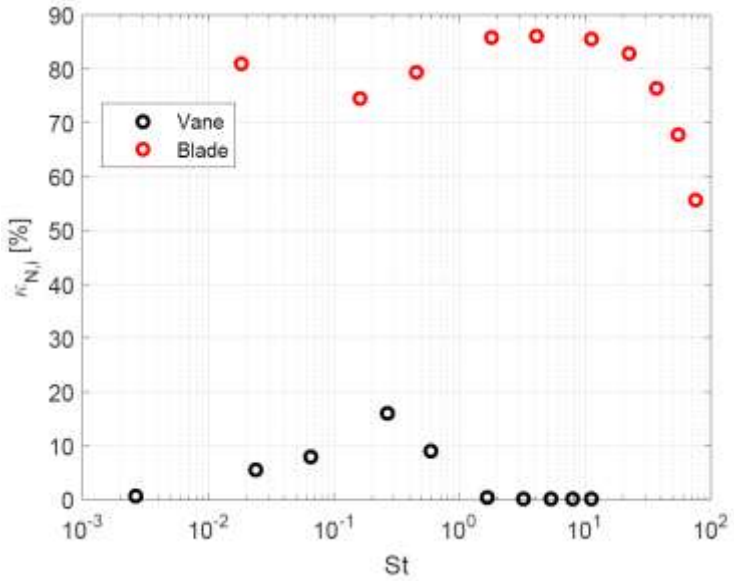


**Figure 62: Number capture efficiency for the vane and blade vs. Stokes number, from the mixing plane simulation**

**Results: Unsteady Simulation Results**

Contours of impact efficiency are shown on the vane from the unsteady case for the three Stokes regimes (Fig. 63). As may be expected, the distributions are quite similar to those from the steady case (Fig. 57) as the vane domain is not significantly affected by the downstream rotors and the flow field remains rather steady. Capture efficiency on the vane surface was also very similar in magnitude and distribution as that of the steady case, and thus is omitted. Figures 66 and 67 provide the quantitative trends for the vane with Stokes number, which are a relatively close match to the mixing plane case.

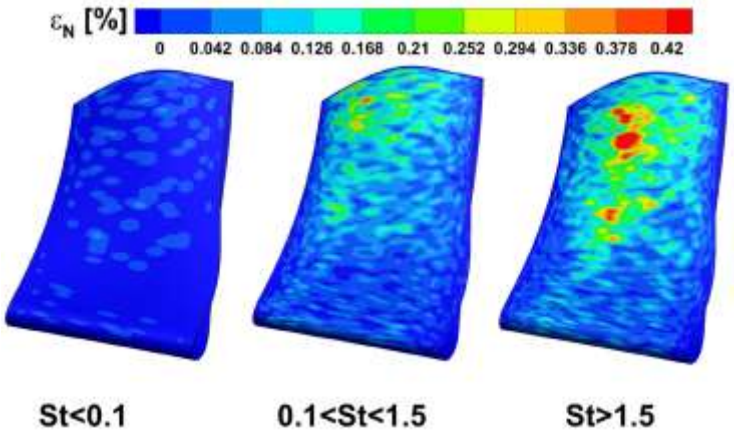


**Figure 63: Number impact efficiency contours for the vane from the unsteady simulation**

The impact and capture distributions on the blades from the unsteady case are quite different to those in the mixing plane case, as shown in Fig. 64. At the lowest Stokes numbers, while particles impact on the pressure surface near the hub in a similar fashion to the steady simulation, the impacts are distributed further back on the pressure surface. This shift in impact locations toward the trailing edge is also apparent for the two larger Stokes groups. A similar trend was observed by Zagnoli et al. (2015), who found that particles predominantly congregated in the vane wake upon exiting the vane domain. The particles were subsequently transported by the slower moving wake-fluid at a reduced incidence angle to the rotor leading edge, causing impacts further toward the trailing edge. The mixing plane calculation, which smears circumferential non-uniformities, is not able to capture these effects. The medium Stokes regime ($1<St<11$) saw an increased amount of impacts near the blade tip region, which has been observed in practice. Perhaps the most striking difference to the steady case is the large number of impacts just downstream of the leading edge on the suction surface for the largest Stokes group. While there are still impacts on the pressure surface near the trailing edge, these are swamped in comparison by the suction surface impacts.

To explain this trend, a midspan slice with finite thickness is extracted and all particles outside of this band are blanked out. The result is Fig. 68 which shows locations of 10 and 45 μm particles at four different timesteps, with particles colored by the magnitude of their velocity. In the 10 μm case particles are accelerated as they leave the vane passage and are able to deviate to some degree around the rotor blades, preventing suction surface impacts. The larger particles exit the vane domain with a lower velocity, having struck the vane pressure surface, and are congregated within the vane wake when entering the rotor domain. Unlike the smaller particles, they are not able to deviate from the oncoming rotor blades and instead the blades effectively `chop' the stream of larger particles as they rotate by. These larger particles are less prone to depositing and thus rebound multiple times on the rotor blade suction surface as the blade continues to rotate toward them. An arrow indicating the magnitude of the rotors' rotational velocity is located below the colorbar in each figure, and shows that the larger particles are indeed slower than the rotating blades while the smaller particles are able to accelerate and avoid the blades. Suction surface impacts were also observed in the steady mixing plane case, however their number is dwarfed by the multiple rebounds that occur on the pressure surface in that case. Figure 65 shows contours of single-impact efficiency (taken from the simulation where only a single impact was allowed to occur), and indicates that a fair amount of the particles with $St>11$ impact the suction surface. Note that no suction surface impacts were predicted in Zagnoli et al., as the maximum particle size investigated in that study was 15 μm.

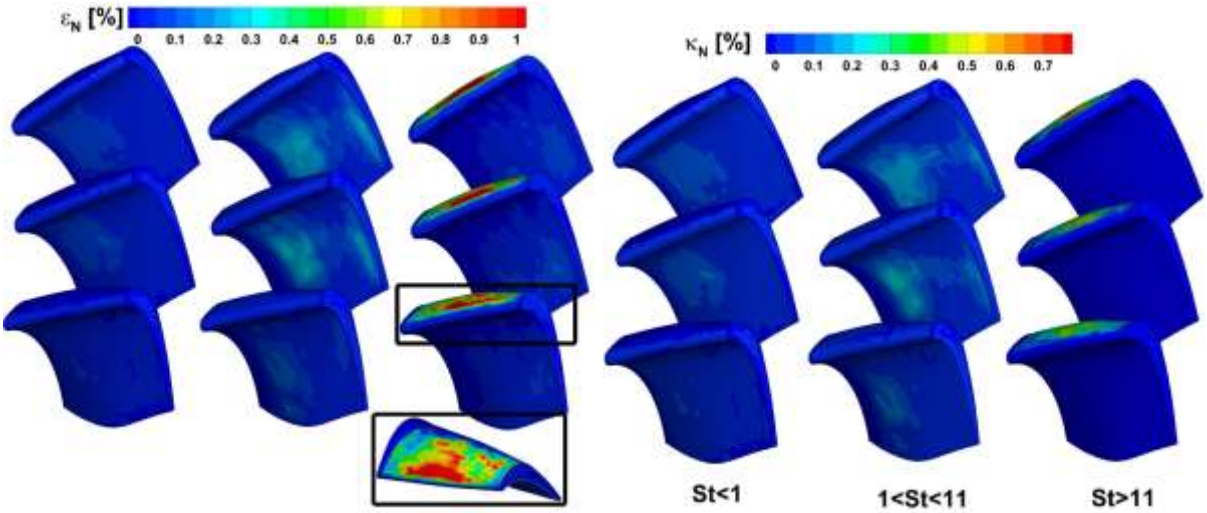


**Figure 64: Number impact and capture efficiency contours for the blade from the unsteady simulation.**

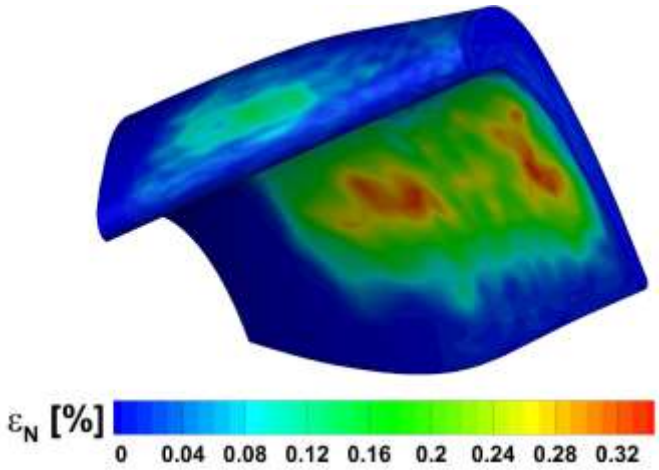


**Figure 65: Contours of single-impact efficiency for St>11 from the mixing plane calculation, showing suction surface impacts.**

Impact and capture efficiency for the blades in the unsteady simulation are plotted in Figures 66 and 67 against Stokes number. Interestingly, the blade impact efficiency followed a similar trend with particle size as that of the vane (up to St = 10), which was not observed in the mixing plane calculation. Impact efficiency asymptotes as the Stokes number increases to and above unity, before increasing sharply for the four largest particles. The blade capture efficiency rises initially with the smaller particles sizes before a slight decrease at 15 μm, as observed with the vane. For St > 10, capture efficiency rises as the impact efficiency of the same particle sizes increases.

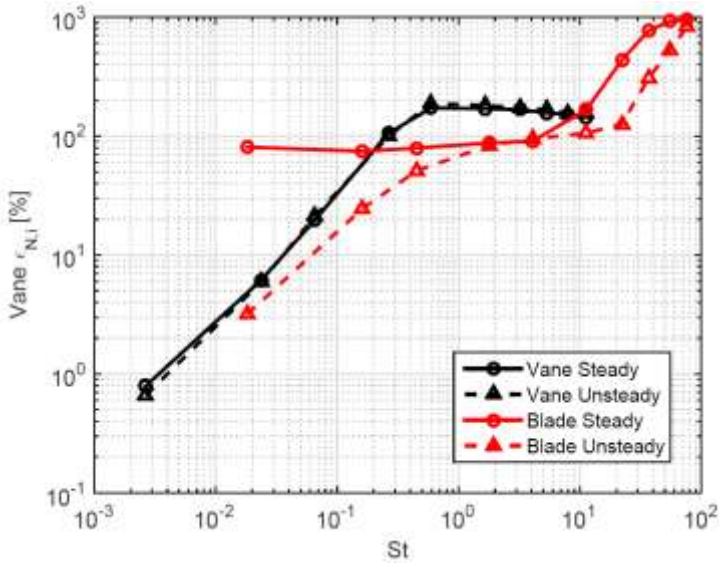


**Figure 66: Number impact efficiency for the vane and blade from the mixing plane and unsteady simulations.**

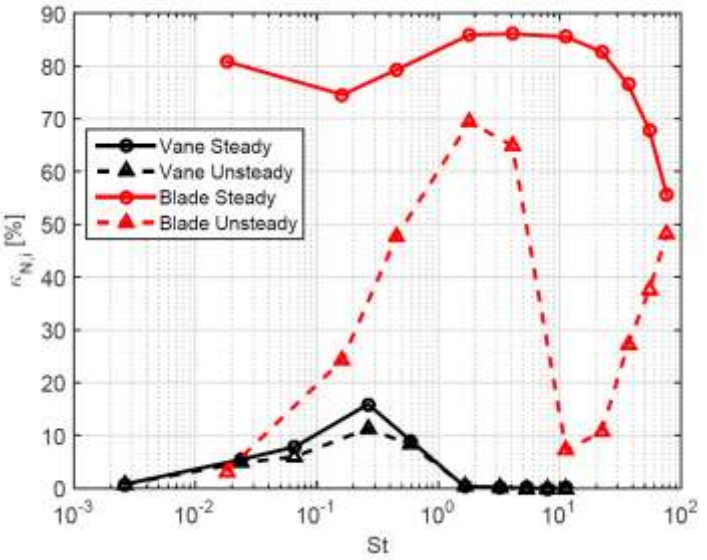


**Figure 67: Number capture efficiency for the vane and blade from the mixing plane and unsteady simulations.**

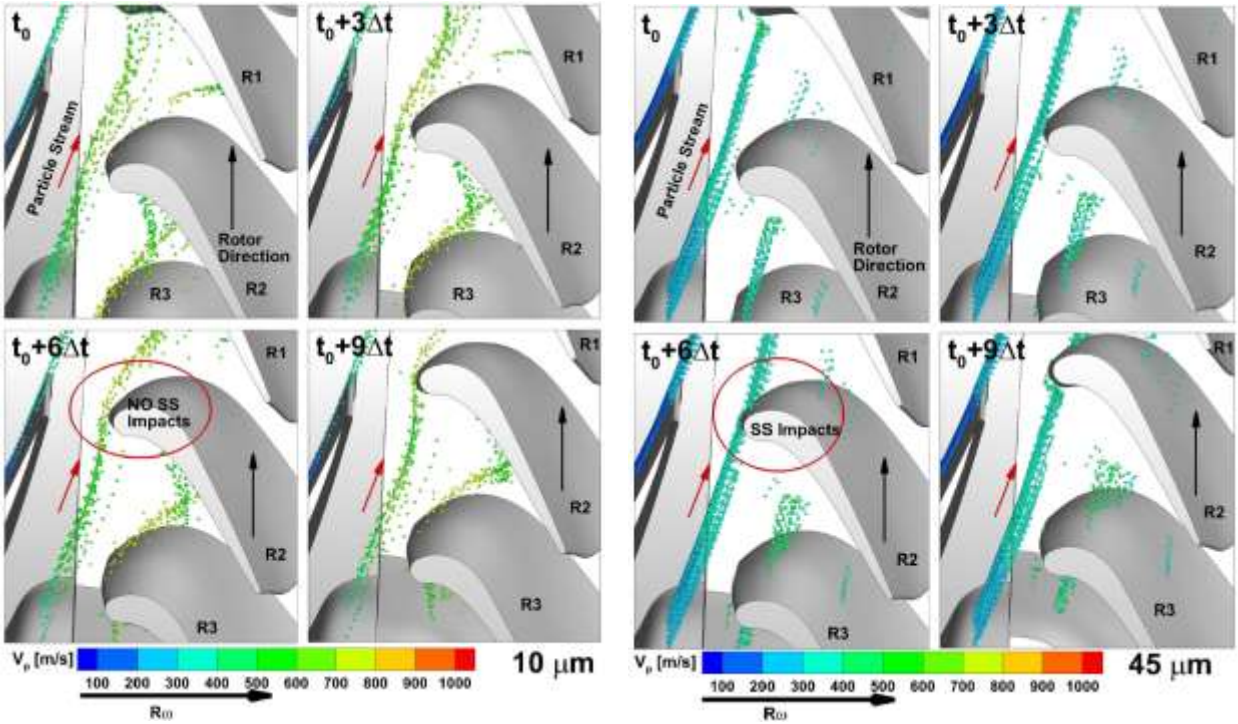


**Figure 68: Snapshots of particle locations at four different time steps for two different particle sizes, colored by particle velocity magnitude.**

Another important aspect to consider is the effect of rotor inlet temperature, which is a circumferentially averaged profile in the mixing plane case and a non-uniform profile that varies with time in the unsteady case. Figure 69 shows how the blade temperatures can change throughout a vane-passing period. Specifically, this difference is important to deposition mechanics if it affects the particle temperature upon impact, as the particles' mechanical properties are a function of temperature. As such, the average particle impact temperature for each of the cases is plotted in Fig. 70, together with the impact temperatures for the vane as well. As expected, there is a close match in the vane impact temperature between the steady and unsteady cases. The average blade impact temperatures, however, do show some difference between the two cases, with the unsteady case generally lower than the mixing plane temperatures. A difference of up to 30 K in average temperature coupled with standard deviations of up to 35 K imply differences of up to 110 K, in a regime where particle yield stress is quite sensitive to temperature. To determine the effect that this discrepancy had on the predictions of deposition by the model employed, a sticking efficiency is calculated by dividing the capture efficiency by the impact efficiency. The result is plotted for the blade from the steady and unsteady simulations in Fig. 71, and shows a decreased sticking efficiency for several of the particle sizes. While temperature is not the only parameter that would cause this decrease, it is bound to contribute to it. This comparison provides another example of significant differences between the predictions obtained from steady and unsteady methods, that can and do affect the overall simulation of deposition in a turbine stage.

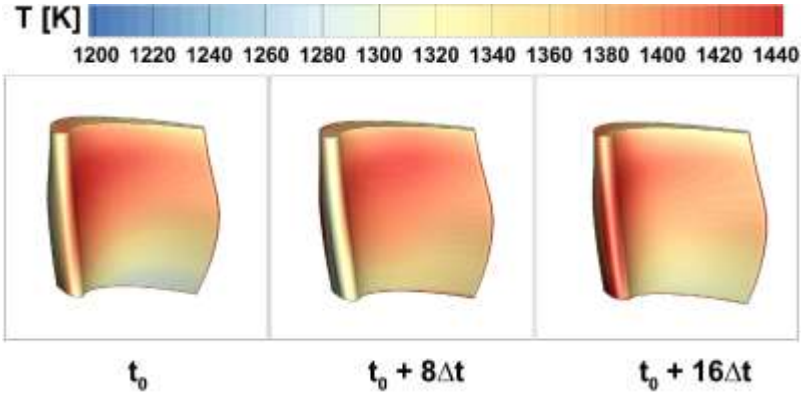


**Figure 69: Blade temperatures from the unsteady simulation at different timesteps.**

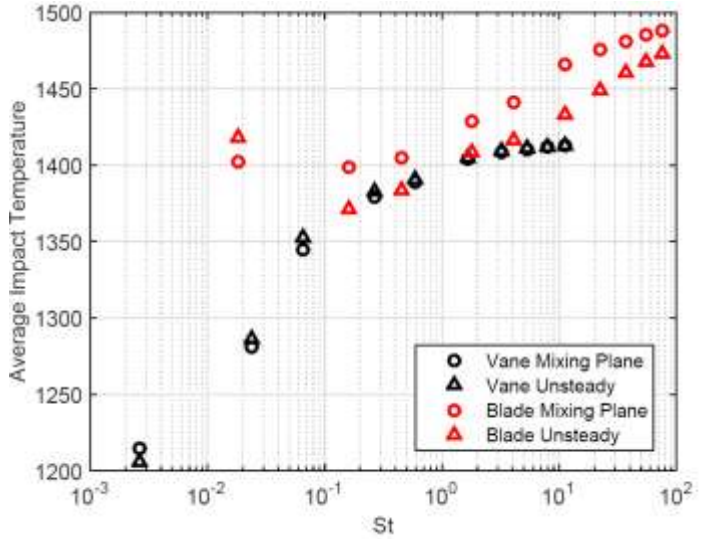


**Figure 70: Average temperature upon particle impact for the steady and unsteady cases.**

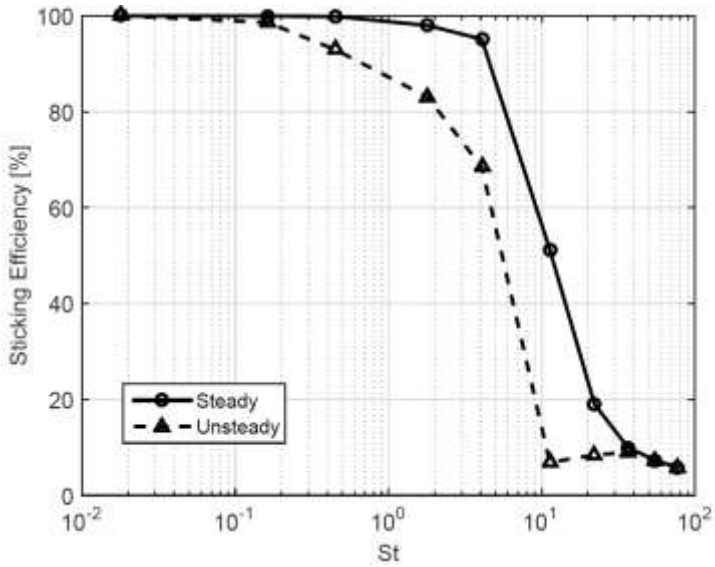


**Figure 71: Sticking efficiency vs. Stokes for the blade from the steady and unsteady simulations.**

## CONCLUSIONS

After this extensive 4-year study, the following conclusions are in order:

1. Hot streaks produce accelerated deposition, as has been observed in practice.
2. Cooling can produce substantial reductions in deposition, both from the effect of the film in cooling particles as they approach the vane surface and from the conduction effect.
3. Hot streaks and cooling have a synergistic effect on deposition. In other words, the increase in deposition due to hot streaks and the reduction due to cooling cannot be superimposed to predict the effect on deposition when both are present.
4. A simple particle rebound model including elastic and plastic deformation as well as surface adhesion can adequately capture rebound mechanics. Deposition modeling is more complicated yet insights can be gleaned from a simple approach offered in the new model.
5. Deposition on a turbine rotor must be predicted using an unsteady solver. Mixing plane models are woefully inadequate. Since particles generally congregate in the vane wake, they deviate from the vane passage flow as they enter the rotor and preferentially impact the pressure surface. Large particles are centrifuged to the rotor tip.

REFERENCES

Ai, W., and Fletcher, T.H., 2009, "Computational Analysis of Conjugate Heat Transfer and Particulate Deposition on a High Pressure Turbine Vane," presented at ASME Turbo Expo 2009: Power for Land, Sea, and Air. June, 2009, Florida, United States. Paper #: GT2009-59573.

Ai, W., Murray, N., Fletcher, T., Harding, S., Lewis, S., and Bons, J., 2012. "Deposition Near Film Cooling Holes on a High Pressure Turbine Vane" *J. Turbomachinery **134***

Barker, B., Casaday, B., Shankara, P., Ameri, A., Bons, J.P., 2013, "Coal Ash Deposition on Nozzle Guide Vanes: Part II – Computational Modeling," *ASME Journal of Turbomachinery*, Vol. 135, January 2013, 011015, (9 pages).

Battelle Columbus Div. Ohio, Deel, O. "Mechanical-Property Data Inconel 625. Annealed Sheet." (1971)

Bitter, J., 1963. "A Study of Erosion Phenomena". *Wear*, 6, pp. 5–21.

Bonilla, C., Webb, J., Clum, C., Casaday, B., Brewer, E., and Bons, J., 2012. "The Effect of Particle Size and Film Cooling on Nozzle Guide Vane Deposition" *ASME Turbo Expo 2012: Power for Land, Sea, and Air.*

Bons, J.P., Blunt, R., and Whitaker, S., 2015, "A Comparison of Techniques for Particle Rebound Measurement in Gas Turbine Applications", accepted for presentation at the ASME Turbo Expo 2015 in Montreal Canada, June 15-19, 2015. Paper #GT2015-43766.

Brach, R. M., Dunn, P. F., "A Mathematical Model of the Impact and Adhesion of Microspheres," *Aerosol Science and Technology* Vol. 16 (1992): 51-64.

Casaday, B., 2013, "Investigation of Particle Deposition in Internal Cooling Cavities of a Nozzle Guide Vane," PhD Thesis, Ohio State University.

Casaday, B., Prenter, R., Bonilla, C., Lawrence, M., Clum, C., Ameri, A., and Bons, J. P., 2013. "Deposition with Hot Streaks in an Uncooled Turbine Vane Passage" *ASME Turbo Expo 2013: Power for Land, Sea, and Air.*

Crosby, J., Lewis, S., Bons, J., Ai, W., and Fletcher, T., 2007. "Effects of Particle Size, Gas Temperature, and Metal Temperature on High Pressure Turbine in Land Based Gas Turbines from Various Synfuels." *ASME Turbo Expo 2007: Power for Land, Sea, and Air.*

Dehbi, A., 2006. "Assessment of a New Fluent Model for Particle Dispersion in Turbulent Flows". Workshop Proceedings on Benchmarking of CFD Codes for Application to Nuclear Reactor Safety (CDF4NRS).

Delimont, J.M., Murdock, W.F. Ng, and Ekkad, S.V., 2014, "Effect of Temperature on Microparticle Rebound Characteristics at Constant Impact Velocity," ASME Turbo Expo 2014, ASME, p. 25687, Dusseldorf, Germany.

Grant, G. and Tabakof, W., "Erosion Prediction in Turbomachinery Resulting from Environmental Solid Particles," Journal of Aircraft, Vol. 12, No. 5, May 1975, pp 471-478.

Haldeman, C.W., Dunn, M.G., Mathison, R.M., 2010. "Fully-Cooled Single Stage HP Transonic Turbine: Part I – Influence of Cooling Mass Flow Variations and Inlet Temperature Profiles on

Blade Internal and External Aerodynamics" *ASME Turbo Expo 2010: Power for Land, Sea, and Air.*

Hindman, E.E., Horn, R.D., and Finnegan, W.G., 1982, "Particle generation, transport, and characterization at the First International Workshop on light absorption by aerosol particles," Appl. Opt. Vol. 21, pp. 403-412.

Hussainova, I., Schade, K.P. "Correlation between Sold Particle Erosion of Cermets and Particle Impact Dynamics," *Tribology International* Vol. 41 (2008): 323-330.

Johnson, K., Kendall, K., and Roberts, A., 1971. "Surface Energy and the Contact of Elastic Solids". Presented at the Royal Society of London, Series A: Mathematical and Physical Sciences.

Kim, O.V., and Dunn, P.F., 2007, "A microsphere-surface impact model for implementation in computational fluid dynamics," Journal of Aerosol Sciences, Vol 38, pp. 532-549.

Liu, C-N, Chien, C-L, Lo, C-C, Lin G-Y, Chen, S-C, and Tsai, C-J, 2011, "Drag Coefficient of a Spherical Particle Attached on the Flat Surface," *Aerosol and Air Quality Research,* Vol, 11, pp. 482-486.

Ong, J., and Miller, R., 2008. "Hot Streak and Vane Coolant Migration in a Downstream Rotor". ASME IGTI Turbo Expo 2008.

Povey, T., Chana, K. S., Jones, T. V., and Hurrion, J., 2007. "The Effect of Hot-Streaks on HP Vane Surface and Endwall Heat Transfer: An Experimental and Numerical Study,". *J. Turbomachinery,* Vol. 129.

Povey, T., and Qureshi, I., 2008. "A Hot-Streak (Combustor) Simulator Suited to Aerodynamic Performance Measurements,". Proc. IMechE Part G: J. Aero. Eng., 222.

Prenter, R., Whitaker, S., Ameri, A., Bons, J.P., 2014, "The Effects of Slot Film Cooling on Deposition on a Nozzle Guide Vane". Paper #GT2014-27171

Reagle, C. J., Delimont J. M., Ng, W. F., Ekkad, S. V., 2013, "Study of Microparticle Rebound Characteristics Under High Temperature Conditions," Proceedings of ASME Turbo Expo 2013, San Antonio, Texas, USA.

Richards, G.A., Logan, R.G., Meyer, C.T., Anderson, R.J. "Ash Deposition at Coal-Fired Gas Turbine Conditions: Surface and Combustion Temperature Effects*," Journal of Engineering for Gas Turbines and Power* Vol. 114 (1991): 132-138.

Singh, S., and Tafti, D., 2013. "Predicting the Coefficient of Restitution for Particle Wall Impacts in Gas Turbine Components". Presented at the 2013 ASME Turbo Expo in San Antonio, Texas. Paper Number: GT2013-95623.

Soltani, M., Ahmadi, G., "On particle adhesion and removal mechanisms." *Journal of Adhesion Science and Technology,* 1994. Vol. 8, No. 7, pp-763-785 (1994)

Suzuki, M., Kazuaki, I., and Makoto, Y., 2008. "Numerical Simulation of Sand Erosion Phenomena in Rotor/Stator Interaction of Compressor,". J. Therm. Sci., 17.

Tabakoff, W., Hamed, A., and Metwally, M., 1991. “Effect of Particle Size Distribution on Particle Dynamics and Blade Erosion in Axial Flow Turbines”. J. Engr. Gas Turbines and Power, 113.

Tafti, D. K., and Sreedharan, S.S., 2010, "Composition Dependent Model for the Prediction of Syngas Ash Deposition with the Application to a Leading Edge Turbine Vane." ASME Turbo Expo 2010: Power for Land, Sea, and Air (2010).

Wall, S., John, W., Wang, H., and Goren, S., 1990. “Measurements of Kinetic Energy Loss for Particles Impacting Surfaces”. *Aerosol Science and Technology*, 12(4), pp. 926–946.

Weir, G., and McGavin, P., 2008. “The Coefficient of Restitution for the Idealized Impact of a Spherical, Nano-Scale Particle on a Rigid Plane”. pp. 1295–1307. Presented at the Royal Society of London, Series A: Mathematical and Physical Sciences.

Whitaker, S., and Bons, J., 2015. “Evaluation of Elastic-Plastic Rebound Properties of Coal Fly Ash Particles for Use in a Universal Turbine Deposition Model”. Presented at the 2015 ASME Turbo Expo in Montreal, Canada. Paper Number: GT2015-43765.

Whitaker, S.M., Peterson, B., Miller, A.F., and Bons, J.P., 2016, “The Effect of Particle Loading, Size, and Temperature on Deposition in a Vane Leading Edge Impingement Cooling Geometry,” submitted to the IGTI 2016 Exposition in Soeul, Korea. In review.

Whitaker, S., Prenter, R., Bons, J.P., 2014, “The Effect of Free-Stream Turbulence on Deposition for Nozzle Guide Vanes”. Paper #GT2014-27168.

Whitaker, S.M., Reilly, D., Bons, J.P., Crafton, J. “A Survey of Airborne Particle Impact Characteristics Using High Speed Particle Shadow Velocimetry.” *43rd AIAA Fluids Dynamics Conference* (2013).

Whitaker, S., Prenter, R., Bons, J.P., 2014, “The Effect of Free-Stream Turbulence on Deposition for Nozzle Guide Vanes”. Paper #GT2014-27168

White, F., *Viscous Fluid Flow*, 3rd ed. McGraw-Hill.

Wu, C., Li, L., and Thornton, C., 2003. “Rebound Behavior of Spheres for Plastic Impacts”. *International Journal of Impact Engineering*, 28, pp. 929–946.

Yang, H., and Boulanger, J., 2011. “The Whole Annulus Computations of Particulate Flow and Erosion in an Axial Fan”. Presented at the 2011 ASME Turbo Expo in Vancouver, Canada. Paper Number: GT2011-45992.

Zagnoli, D., Prenter, R., Ameri, A., and Bons, J.P., 2015, “Numerical Study of Deposition in a Full Turbine Stage Using Steady and Unsteady Methods”, ASME Turbo Expo 2015 in Montreal Canada, June 15-19, 2015. Paper #GT2015-43613.

Ziskind, G., 2006, “Particle Resuspension from Surfaces: Revisited and Re-evaluated,” *Rev. Chem. Eng.*, 22: 1-123.

Zoeteweij, M., van der Donck, J., and Versluis, R., 2009. “Particle Removal in Linear Shear Flow: Model Prediction and Experimental Validation”. Adhesion Science and Technology, 23, pp. 899–911.